

2015

Prediction of vertebral fractures under axial compression and anterior flexion

<https://hdl.handle.net/2144/16086>

Boston University

BOSTON UNIVERSITY
COLLEGE OF ENGINEERING

Dissertation

**PREDICTION OF VERTEBRAL FRACTURES UNDER
AXIAL COMPRESSION AND ANTERIOR FLEXION**

by

TIMOTHY MAXFIELD JACKMAN

B.S., Brigham Young University, 2010
M.S., Boston University, 2014

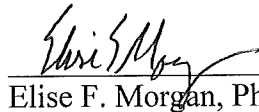
Submitted in partial fulfillment of the
requirements for the degree of
Doctor of Philosophy

2015

© 2015 by
TIMOTHY MAXFIELD JACKMAN
All rights reserved except for
Chapter 2, which is © 2014 Wiley

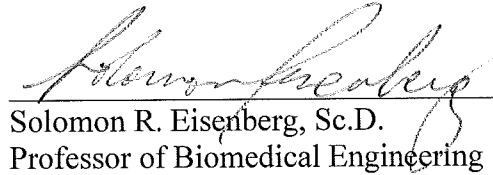
Approved by

First Reader



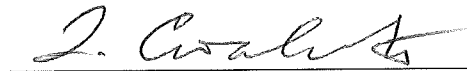
Elise F. Morgan, Ph.D.
Associate Professor of Biomedical Engineering

Second Reader



Solomon R. Eisenberg, Sc.D.
Professor of Biomedical Engineering

Third Reader




Dimitrije Stamenovic, Ph.D.
Associate Professor of Biomedical Engineering

Fourth Reader



Paul A. Barbone, Ph.D.
Associate Professor of Mechanical Engineering

Fifth Reader



Mary L. Bouxsein, Ph.D.
Associate Professor of Orthopaedic Surgery
Harvard Medical School

To Tommy and Maggie

ACKNOWLEDGEMENTS

Thank you to Alexander Adams, Dr. Paul Barbone, Dr. Glenn Barest, David Berry, Andy Camp, Cameron Curtiss, Rachel Danzig, Lidia De Barros, Alex DelMonaco, Joe Estano, Paul Fein, Dr. Amira Hussein, Corinne Jackman, Greg Janese, Kamil Makhnejia, Gabriel McDonald, Dr. Greg Miller, Dr. Elise Morgan, Charlotte Naylor, Sharon Roth, Bob Sjostrom, Dr. Ginu Unnikrishnan, and Zack Webster for your substantial contributions to this work.

**PREDICTION OF VERTEBRAL FRACTURES UNDER
AXIAL COMPRESSION AND ANTERIOR FLEXION**

TIMOTHY MAXFIELD JACKMAN

Boston University College of Engineering, 2015

Major Professor: Elise F. Morgan, Ph.D., Associate Professor of Biomedical
Engineering

ABSTRACT

Vertebral fractures affect at least 12–20% of men and women over the age of 50, and the risk of fracture increases exponentially with age. Despite their high prevalence, the failure mechanisms leading to these fractures are not well understood. For example, clinical observations of fractured vertebra often note that one or both vertebral endplates have collapsed, but the precise involvement of the endplates in the initiation and progression of failure has not yet been defined. The mechanisms of failure may also relate to spatial variations in the density and microstructure of the porous trabecular bone within the vertebra as well as to the health of the adjacent intervertebral discs (IVDs) which transfer loads directly to the vertebral endplates. Delineating the contributions of these factors would shed light on the etiology of vertebral fractures and would aid in development of clinically feasible, patient-specific finite element (FE) models of the vertebra. These models are built from a patient's quantitative computed tomography (QCT) scan and have shown tremendous promise for accurate, patient-specific estimates of bone strength and fracture risk. Further validation studies are required to assess the impact of the choices of material properties and boundary conditions, as a prerequisite for broad implementation of these FE models in clinical care.

The overall goal of this work was to define the failure processes involved in vertebral fractures and to evaluate the accuracy of patient-specific FE models in simulating these processes. Mechanical testing of human spine segments, in conjunction with micro-computed tomography, enabled the assessment of deformation at the vertebral endplate and deformation throughout the entire bone, as the vertebra was loaded to failure under both axial compression and anterior flexion. These data were compared against predictions of vertebral deformation obtained from QCT-based FE models. The impact of the choice of boundary conditions was specifically examined by comparing the accuracy of the FE predictions between models that simulated applied loads based on measured distributions of pressure within IVDs and models that used highly idealized boundary conditions.

The results of these studies demonstrated that sudden and non-recoverable endplate deflection is a defining feature of biomechanical failure of the vertebra, for both compression and flexion loading. The locations of endplate collapse as vertebral failure progressed were associated with the porosity of the endplate and the microstructure of the underlying trabecular bone. FE analyses incorporating the experimentally observed endplate deflections as boundary conditions provided more accurate predictions of displacements throughout the rest of the vertebra when compared to FE models with highly idealized boundary conditions. Under anterior flexion, the use of boundary conditions informed by measurements of IVD pressure mitigated, but did not eliminate, the inaccuracy of the idealized boundary conditions. No further improvement in accuracy was found when using boundary conditions based on pressure measurements

corresponding only to IVDs whose level of degeneration matched that observed in the IVDs adjacent to the vertebra being modeled. Overall, the accuracy of the FE predictions of vertebral deformation was only moderate, particularly near the locations of endplate collapse. The outcomes of this work indicate that the vertebral endplate is principally involved in vertebral fractures and that current methods for QCT-based FE models do not adequately capture this failure mechanism. These outcomes provide a biomechanical rationale for clinical diagnoses of vertebral fracture based on endplate collapse. These outcomes also emphasize that future studies of patient-specific FE models should incorporate physiologically relevant loading conditions and also material properties that more accurately represent the vertebral endplate in order to obtain higher fidelity predictions of vertebral failure.

TABLE OF CONTENTS

ACKNOWLEDGEMENTS.....	v
ABSTRACT.....	vi
TABLE OF CONTENTS.....	ix
LIST OF TABLES.....	xiii
LIST OF FIGURES.....	xv
LIST OF ABBREVIATIONS.....	xxvi
CHAPTER ONE.....	1
MOTIVATION.....	2
SPECIFIC AIMS.....	4
INTRODUCTION.....	4
Anatomy of the Vertebra.....	4
Anatomy of the Intervertebral Disc.....	6
Intervertebral Disc Degeneration.....	8
Non-Invasive Assessments of IVD Health.....	10
Vertebral Fractures.....	11
Vertebral Loading.....	14
Image-Guided Failure Analysis.....	15
QCT-Based FE Models.....	17
CHAPTER TWO.....	20

ENDPLATE DEFLECTION IS A DEFINING FEATURE OF VERTEBRAL FRACTURE AND IS ASSOCIATED WITH PROPERTIES OF THE UNDERLYING TRABECULAR BONE	21
INTRODUCTION	21
METHODS	23
Specimen Preparation	23
Mechanical Testing and Imaging.....	23
Endplate Deflection	24
Subchondral Trabecular Microstructure and Endplate Volume Fraction.....	26
IVD Histology and Grading.....	28
Statistical Analyses	31
RESULTS	32
DISCUSSION.....	36
CHAPTER THREE	40
DEVELOPMENT OF A POLYURETHANE CALIBRATION LAYER TO FUNCTION AS A MULTI-AXIAL LOAD CELL.....	41
INTRODUCTION	41
ASSEMBLY	43
MECHANICAL TESTING AND IMAGE ANALYSIS.....	45
MATERIAL MODELING.....	48
VALIDATION.....	51
CHAPTER FOUR.....	53

EXPERIMENTAL MEASUREMENT OF PROGRESSION OF VERTEBRAL	
FRACTURES	54
INTRODUCTION	54
METHODS	57
Specimen Preparation	57
Mechanical Testing and Imaging.....	59
Endplate Deflection	62
Digital Volume Correlation	62
Subchondral Trabecular Microstructure and Endplate Volume Fraction.....	65
Statistical Analyses	65
RESULTS	66
Anterior Flexion.....	66
Axial Compression.....	79
DISCUSSION.....	86
CHAPTER FIVE	93
ACCURACY OF QCT-BASED FINITE ELEMENT PREDICTIONS OF VERTEBRAL	
FRACTURE UNDER AXIAL COMPRESSION AND ANTERIOR FLEXION	94
INTRODUCTION	94
METHODS	96
Specimen Preparation	96
Mechanical Testing and Imaging.....	96
Digital Volume Correlation	97

IVD Grading	98
Nonlinear FE Analyses	99
Intradiscal Pressure Measurements.....	102
Boundary Conditions	105
Statistical Analyses	108
RESULTS	109
Anterior Flexion.....	109
Axial Compression.....	117
Yield Criterion	122
DISCUSSION	122
CHAPTER SIX.....	129
CONCLUSIONS.....	130
FUTURE WORK.....	134
BIBLIOGRAPHY.....	137
CURRICULUM VITAE.....	155

LIST OF TABLES

Table 2.1 Ultimate force (in N) and the drop in force occurring after the ultimate point (in N and as a percentage of the ultimate force): values presented are mean \pm standard deviation (SD), minimum and maximum for the 10 specimens.	33
Table 2.2 Maximum endplate deflection measured before and after the load drop and increase in deflection between these two load increments, expressed in mm and as a percentage of the height of the vertebral body: values presented are mean \pm standard deviation (SD), minimum and maximum for the 10 specimens.	33
Table 4.1 Anterior flexion: Force (in N) and Moment (in Nm) at the peak of loading and the drop in force (in N and as a percentage of the ultimate force) and moment (in Nm and as a percentage of the ultimate moment) occurring after the peak of loading: values presented are mean \pm standard deviation (SD), minimum and maximum for the 14 specimens.	69
Table 4.2 Anterior flexion: Maximum endplate deflection measured at and immediately after the peak of loading and increase in deflection between these two load increments, expressed in mm and as a percentage of the height of the vertebral body: values presented are mean \pm standard deviation (SD), minimum and maximum for the 14 specimens.	69
Table 4.3 Anterior flexion: Maximum anterior displacement in the anterior direction measured at and immediately after the peak of loading and increase in displacement between these two load increments, expressed in mm and as a percentage of the maximum endplate deflection in the corresponding specimen and load increment:	

values presented are mean \pm standard deviation (SD), minimum and maximum for the 14 specimens. 73

Table 4.4 Axial compression: Experimentally measured ultimate force (in N) and the drop in force occurring after the ultimate point (in N and as a percentage of the ultimate force) for the axial compression set: values presented are mean \pm standard deviation (SD), minimum and maximum for the 14 specimens. 80

Table 4.5 Axial compression: Maximum endplate deflection measured before and after the load drop and increase in deflection between these two load increments, expressed in mm and as a percentage of the height of the vertebral body: values presented are mean \pm standard deviation (SD), minimum and maximum for the 14 specimens of the axial compression set. 80

LIST OF FIGURES

Figure 1.1 (A) The human spine showing thoracic and lumbar levels of interest, T7–T9, T12–L2, and L2–L4.⁸⁰ (B) The human vertebra, viewed from above.⁸⁰ 5

Figure 1.2 Left: Schematic view of spine segment and intervertebral disc.¹²⁷ The figure shows the organization of the disc with the nucleus pulposus (NP) surrounded by the lamellae of the annulus fibrosus (AF) and separated from the vertebral bodies (VB) by the cartilaginous endplate (CEP). Right: Photomicrograph of L5 vertebra from a 6-month-old rabbit;⁶⁹ H&E staining, original magnification: 100x. N = nucleus pulposus; AF = annulus fibrosus; CP = cartilaginous endplate; BP = bony endplate. 6

Figure 1.3 (a) Schematic showing the structure of the intervertebral disc.⁵⁵ (b) Schematic showing fixed negative charge from extracellular matrix. PG indicates proteoglycan.⁵⁵ 7

Figure 1.4 Sagittal sections demonstrating macroscopic appearances of healthy (top) and degenerated (bottom) IVDs..... 9

Figure 1.5 Stress profiles along mid-sagittal line of a healthy IVD (left) and degenerated IVD (right).² 10

Figure 1.6 Classification of fractures based on location in the sagittal plane and the severity of the height reduction.³⁴ 12

Figure 1.7 Appearance of vertebral endplates in a normal vertebra as assessed with the algorithm-based approach for the qualitative identification of vertebral fracture.⁵⁸ A clinical fracture would feature the central endplate depressed below the ring apophysis..... 13

Figure 1.8 Sequence of six radiographs taken at successive stages of compression showing the endplate bulge and fail by permanent deformation. ⁴²	13
Figure 1.9 Variation of the load fraction carried by the cortical shell across transverse slices within two specimens representing high and low variation in load fraction, ²⁹ The trabecular bone load fraction equals the inverse of the shell load fraction at each position.....	14
Figure 1.10 (A) Sagittal cut view of QCT image stack. (B) Mask applied to QCT images to isolate vertebra. (C) Voxel-based FE model; BMD values for each element are derived from calibrated QCT images.....	19
Figure 2.1 Experimental procedure for mechanical testing and imaging	24
Figure 2.2 Sagittal half-section of vertebra before loading (gray) and after failure (blue): Endplate deflection was defined as the vertical movement of the endplate between registered images.	25
Figure 2.3 Above: Transverse slice of vertebra with an overlay of the VOIs used for quantification of trabecular microstructure and $Ep.BV/TV$. Below: cross sectional view of the VOIs.....	27
Figure 2.4 ALDI scoring: Shown at the left in each of the three rows is a transverse QCT slice of the IVD (acquired prior to mechanical testing). The ALDI score is shown at the top left. Yellow, orange, and red regions are portions of the endplates and calcification within the IVD; no osteophytes were present in the QCT images of the mid-sections of these three IVDs. Shown at the top and bottom right in each row are	

<p>a corresponding optical image and histological section (FAST staining⁷⁵), respectively, of a sagittal cross-section (acquired after mechanical testing).</p>	30
<p>Figure 2.5 VOI distance is defined as the in-plane distance from site of initial deflection to the center of a given VOI used for evaluating trabecular microstructure. Yellow indicates areas of higher endplate deflection, while red indicates areas with little or no deflection.....</p>	32
<p>Figure 2.6 (A–E) Axial deflection (negative values indicate downward movement) in the superior endplate for the six loading increments labeled on the load-displacement curve. For this vertebra, increment C is the increment of marked increase in endplate deflection. (F) Endplate deflection after unloading. (G) ρ_{app} for each VOI of subchondral trabecular bone. The deflection colorscale is non-linear, and the red image above the abscissa is the QCT image used for ALDI scoring.....</p>	34
<p>Figure 2.7 Maximum endplate deflection for each specimen at loading increments leading up to and immediately after the drop in the load-displacement curve.</p>	34
<p>Figure 2.8 Regions of large endplate deflection (outlined in blue and red), defined as >0.5 mm, and (A) distribution of SMI in the VOIs of subchondral bone (grayscale) or (B) distribution of Ep.BV/TV in the VOIs of subchondral endplate (grayscale): The lightest blue outline corresponds to the increment at which endplate deflection clearly initiated. The boundaries at subsequent increments are represented with progressively darker shades of blue. The red outline corresponds to the unloaded scan. SMI values typically range from 1 (plate-like trabeculae) to 3 (rod-like trabeculae) and can include values up to 4 (sphere-like trabeculae).</p>	35

Figure 3.1 Schematic of experimental apparatus for testing spine segments under anterior flexion	42
Figure 3.2 Assembly schematic for calibration layer	44
Figure 3.3 Mid-sagittal cross-sections of the calibration layer loaded under 0, 1, 2, 3, and 4 kN with a red line superimposed over the stack of aligned images to mark the unloaded profile of the calibration layer; A color map was applied to the images to improve visualization: red corresponds to the high attenuating PVC plates while the dark blue corresponds to air.....	44
Figure 3.4 Preconditioning cycles for the calibration layer before and after mechanical testing.....	46
Figure 3.5 Procedure to interpolate PVC surface from original filtered and segmented data; The gap in the outer ring corresponds to a notch cut into the PVC plate to interface with a pin in the loading device that prevented any rotational movement.	46
Figure 3.6 Mid-sagittal cross section of the calibration layer featuring bowing in the PVC potting tray. The user identifies where the PVC surface intersects with each green line.....	47
Figure 3.7 A) Mid-sagittal cross section of the calibration layer, imaged using μ CT; B) 3-D view of half-section of FE model, with the color map corresponding to axial displacements obtained at the surfaces by tracking the position of the PVC potting tray and plate, and elsewhere by FE analysis; C) Schematic of distributed load at superior surface of calibration layer and the corresponding reaction force (R_F) and moment (R_M) about the center of mass.	47

Figure 3.8 Force-displacement curves of 40A polyurethane loaded under axial compression in unconfined compression for four cycles. To reduce friction as much as possible, the polyurethane was lubricated on the surfaces that interfaced with the hydraulic compressor.	50
Figure 3.9 Force-relaxation curves for 40A polyurethane loaded under 1, 2, 3, and 4 kN of axial force.	50
Figure 3.10 Comparison between experimentally measured and simulated force on the polyurethane calibration layer.....	52
Figure 4.1 Schematic of dissected T7–T9 spines segment for mechanical testing under either axial compression or axial compression with anterior flexion	58
Figure 4.2 Schematic of experimental apparatus for testing spine segments under anterior flexion; The compression screw and flexion screw applied the axial compression and angle, respectively, of each step, while the level screws ensured that the angle was only applied in the sagittal plane.	61
Figure 4.3 Schematic for generating the 3-D, irregularly shaped mesh that was applied to aligned images for digital volume correlation.	64
Figure 4.4 For anterior flexion: (Top) Lateral radiographic views (created from μ CT); (Middle) Sagittal half-section of vertebra before loading (gray) and at load increment (blue) noted on the load-displacement and moment-angle curve; (Bottom) For increments A–C, three-quarter section views of experimental displacement field in axial direction; positive values indicate downward displacement. The arrow indicates the site of initial deflection.	68

Figure 4.5 For anterior flexion: (Top) Lateral radiographic views (created from μ CT); (Middle) Sagittal half-section of vertebra before loading (gray) and at load increment (blue) noted on the load-displacement and moment-angle curve; (Bottom) For increments A–C, three-quarter section views of experimental displacement field in axial direction; positive values indicate downward displacement. The arrow indicates the site of initial deflection. 70

Figure 4.6 Axial force (dashed blue) and anterior moment (solid green) curves for four cases observed during mechanical testing; The vertical red line indicates the increment that corresponds to the peak of loading. 71

Figure 4.7 Experimental displacement fields in axial and anterior/posterior direction for a T8 vertebra featuring (A) initial deformation at the central endplate and (B) initial deformation at the anterior ring apophysis; Positive values in the axial direction indicate downward displacement and negative values in the anterior/posterior direction indicate anterior displacement. 74

Figure 4.8 Three-quarter section views of experimental displacement fields in axial and anterior/posterior directions at and immediately after the peak of loading for a representative specimen loaded under anterior flexion; Positive values in the axial direction indicate downward displacement and negative values in the anterior/posterior direction indicate anterior displacement. 75

Figure 4.9 Maximum deflection in the superior endplate (top) and maximum anterior bulge (bottom) prior to, at, and after the peak of loading for all specimens loaded under anterior flexion; Each specimen has a unique marker. 76

Figure 4.10 Linear regression of the maximum deflection in the superior endplate and maximum anterior bulge in the anterior cortex after the peak of loading for all specimens loaded under anterior flexion ($R^2 = 0.385$, $p = 0.0179$). 77

Figure 4.11 Regions of large endplate deflection (outlined in blue and red), defined as $>0.5\text{mm}$, and (above) distribution of apparent density in the VOIs of subchondral bone (grayscale) or (below) distribution of Ep.BV/TV in the VOIs of subchondral endplate (grayscale): The lightest blue outline corresponds to the increment at which endplate deflection clearly initiated. The boundaries at subsequent increments are represented with progressively darker shades of blue. The red outline corresponds to the unloaded scan. 78

Figure 4.12 For axial compression: (Top) Lateral radiographic views (created from μCT); (Middle) Sagittal half-section of vertebra before loading (gray) and at load increment (blue) noted on the load-displacement curve; (Bottom) For increments A–C, three-quarter section views of experimental displacement field in axial direction; positive values indicate downward displacement. 81

Figure 4.13 Maximum deflection in the superior endplate prior to, at, and after the ultimate point for all specimens loaded under axial compression; Each specimen has a unique marker..... 82

Figure 4.14 Axial deflection (negative values indicate downward movement) in the endplate at and immediately following the ultimate point for a representative case of initial endplate deflection at (A) the anterior ring apophysis, (B) the anterior central endplate, (C) the medial central endplate, (D) the mediolateral ring apophysis, and

(E) the posterior ring apophysis. The deflection colorscale is nonlinear, and the center of each site of initial deflection was used for qualitative comparison in Figures 4.16 and 4.18..... 83

Figure 4.15 Three-quarter section views of experimental displacement fields in axial and lateral directions at and immediately after the ultimate point for a representative specimen loaded under axial compression; Positive values in the axial direction indicate downward displacement and positive values in the lateral direction indicate displacement towards the left..... 85

Figure 4.16 Relative location of the center of the initial endplate deflection site for spine segments loaded under axial compression and anterior flexion 89

Figure 4.17 Vertebral strength vs. bone mineral density multiplied with cross sectional area for T8 ($R^2 = 0.70$) and L1 ($R^2 = 0.82$) vertebrae, as determined by examining the bone mineral density and transverse area of the largest elliptical cylinder that fit in the centrum of the vertebral body; The T8 vertebrae featured an intact neural arch, whereas all posterior elements were removed from the L1 vertebrae. 89

Figure 4.18 Relative location of the center of the initial endplate deflection site for T8 and L1 vertebrae loaded to failure under axial compression; The posterior elements of the L1 vertebrae were removed (Chapter 2) while the T8 vertebrae featured an intact neural arch and zygapophysial joints 90

Figure 5.1 Procedure to develop specimen-specific, QCT-based FE models..... 102

Figure 5.2 Yield surface of the crushable foam material model with the parameters that define the shape..... 102

Figure 5.3 Photograph of spine segment with apparatus developed to obtain intradiscal pressure measurements; Image courtesy of Alex DelMonaco.....	104
Figure 5.4 (Left) Measured mid-sagittal pressure profiles [7] averaged for moderately healthy (ALDI=0–1), degenerated (ALDI=2), and all (ALDI=0–2) IVDs loaded under anterior flexion. (Right) Color maps of the distributed load across the superior endplate for (A) Experimentally Matched, (B) Idealized, (C) IVD-Generic, and (D) IVD-Specific boundary conditions for the anterior flexion set.	106
Figure 5.5 (Left) Measured mid-sagittal pressure profiles [7] averaged for moderately healthy (ALDI=0–1), degenerated (ALDI=2), and all (ALDI=0–2) IVDs loaded under axial compression. (Right) Color maps of the distributed load across the superior endplate for (A) Experimentally Matched, (B) Idealized, (C) IVD-Generic, and (D) IVD-Specific boundary conditions for the axial compression set.	107
Figure 5.6 For anterior flexion: (A) Three-quarter section view of a representative T8 vertebral body before loading (gray) and at the load increment following peak of loading (blue); (B–J) Three-quarter section views of experimental and FE axial displacements (positive values are down-ward displacements) at the load increment following peak of loading for crushable foam (C–F) and von Mises (G–J) FE analyses.	110
Figure 5.7 Linear regression performed on transformed experimental and FE-computed displacements for all boundary conditions from a representative specimen loaded under anterior flexion.....	111

Figure 5.8 Crushable foam FE analyses: R^2 values for regressions of FE-computed vs. measured displacements of the anterior flexion set for all four boundary conditions. The color corresponds to ALDI score (blue=0, black=1, red=2), and for a given ALDI score each specimen is indicated with a different symbol. 112

Figure 5.9 von Mises FE analyses: R^2 values for regressions of FE-computed vs. measured displacements of the anterior flexion set for all four boundary conditions. The color corresponds to ALDI score (blue=0, black=1, red=2), and for a given ALDI score each specimen is indicated with a different symbol. 113

Figure 5.10 Median percent error for FE-computed axial displacements compared to experimental data using crushable foam FE yield criterion for specimens loaded under anterior flexion. The color corresponds to ALDI score (blue=0, black=1, red=2), and for a given ALDI score each specimen is indicated with a different symbol. 114

Figure 5.11 FE-computed axial force for each specimen loaded under anterior flexion plotted against experimental force 115

Figure 5.12 FE-computed moment for each specimen loaded under anterior flexion plotted against experimental anterior moment. 116

Figure 5.13 For axial compression: (A) Three-quarter section view of a representative T8 vertebral body before loading (gray) and at the load increment following peak of loading (blue); (B–J) Three-quarter section views of experimental and FE axial displacements (positive values are down-ward displacements) at the load increment

following peak of loading for crushable foam (C–F) and von Mises (G–J) FE analyses	118
Figure 5.14 Crushable foam FE analyses: R^2 values for regressions of FE-computed vs. measured displacements of the axial compression set for all four boundary conditions. The color corresponds to ALDI score (blue=0, black=1, red=2), and for a given ALDI score each specimen is indicated with a different symbol.	119
Figure 5.15 von Mises FE analyses: R^2 values for regressions of FE-computed vs. measured displacements of the axial compression set for all four boundary conditions. The color corresponds to ALDI score (blue=0, black=1, red=2), and for a given ALDI score each specimen is indicated with a different symbol.	119
Figure 5.16 Median percent error for FE-computed axial displacements compared to experimental data using crushable foam FE yield criterion for specimens loaded under axial compression. The color corresponds to ALDI score (blue=0, black=1, red=2), and for a given ALDI score each specimen is indicated with a different symbol.....	120
Figure 5.17 FE-computed axial force for each specimen loaded under axial compression plotted against experimental force.....	121

LIST OF ABBREVIATIONS

AF	Annulus Fibrosus
ALDI	Apparent Loss of Disc Integrity
ANOVA	Analysis of Variance
BMD	Bone Mineral Density
BV/TV	Volume Fraction
CF	Crushable Foam
ConnD	Connectivity Density
DA	Degree of Anisotropy
DVC	Digital Volume Correlation
Ep.BV/TV	Endplate Volume Fraction
FE	Finite Element
GAG	Glycosaminoglycan
IVD	Intervertebral Disc
MLE	Maximum Likelihood Estimation
MRI	Magnetic Resonance Imaging
NP	Nucleus Pulposus
PMMA	Polymethyl Methacrylate
PVC	Polyvinyl Chloride
QCT	Quantitative Computed Tomography
SMI	Structural Model Index
Tb.N*	Trabecular Number

Tb.Sp*	Trabecular Separation
VM	von Mises
VOI	Volume of Interest
μ CT	Micro-Computed Tomography
ρ_{app}	Apparent Density

CHAPTER ONE

MOTIVATION

Vertebral fractures affect at least 12–20% of men and women over the age of 50^{41,86,95}, and the risk of fractures increases exponentially with age⁶². These fractures are also notable for their high associated mortality¹⁴ and poorly defined pathogenesis.¹⁵ Vertebral fracture is a strong predictor for future fractures in the spine, hip, and wrist, even after adjusting for bone mineral density^{33,40,77,110}. The development of osteoporosis—defined by a loss of bone mass and deteriorated bone microstructure—is a common factor leading to fracture.¹⁶ Degeneration of the adjacent intervertebral disc (IVD) may also influence vertebral failure by altering the normal loading experienced by the vertebra.^{3,132} The prevalence of age-related factors leading to fracture^{85,95} suggests that vertebral fractures will continue to have a significant impact on the aging population.

While the incidence of vertebral fractures is the highest of any osteoporotic fractures,¹³ the mechanisms that initiate and propagate damage in the vertebra remain poorly understood. Deflection in the vertebral endplates has been associated with vertebral failure,^{8,42} but the relationship between endplate deflection and vertebral failure is unclear. Further, how vertebral loading (*i.e.*, bending or compression loads) may impact the role of the endplate in the onset and progression of deformation towards a clinical fracture pattern has not yet been examined. Understanding the mechanisms failure in the vertebra may provide valuable insight for fracture prevention and management.

Sites of initial failure in the vertebra and the progression of deformation into a clinical fracture pattern can be examined by images acquired before and after a fracture

has developed. Full-field, experimental measurement of displacements throughout a vertebra imaged before and after loading has been used to identify failure patterns in vertebrae loaded under axial compression.^{47,48} These measurements, obtained by applying digital volume correlation (DVC) to the image series,^{5,48,74} have not been studied for vertebrae loaded under anterior bending loads. Experimentally obtained displacement fields throughout the vertebra would provide new insights into how the loading mode applied to the spine segment affects the mechanisms of failure in the vertebra. Further, these displacement fields can be used to assess the accuracy of finite element (FE) analyses.

FE models based on quantitative computed tomography (QCT) have shown tremendous promise for accurate, patient-specific estimates of fracture,^{18,20,52,97,131,139} but the improvement of these models over traditional bone mineral density (BMD) measures has not yet been established. Preliminary findings as part of an ongoing study in our laboratory suggest that accurate boundary conditions representing realistic loading conditions are critical to improving predictions of vertebral failure.⁴⁷ However, obtaining accurate loading conditions that are physiologically relevant remains a critical barrier to progress. Measurements of pressure within the IVDs adjacent to the vertebra can provide a useful estimate of these loading conditions, and these pressures have been shown to change with IVD degeneration.^{3,101} Thus, non-invasive assessments of IVD health may provide information on vertebra loading, and this information could be used to formulate boundary conditions for FE simulations of vertebral failure.

The overall goal of this work was to define the failure processes involved in vertebral fractures and evaluate the accuracy of patient-specific FE models in simulating these processes. The outcomes of this research are anticipated to yield new insights into the initiation and propagation of vertebral failure, and to provide a clinically relevant technique to obtain realistic boundary conditions for accurate, patient-specific prediction of vertebral failure.

SPECIFIC AIMS

- Investigate the relationship between endplate deflection and vertebral failure, with emphasis on associations between endplate deflection and characteristics of the neighboring subchondral bone and IVD.
- Experimentally measure deformation patterns and vertebral strength in axial compression and compression with anterior flexion.
- Predict vertebral failure and deformation patterns using QCT-based FE models when boundary conditions are based on experimental measurements of endplate deflection and measured distributions of pressure within IVDs and determine the accuracy of the simulated vertebral strength and displacement fields to the experimental data from Aim #2.

INTRODUCTION

Anatomy of the Vertebra

The primary mechanical functions of vertebrae are to protect the spinal cord and to support loads transferred through adjacent IVDs and muscle activity (Figure 1.1A).

The vertebra (Figure 1.1B) is composed of the vertebral body and the posterior elements

(pedicles, spinous process, lamina, and transverse process for lumbar vertebrae). The posterior elements are mostly cortical bone, while the vertebral body consists of trabecular bone with a thin, outer shell (known as the cortex) of cortical bone. Trabecular bone in the vertebral body exhibits spatial variation in density and architecture; such heterogeneity has a significant impact on vertebral strength.⁵⁰

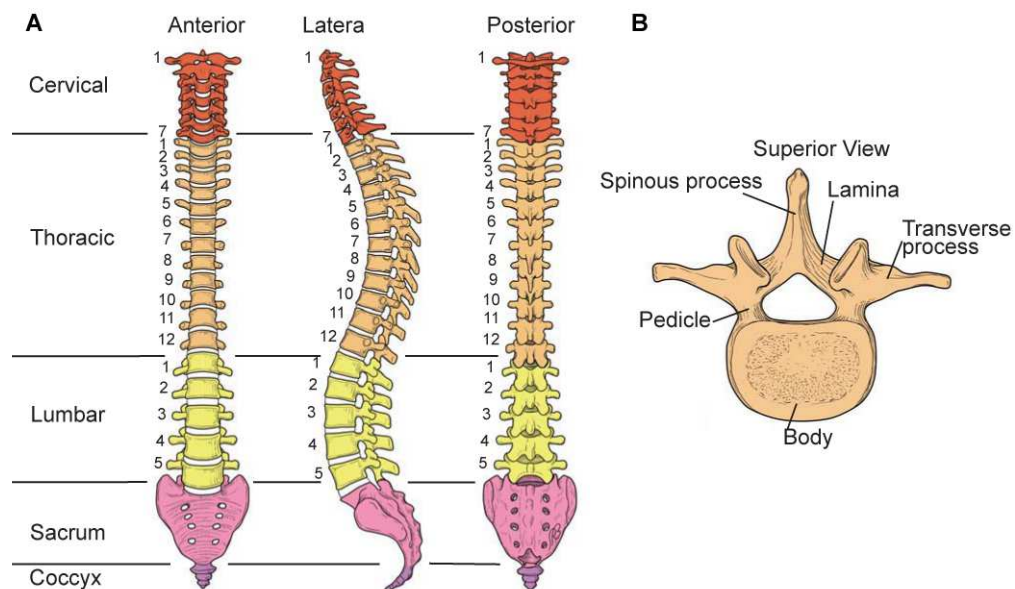


Figure 1.1 (A) The human spine showing thoracic and lumbar levels of interest, T7–T9, T12–L2, and L2–L4.⁸⁰ (B) The human vertebra, viewed from above.⁸⁰

Vertebral endplates are thin plates of bone and hyaline cartilage that mark the superior and inferior boundary between the vertebral body and IVD (Figure 1.2). The bony endplate is perforated with small pores that allow diffusion across the endplate between the avascular IVD and the vascular network in the vertebra.^{107,108} The cartilaginous endplate prevents disc tissue from penetrating through the endplate pores¹¹³ and facilitates nutrient transport into the IVD from adjacent blood vessels.^{106,127} The

endplate is thought to be the weakest and most easily damaged component of the spine. The superior endplate is thought to be more commonly fractured because it is thinner and supported by less-dense trabecular bone than the inferior endplate.¹³⁸

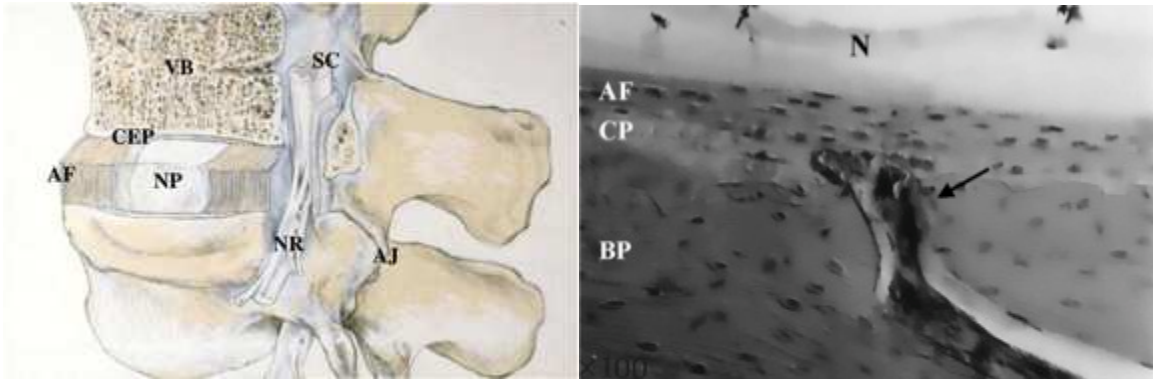


Figure 1.2 Left: Schematic view of spine segment and intervertebral disc.¹²⁷ The figure shows the organization of the disc with the nucleus pulposus (NP) surrounded by the lamellae of the annulus fibrosus (AF) and separated from the vertebral bodies (VB) by the cartilaginous endplate (CEP). Right: Photomicrograph of L5 vertebra from a 6-month-old rabbit;⁶⁹ H&E staining, original magnification: 100x. N = nucleus pulposus; AF = annulus fibrosus; CP = cartilaginous endplate; BP = bony endplate.

Anatomy of the Intervertebral Disc

The IVD is a fibrocartilaginous structure between two vertebral bodies that provides mobility to the spinal column (Figure 1.1A) and distributes forces over the surfaces of the adjacent endplates. The IVD (Figure 1.3A) is composed of two primary components: the nucleus pulposus (NP) and annulus fibrosus (AF). The NP is a gelatinous structure dense with proteoglycans. These hydrophilic proteins have a strong, negative, fixed charge (Figure 1.3B) that draws water into the NP (and to a lesser extent, the AF) and creates an

internal swelling pressure.¹¹¹ Swelling is the primary load-bearing mechanism in the NP, regardless of degeneration.⁶⁰ In a healthy disc, approximately 80% of the NP is water, whereas the outer AF is about 60% water.¹²⁸ In degenerated discs, the water content was observed to decrease 5–10% in the NP and inner AF.⁷⁹ The AF is an organized structure of collagen layers called lamellae that surround the NP. The encircling lamellae, oriented in alternating directions, withstand the forces applied by a compressed NP and/or from the adjacent vertebra directly.^{93,94}

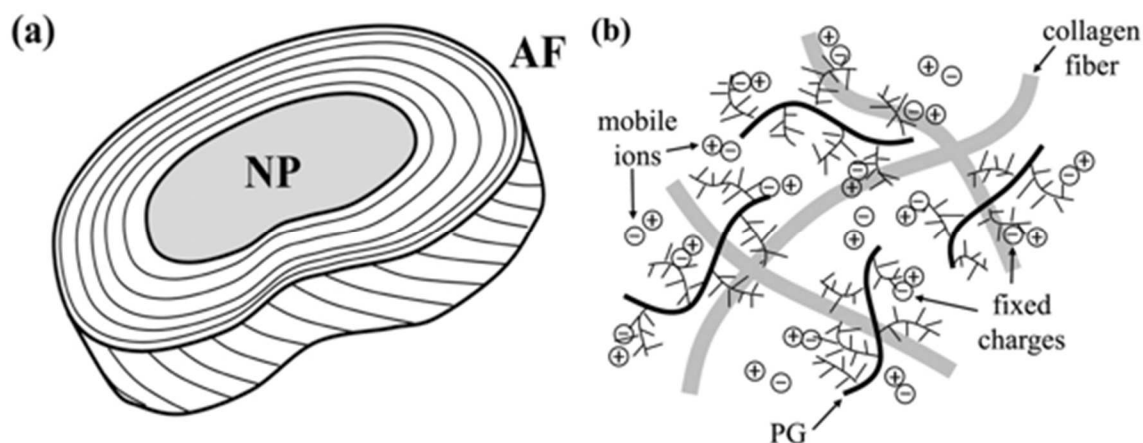


Figure 1.3 (a) Schematic showing the structure of the intervertebral disc.⁵⁵ (b) Schematic showing fixed negative charge from extracellular matrix. PG indicates proteoglycan.⁵⁵

The boundary between the NP and AF is not clearly defined. Early researchers often viewed the NP as a separate entity bound by the AF and cartilaginous endplate;⁵³ Other work suggested some connection through a poorly organized structure.¹⁰⁷ The transition between these two regions is unclear, and becomes even more so with degeneration. Recent studies, however, have demonstrated that the NP contains a highly structured network of fibers that integrate with the inner annulus.¹³⁰ Furthermore,

microscopic examination has revealed nucleus fibers inserting into the cartilaginous endplate.¹²⁹ The connectivity between the NP, AF, and endplate indicates that the NP should be viewed as a separate entity but rather as an integrated structure with adjacent tissue.

The IVD maintains a balance between externally applied loads and internal osmotic pressure; this equilibrium is altered as loads are applied or removed during daily activities. Depending on the concentration gradient across the tissue membrane, osmotic pressure can act to expand or contract the IVD. The ionic concentration surrounding the tissue has a significant impact on the mechanical behavior of articular cartilage and other connective tissues.²⁷ Biomechanical testing conditions of IVDs must be carefully considered to provide physiologically comparable circumstances. A solution with a high or low osmolarity would affect IVD hydration and, therefore, dramatically affect the mechanical behavior.¹⁰³

Intervertebral Disc Degeneration

With increasing age, IVDs tend to exhibit degenerative changes (Figure 1.4). Degeneration of IVDs is strongly associated with back pain²² and affects approximately 60% of the population by age 70.^{4,87} With degeneration, IVDs often experience reduced glycosaminoglycan (GAG) levels,¹¹² NP pressure^{2,84,126} and disc height^{73,100} and becoming more fibrous.⁶ IVD degeneration initiates with dehydration in the NP,¹² which decreases swelling pressure and progresses to a loss of demarcation between the NP and AF as well as to decreased disc height.^{6,100,119} Under axial compression, healthy IVDs maintain approximately uniform pressure across the NP, but in degenerated IVDs, the

pressure distribution becomes less uniform (Figure 1.5), and the regions of high pressure shift from the NP to the AF.² Other visible signs of degeneration include fissures and tears in both the NP and AF,¹¹⁹ osteophytes at the vertebral margin,⁷³ and a loss of demarcation between the NP and AF.^{6,119} When compared to motion segments (defined as a single IVD with both adjacent vertebra) with healthy IVDs, those with degenerated IVDs exhibit less spatial variation in stiffness of the neighboring bone along the mid-sagittal plane.⁶⁷ These studies demonstrate that degeneration alters the intradiscal pressure distribution in the IVD and that this alteration may impact the loading profile across the adjacent endplate, causing the underlying trabecular bone to adapt to the new mechanical environment. Thus, IVD health may play a role in the mechanisms of vertebral failure, via effects on vertebral loading and/or trabecular microstructure.

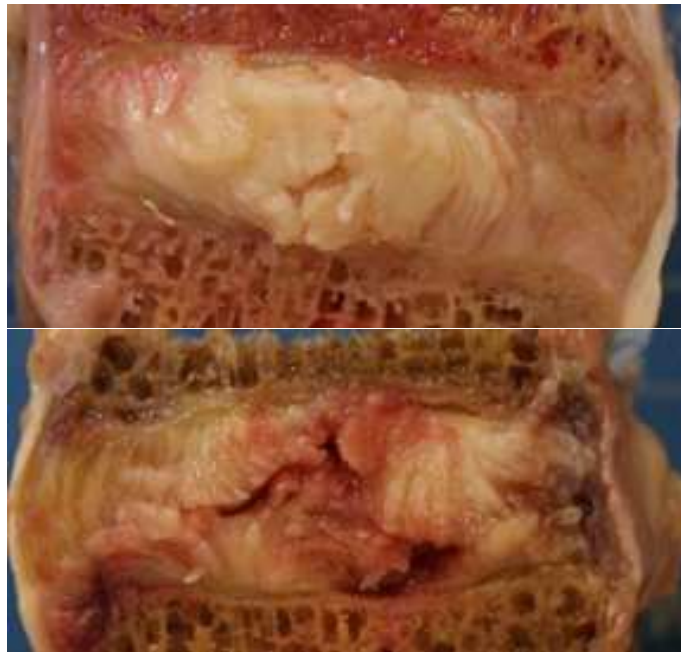


Figure 1.4 Sagittal sections demonstrating macroscopic appearances of healthy (top) and degenerated (bottom) IVDs.

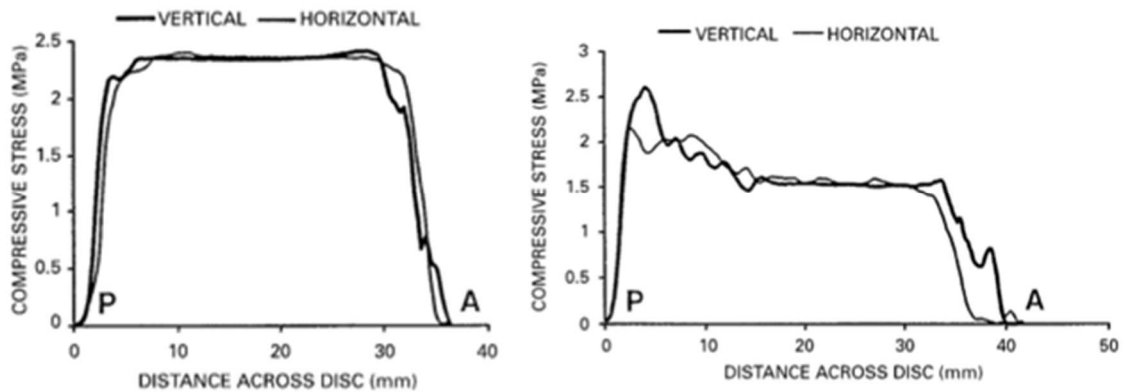


Figure 1.5 Stress profiles along mid-sagittal line of a healthy IVD (left) and degenerated IVD (right).²

Non-Invasive Assessments of IVD Health

Several non-invasive methods exist for evaluating IVD health. Lane et al. developed a system to score discs from lateral radiographs.⁷³ This system was based on two defining features of disc degeneration: disc-space narrowing (a loss of IVD height) and the presence of osteophytes at the vertebral margin. This grading system, however, is limited by its inability to directly assess the overall health of the NP.

Pfirrmann et al. developed a reliable grading system using magnetic resonance imaging (MRI).¹⁰⁰ With MRI, the distinction between the NP and the AF has been shown to correlate directly with proteoglycan content, but not water or collagen content.^{28,98} MRI has been used to evaluate the height of the vertebral body and IVD in osteoporotic patients,¹²¹ measure the thickness of the cartilaginous endplate,⁸⁹ and visualize changes in the IVD-endplate interface and in the endplate (*i.e.*, Modic changes).⁷ It may be possible to track internal IVD deformations, with the image texture provided by the brighter NP and darker cartilaginous endplate.⁹⁴ If non-invasive techniques can reliably assess

proteoglycan content and, by extension, IVD degeneration, then these methods may also provide a useful estimate of the typical pressure distribution in the IVD for various degrees of degeneration.

Vertebral Fractures

With over 500,000 incident fractures reported in 2005 in the United States alone, vertebral fractures are the single most common type of osteoporotic fracture, and a majority (71%) vertebral fractures occur in women.¹³ Furthermore, older women with incident fractures have an increased risk of mortality.⁶³ Identifying patients with incident fractures, however, has been a subject of disagreement among clinicians: About one half of vertebral fractures may be asymptomatic and the natural variation in vertebral shape may confound the classification of mild fractures.²⁶ Genant et al. developed a classification system to diagnose vertebral fractures based on the relative distance between superior and inferior endplates at posterior, central, and anterior points of the vertebral body as assessed with a lateral radiograph (Figure 1.6).³⁴ Jiang et al. developed an algorithm-based approach for qualitative identification of vertebral fractures that assessed whether the whole endplate was depressed within the ring apophysis (Figure 1.7).^{31,58} While both clinical classifications^{31,58,59} and biomechanical studies^{39,42,99,109} identify endplate deflection as a frequent feature of vertebral fractures and deformities, it remains unclear whether vertebral fracture initiates with endplate deflection or whether endplate deflection is a secondary effect of the primary cause of vertebral fracture. Excessive endplate bulging and trabecular collapse have been reported to accompany endplate fractures (Figure 1.8).^{8,39,42} The underlying trabecular bone is widely agreed to

provide mechanical support to the endplate: near the endplate, the subchondral trabecular bone, and not the cortical shell, bears almost the entire load supported by the vertebral body (Figure 1.9).^{29,43} Regional variations in microstructure, stiffness, and strength have been observed in the underlying trabecular bone,^{45,66,115} and these properties also change with age and the development of osteoporosis.¹²⁰ Such variations in the mechanical behavior of the adjacent bone may affect both the initiation and progression of endplate deflection and, by extension, vertebral failure.

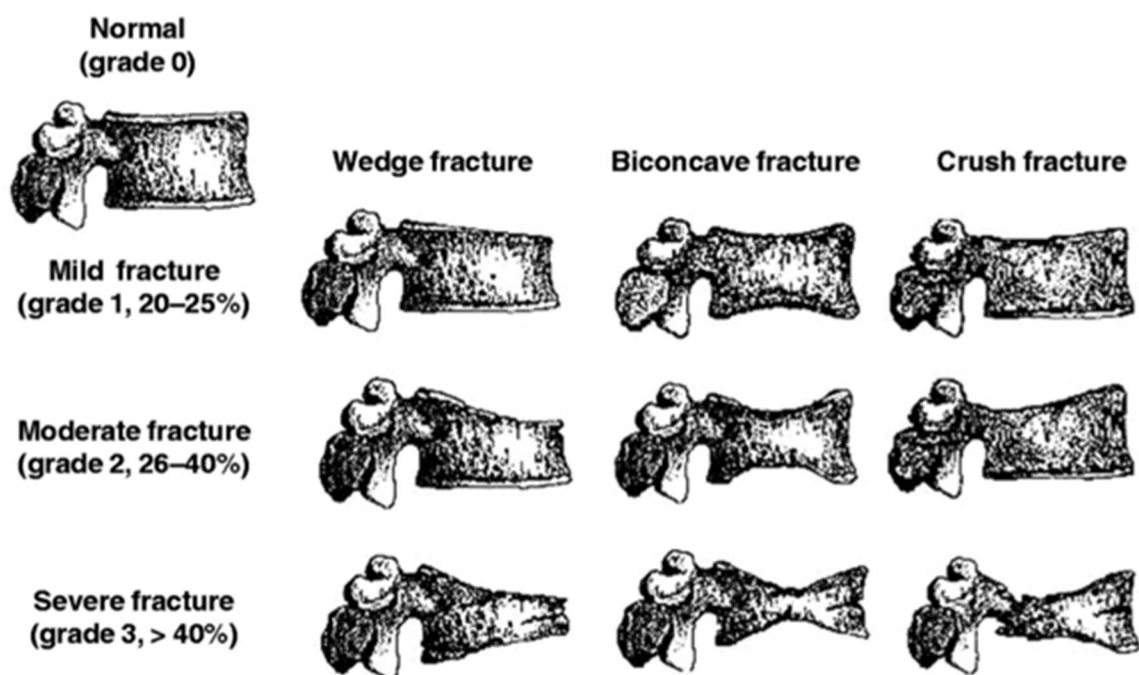


Figure 1.6 Classification of fractures based on location in the sagittal plane and the severity of the height reduction.³⁴

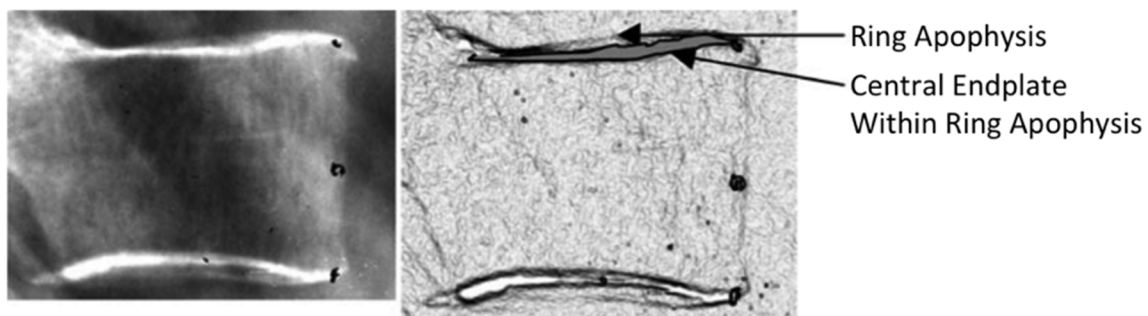


Figure 1.7 Appearance of vertebral endplates in a normal vertebra as assessed with the algorithm-based approach for the qualitative identification of vertebral fracture.⁵⁸ A clinical fracture would feature the central endplate depressed below the ring apophysis.

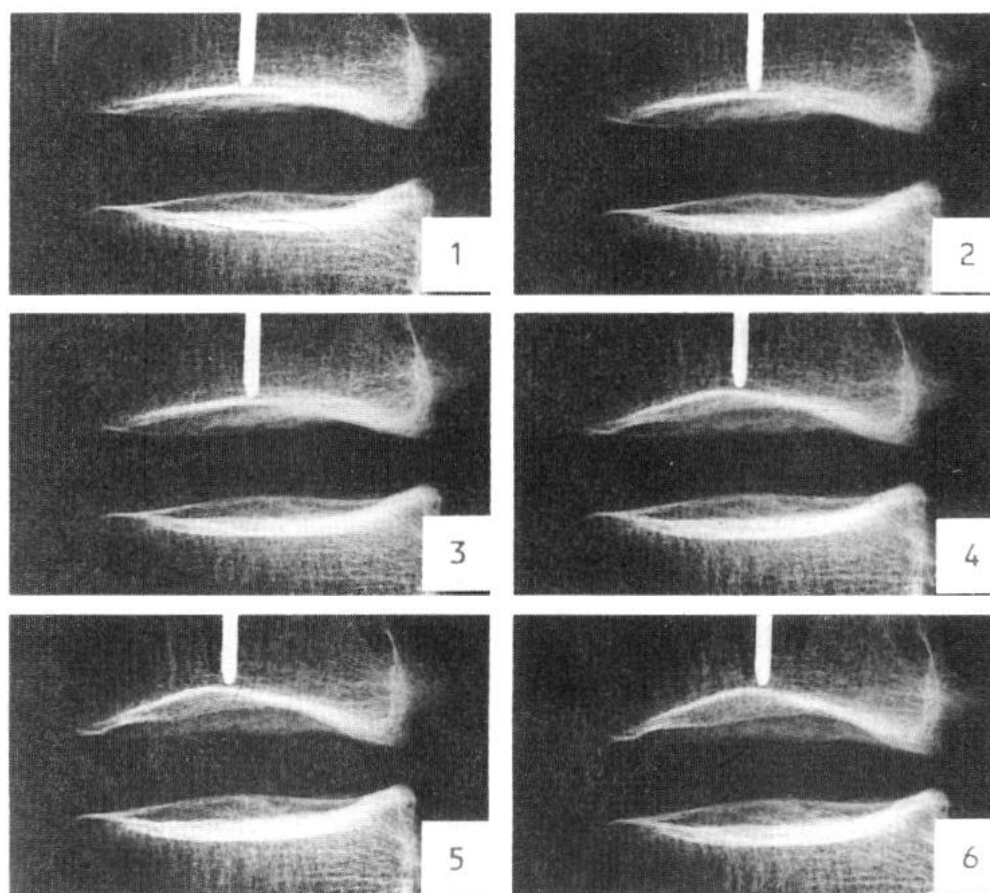


Figure 1.8 Sequence of six radiographs taken at successive stages of compression showing the endplate bulge and fail by permanent deformation.⁴²

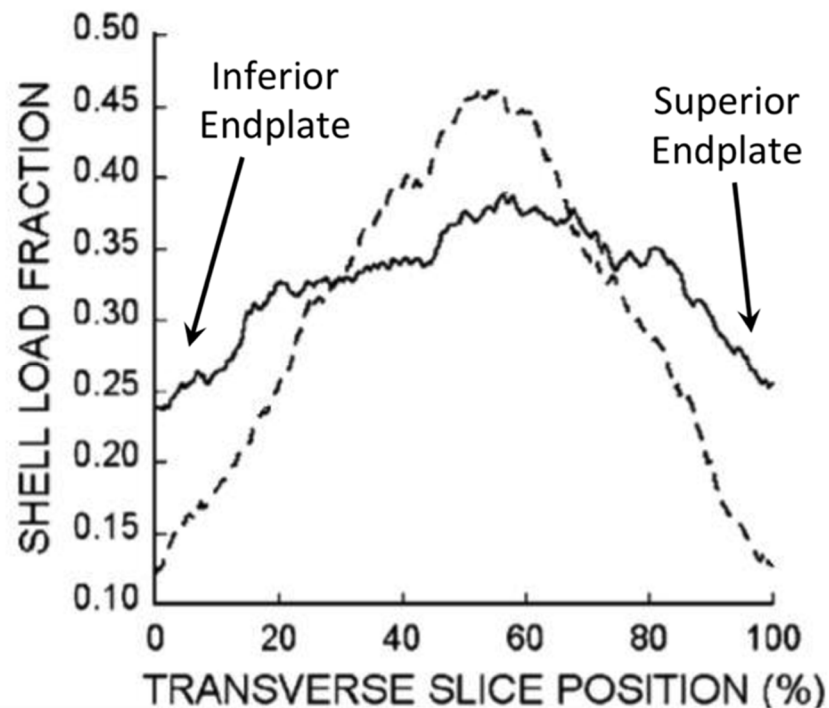


Figure 1.9 Variation of the load fraction carried by the cortical shell across transverse slices within two specimens representing high and low variation in load fraction,²⁹ The trabecular bone load fraction equals the inverse of the shell load fraction at each position.

Vertebral Loading

Vertebral fractures develop in several different patterns (*i.e.*, wedge, crush, biconcave fractures) that are thought to be associated with different loading conditions (Figure 1.6). Different *in vivo* loading conditions, such as anterior bending or axial compression, may produce different loading patterns across the endplates and, subsequently, different failure patterns through the underlying bone. Vertebral wedge fractures, fractures associated with anterior bending-type loading,^{10,134} are the most commonly observed fracture type.²⁶

Image-Guided Failure Analysis

Failure patterns in whole bones can be estimated by images acquired before and after a fracture has developed. Markers fixed to both hard and soft tissues can be tracked during mechanical testing by comparing images before and after loading to obtain local strain measurements based on the movements of the markers.^{46,116,117} Trabecular microstructure can be used as markers to track local deformations in whole bones, provided there is a way to image trabecular bone with sufficient resolution. Nazarian et al. used time-lapsed micro-computed tomography to visualize failure patterns in trabecular bone cores after failure, using both step-wise and continuous loading protocols.^{91,92} Though not quantitative, these imaging studies provided qualitative information on failure patterns.

Digital volume correlation (DVC), an adaptation of the previously established 2-D method, can be utilized to provide quantitative information on the failure patterns in a region of interest.⁵ DVC quantifies the displacement field throughout the volume of images, yielding experimental data that can validate the results of numerical simulations of vertebral fracture. Liu et al. assessed the accuracy of applying DVC to trabecular bone and found that the precision of DVC depends on the trabecular structure and, of the three methods compared in the study, the maximum likelihood estimation (MLE) was the most accurate and precise.⁷⁸

The MLE method seeks the displacement field $\mathbf{u}(\mathbf{x})$ that minimizes the functional:^{78,104}

$$\pi(\mathbf{u}(\mathbf{x})) = \frac{1}{2} \int_{\Omega} (I_1(\mathbf{x}) - I_2(\mathbf{x} + \mathbf{u}(\mathbf{x})))^2 d\Omega \quad \text{Eq. 1.1}$$

where \mathbf{x} is the position, Ω is the image domain of the region of interest, $d\Omega = dx dy dz$, and I_1 and I_2 are the pre and post deformation images, respectively. This functional is minimized using a Gauss-Newton method, which requires a first derivative and an approximation of the second derivative of the functional $\pi(\mathbf{u}(\mathbf{x}))$ with respect to $\mathbf{u}(\mathbf{x})$.

The first derivative is found using functional derivative, defined as:

$$D_{\mathbf{u}}\pi \cdot \mathbf{w} = \left. \frac{d}{d\varepsilon} \right|_{\varepsilon \rightarrow 0} \pi[\mathbf{u}(\mathbf{x}) + \varepsilon \mathbf{w}(\mathbf{x})] \quad \text{Eq. 1.2}$$

where $D_{\mathbf{u}}\pi$ is the gradient of π with respect to $\mathbf{u}(\mathbf{x})$ and ε is a scalar. The function $\mathbf{w}(\mathbf{x})$ is an arbitrary variation of $\mathbf{u}(\mathbf{x})$ so that $\mathbf{u}(\mathbf{x}) + \varepsilon \mathbf{w}(\mathbf{x})$ satisfies the same boundary conditions as $\mathbf{u}(\mathbf{x})$. Substituting equation (1) into the right hand side of equation (2) and setting the left hand side of equation (2) equal to zero (assuming that a minimum of π exists) yields:

$$\int_{\Omega} \mathbf{w}(\mathbf{x}) \cdot \nabla I_2(\mathbf{x} + \mathbf{u}(\mathbf{x})) (I_1(\mathbf{x}) - I_2(\mathbf{x} + \mathbf{u}(\mathbf{x}))) = 0. \quad \text{Eq. 1.3}$$

Equation (3) is solved iteratively by discretizing the functions $\mathbf{u}(\mathbf{x})$ and its variants. The displacement for each sub-region is represented as:

$$\mathbf{u}(\mathbf{x}) = \sum_{a=1}^A \mathbf{u}^a N^a(\mathbf{x}) \quad \text{Eq. 1.4}$$

where $N^a(\mathbf{x})$ are the linear shape functions at each nodal value a and \mathbf{u}^a is the displacement field at node a .

When employing the MLE method, the displacement estimates may result in erroneous measurements in regions with relatively high noise levels. Assuming that the displacement field $\mathbf{u}(x)$ is smooth, another term that penalizes noise in the measurement can be added to the functional:

$$\pi(\mathbf{u}(x)) = \frac{1}{2} \int_{\Omega} (I_1(x) - I_2(x + \mathbf{u}(x)))^2 d\Omega + \frac{1}{2} \int_{\Omega} \alpha (\nabla \mathbf{u}(x) : \nabla \mathbf{u}(x)) d\Omega \quad \text{Eq. 1.5}$$

where α is an adjustable regularization parameter. Hussein et al. demonstrated that DVC (using the MLE method) could be applied to whole vertebral bodies to examine yield and post-yield deformations under axial compression.⁴⁸

QCT-Based FE Models

FE models, based on quantitative computed tomography (QCT), have shown tremendous promise for accurate, patient-specific predictions of fracture,⁶⁵ but the efficacy of such models is still being investigated compared to traditional BMD measures.¹³¹ Currently, measurements of bone mineral density (BMD) are used to estimate fracture risk, but these values only explain ~60% of the variation in vertebral strength¹⁶ and almost half of patients with vertebral fractures do not exhibit osteoporotic levels of BMD.⁶⁴ BMD measurements do not incorporate factors that may be critical to vertebral strength, such as: intervertebral heterogeneity, vertebral geometry, and the load distributions across adjacent IVDs. QCT-based FE analyses can combine patient-specific geometry and voxel-based material properties with realistic loading conditions to provide clinically relevant predictions of mechanical behavior in the spine.^{11,30,61,76} These models are a common tool to study spine and hip pathologies⁶⁵ and have shown significant

potential for assessing osteoporosis treatments and characterizing vertebral failure mechanisms.^{88,118}

QCT-based FE models can be created with either voxel-based¹⁸ or geometry-based¹¹⁸ techniques. With the voxel-based method (Figure 1.10), the model is defined directly from the QCT image stack and the mesh is generated by assigning elements that occupy a set number of voxels. Material properties for each element can be estimated as an average of the voxel intensities in each element. Generally, voxel-based models have element sizes between 1–5mm in length.^{18,88} For the geometry-based method, a surface is generated from the image stack and the volume enclosed within that surface is meshed. Several techniques exist for assigning material properties for the geometry-based method, such as averaging a fixed number of voxels near the element centroid or using a weighted average of voxels from the element nodes.¹¹⁸ Results have shown that the shell can be accurately modeled by averaging the density with that of nearby trabecular bone, however this analysis was only performed on 2-D cross sections of the vertebral body.¹¹⁴ Accuracy of both QCT-based methods is dependent on the size of the element mesh.

Despite the advancements in QCT-based FE models, the advantage of these models over using traditional BMD to estimate fracture risk is not yet clearly established.^{86,131} No evidence exists to date indicating that FE models give better predictions of fracture risk than BMD measurements. Differences between FE-computed and experimentally measured bone strength can differ by as much as two-fold.¹⁸ Buckley et al. demonstrated that QCT-based FE models do not accurately capture failure behavior in flexion.¹¹ Preliminary results suggest that deformation patterns in axial compression

are not well captured by uniform boundary conditions,⁵¹ and that accurate boundary conditions representing realistic loading conditions may be critical to improving failure prediction in both compression and flexion. Together with accurate material models of the bone and physiologically relevant boundary conditions, QCT-based FE models may provide a clinically relevant technique for accurate, patient-specific prediction of vertebral failure.

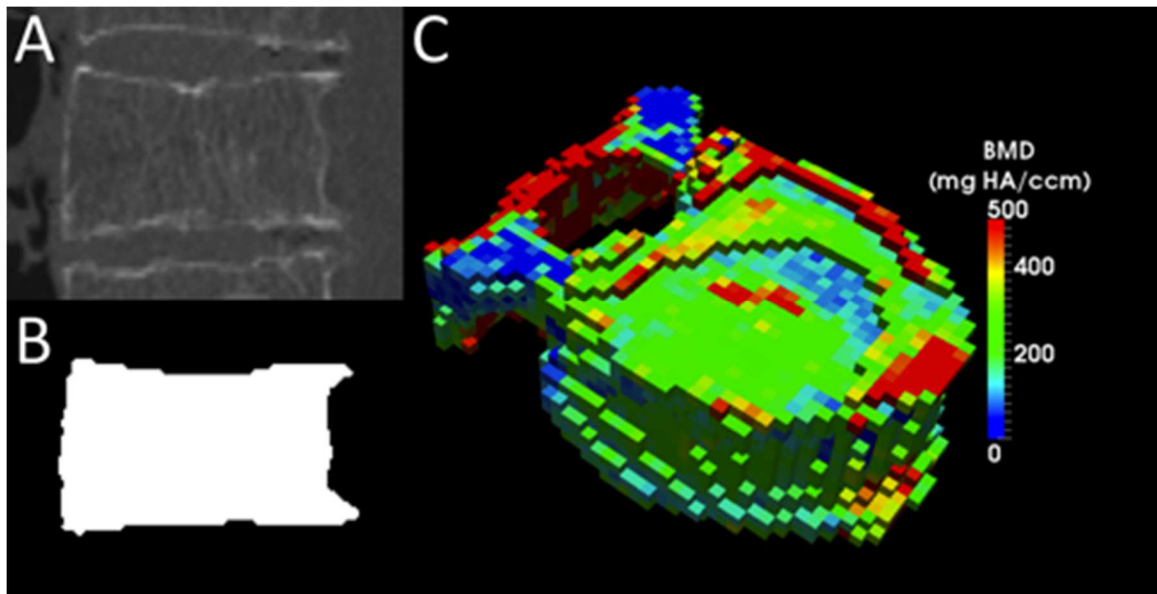


Figure 1.10 (A) Sagittal cut view of QCT image stack. (B) Mask applied to QCT images to isolate vertebra. (C) Voxel-based FE model; BMD values for each element are derived from calibrated QCT images.

CHAPTER TWO

Published in *Journal of Orthopaedic Research*. July, 2014. 32(7): 880–886

**ENDPLATE DEFLECTION IS A DEFINING FEATURE OF VERTEBRAL
FRACTURE AND IS ASSOCIATED WITH PROPERTIES OF THE
UNDERLYING TRABECULAR BONE**

INTRODUCTION

Vertebral fractures affect at least 12–20% of men and women over the age of 50 years,^{41,86,95} and the risk of fracture increases exponentially with age.⁶² These osteoporotic fractures are notable for their high associated morbidity¹⁴ and increased risk of death.¹⁵ Vertebral fracture is a strong predictor of future fractures in the spine, hip, and wrist, even after adjusting for bone mineral density.^{33,77,110} Understanding the mechanisms of vertebral failure will likely have extensive clinical impact with respect to prevention and treatment of fractures in the aging population. Some clinical classifications^{31,58,59} of vertebral fractures and deformities associate large endplate deflection with vertebral failure, indicating that the endplates may play a critical role in mechanical failure of the vertebra.

Biomechanical studies^{39,42,99,109} of vertebral fractures have reported large endplate deflection in conjunction with vertebral failure, but the precise relationship remains poorly defined. Specifically, whether vertebral failure initiates with endplate deflection is not clear at present. Initial endplate injury in motion segments has been observed to coincide with a decrease in stiffness prior to failure,¹³⁷ and excessive endplate bulging and trabecular collapse have been reported to accompany endplate fractures.^{8,39,42} The underlying trabecular bone is widely agreed to provide mechanical support to the endplate: near the endplate, the subchondral trabecular bone, and not the cortical shell,

bears almost the entire load supported by the vertebral body.^{29,43} Regional variations in microstructure, stiffness, and strength have been observed in the underlying trabecular bone,^{45,66,115} and these properties also change with age and the development of osteoporosis.¹²⁰ Such variations in the mechanical behavior of the adjacent bone may affect both the initiation and progression of endplate deflection and, by extension, vertebral failure.

Degeneration of the adjacent intervertebral disc (IVD) may also influence endplate deflection. In axial compression, healthy IVDs maintain approximately uniform pressure across the nucleus pulposus (NP), but in degenerated IVDs, the regions of high pressure shift to the annulus fibrosus (AF).^{2,72} This shift reduces the load borne by the trabecular core,⁴⁴ and may reduce in-plane tensile strains in the central endplate.³² When compared to motion segments with healthy IVDs, those with degenerated IVDs exhibit less spatial variation in stiffness of the neighboring bone.⁶⁷ These studies demonstrate that IVD degeneration alters the loading profile across the endplate and suggest that the underlying trabecular bone may adapt to the new mechanical environment. Thus, IVD health may play a role in the mechanisms of vertebral failure, via effects on vertebral loading and/or trabecular microstructure.

The overall goal of this study was to investigate the relationship between endplate deflection and vertebral failure, with emphasis on associations between endplate deflection and characteristics of the neighboring subchondral bone and IVD. The objectives were: 1) to quantify axial deflection of the endplate using a series of micro-computed tomography (μ CT) images acquired as the vertebra was compressed to failure;

2) to identify associations between endplate deflection and the microstructure of the endplate and subchondral trabecular bone; and 3) to examine the role of IVD health in endplate deflection.

METHODS

Specimen Preparation

Ten functional spine units, each consisting of the L1 vertebra with adjacent IVDs and adjoining endplates of T12 and L2, were dissected from fresh-frozen human spines (age: 61–88 years; 5 male, 5 female; NDRI, Philadelphia, PA) by making transverse cuts just above the inferior endplate of T12 and below the superior endplate of L2. The posterior elements were removed due to the size constraints of the μ CT scanner. The specimens were kept hydrated and, when not in use, wrapped in saline-soaked gauze, sealed in plastic bags, and stored at -20°C .

Mechanical Testing and Imaging

The top and bottom surfaces of the specimens were potted in circular dishes filled with polymethyl methacrylate (PMMA). Each specimen was first imaged with quantitative computed tomography (QCT; GE Lightspeed VCT; GE Healthcare, Milwaukee, WI; $0.32 \times 0.32 \times 0.626$ mm/voxel) and then placed in a custom-built, radiolucent device for mechanical testing (Figure 2.1). After ten cycles of preconditioning to 400N, the specimens were imaged with μ CT (μ CT 80, Scanco Medical, Brüttisellen, Switzerland; $37 \mu\text{m}$ /voxel). The settings for voltage, current and integration time were 70 kVp, 114 mA, and 300 ms, respectively. Scan times ranged 3.5–

4.0 hours. Each specimen was then axially compressed in a stepwise manner (1 mm/step, rate: 0.25 mm/s) by turning the top screw cap to apply the specified displacement.⁴⁸ After a 20-minute relaxation period, the loaded specimen underwent another μ CT scan, with the same scan settings. This stepwise loading was continued to failure, defined as the specimen's ultimate point. The specimen was then unloaded and imaged with μ CT to quantify any post-loading recovery.

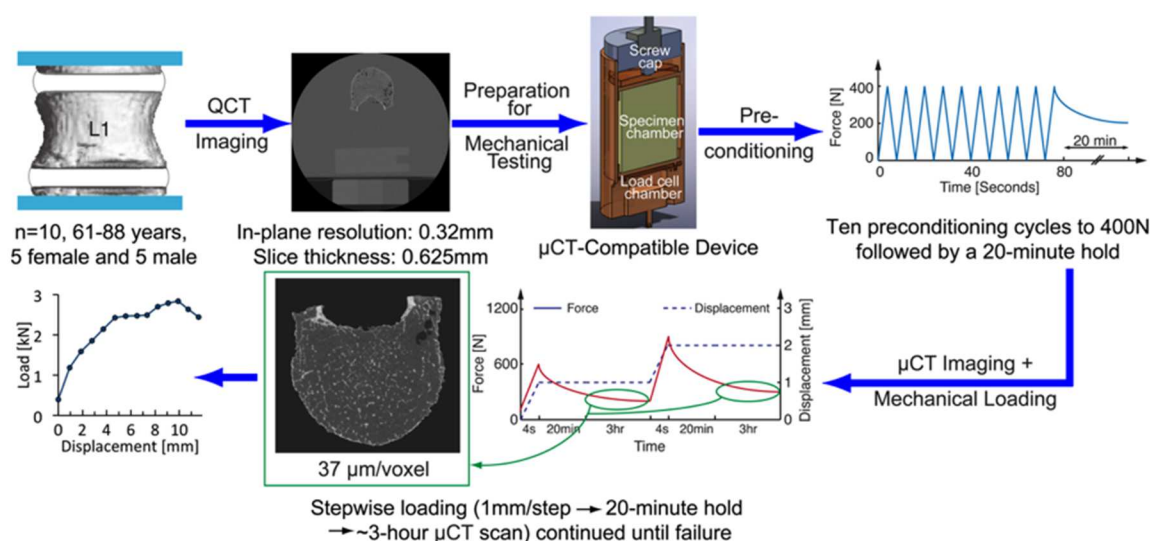


Figure 2.1 Experimental procedure for mechanical testing and imaging

Endplate Deflection

Image registration (IPL; Scanco Medical) was used to align the series of images of the entire vertebral body. The minimum acceptable correlation coefficient between pairs of registered images was set at 0.8; visual inspection was also performed to ensure the images were properly aligned. The surfaces of the calcified endplates of L1 were determined from the aligned images using a semi-automated, custom algorithm in

MATLAB (MathWorks, Inc., Natick, MA). This algorithm used a Gaussian filter (sigma: 1, support: 2) and a global threshold to identify the boundary between calcified and cartilaginous endplate. The threshold, 15% of the maximum grayscale intensity (or 4915 on a 16-bit scale), was selected based on an adaptive, iterative technique (Scanco Medical) for segmentation of bone tissue from marrow. Endplate deflection, defined as the change in axial position between the aligned images, was measured at each pixel on the calcified endplate surface at each load increment (Figure 2.2). The three load increments that immediately followed clear initiation of endplate deflection, defined as deflection exceeding 0.2 mm anywhere on the endplate surface, were identified. This 0.2mm threshold was chosen based on considerations of the measurement precision of endplate deflection.

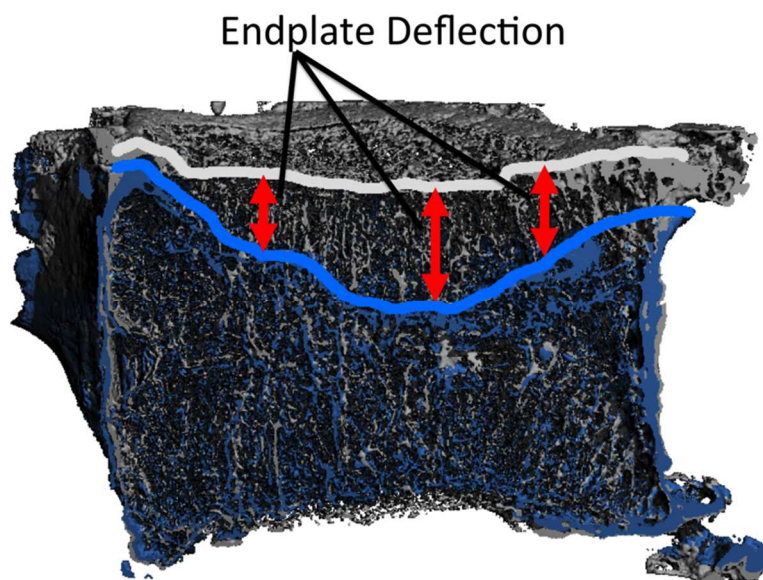


Figure 2.2 Sagittal half-section of vertebra before loading (gray) and after failure (blue): Endplate deflection was defined as the vertical movement of the endplate between registered images.

Subchondral Trabecular Microstructure and Endplate Volume Fraction

A grid of contiguous, 5mm squares was defined just under the superior endplate. Each square defined the sides of a 3-D volume of interest (VOI) that extended from the inferior aspect of the endplate down to a depth of 5 mm (Figure 2.3). Apparent density (ρ_{app}), volume fraction, trabecular separation (Tb.Sp*), trabecular number (Tb.N*), connectivity density (ConnD), degree of anisotropy (DA), structural model index (SMI), and mean deflection were evaluated for each VOI. The same grid of 5mm squares, but with a VOI depth of 2 mm that started from the superior aspect of the endplate,¹⁰⁸ was used for computation of volume fraction, termed as endplate volume fraction (Ep.BV/TV). All analyses used a Gaussian filter (sigma = 0.8; support = 1) and threshold of 4915.

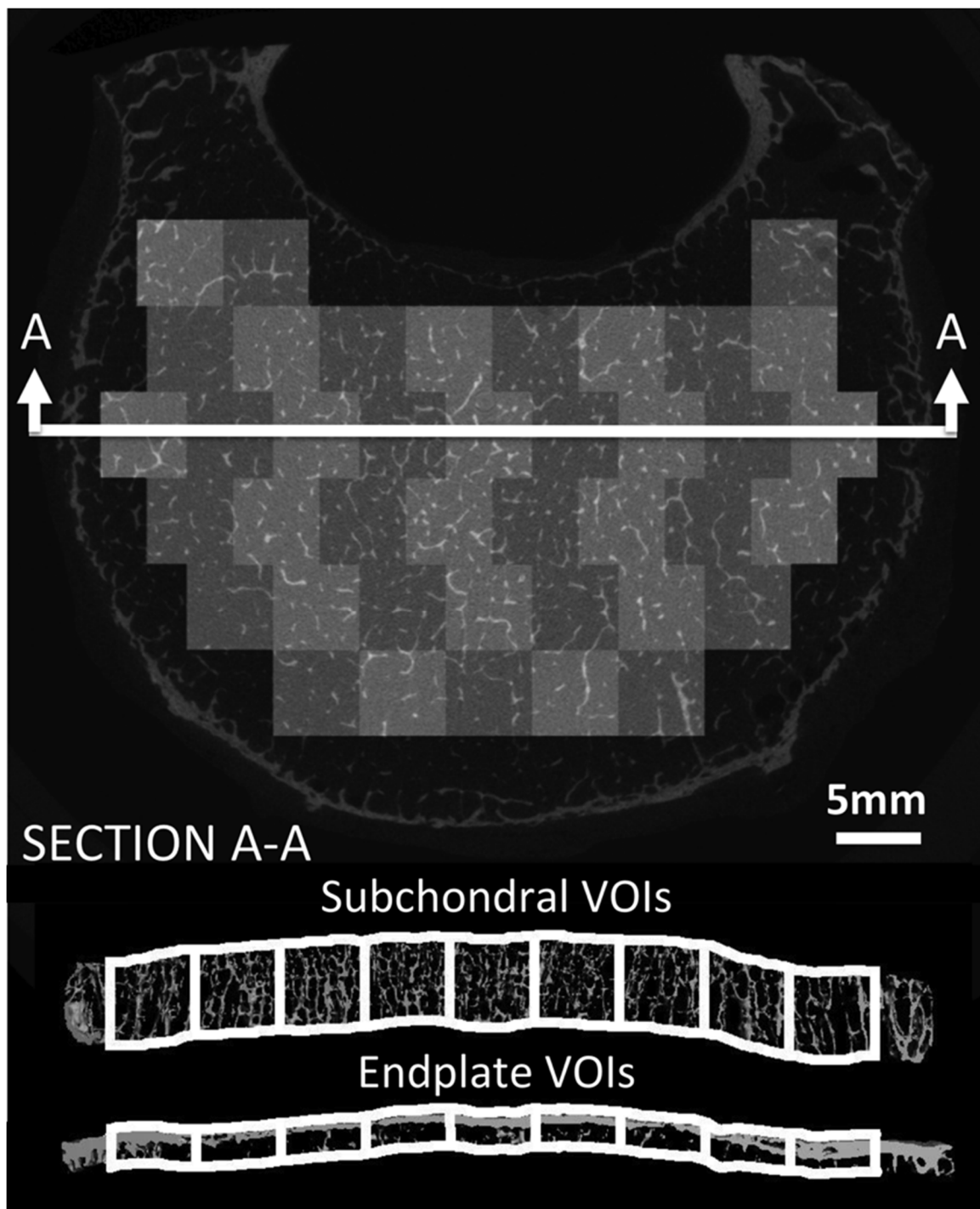


Figure 2.3 Above: Transverse slice of vertebra with an overlay of the VOIs used for quantification of trabecular microstructure and Ep.BV/TV. Below: cross sectional view of the VOIs.

IVD Histology and Grading

Histological assessment of the T12–L1 IVDs was performed to identify the location of the NP and to evaluate the overall health of the disc. Mid-sagittal sections (~7-mm-thick) of T12–L1 IVDs were extracted with the adjacent endplates and subchondral bone, using a low-speed saw (Isomet Low Speed Saw, Buehler, Lake Bluff, IL), and photographed. The extraction was performed after mechanical testing for all but three specimens. After extraction, the specimens were fixed in 10% paraformaldehyde for eight days (solution changed every other day) and decalcified in Morses's Solution³⁸ (10% sodium citrate, 20% formic acid) for 12 days (solution changed daily). The specimens were then progressively dehydrated in ethanol solutions of increasing concentration (up to 70%) and embedded in paraffin. Ten- μ m-thick sections were taken on a microtome (Leica Biosystems, Buffalo Grove, IL), mounted on microscope slides, cleared in Xylene, rehydrated, and stained following the FAST stain protocol.⁷⁵ The IVDs were also graded from photographs taken during extraction¹¹⁹ and from the QCT images, the latter according to the grading scale, "apparent loss of disc integrity" (ALDI)⁴⁹, which ranges from 0 (no/mild degeneration) to 2 (severe degeneration) (Figure 2.4). The ALDI grading scale is based on prior observations that IVD degeneration initiates with dehydration in the nucleus pulposus (NP),¹² which decreases swelling pressure and progresses to a loss of demarcation between the NP and annulus fibrosus (AF).^{6,100,119} The ALDI scale was developed from comparisons of transverse and sagittal QCT images to histological sections, noting that a dark, central region in the QCT images corresponds to a healthy nucleus pulposus (NP). This difference in CT attenuation would

be expected based on the high water content of healthy NP tissue. A loss of discernibility of the presumptive NP and/or the appearance of fissures indicated degenerative changes, with the presence of osteophytes being a secondary indicator. From the QCT images, the boundary of the NP was defined as the dark region in the center of the IVD. With the severely degenerated IVDs (n = 3), the NP boundary was not visible in the QCT images and was instead approximated according to Adams et al.,² who demonstrated that the diameter and location of the central hydrostatic region, labeled the ‘functional nucleus’, varies with age, gender, spine level, and degeneration.² The NP boundary identified in QCT images was consistent with empirical approximations Adams et al. developed for lumbar IVDs along the mid-sagittal line. The subchondral VOIs were identified as underlying either the NP or AF.

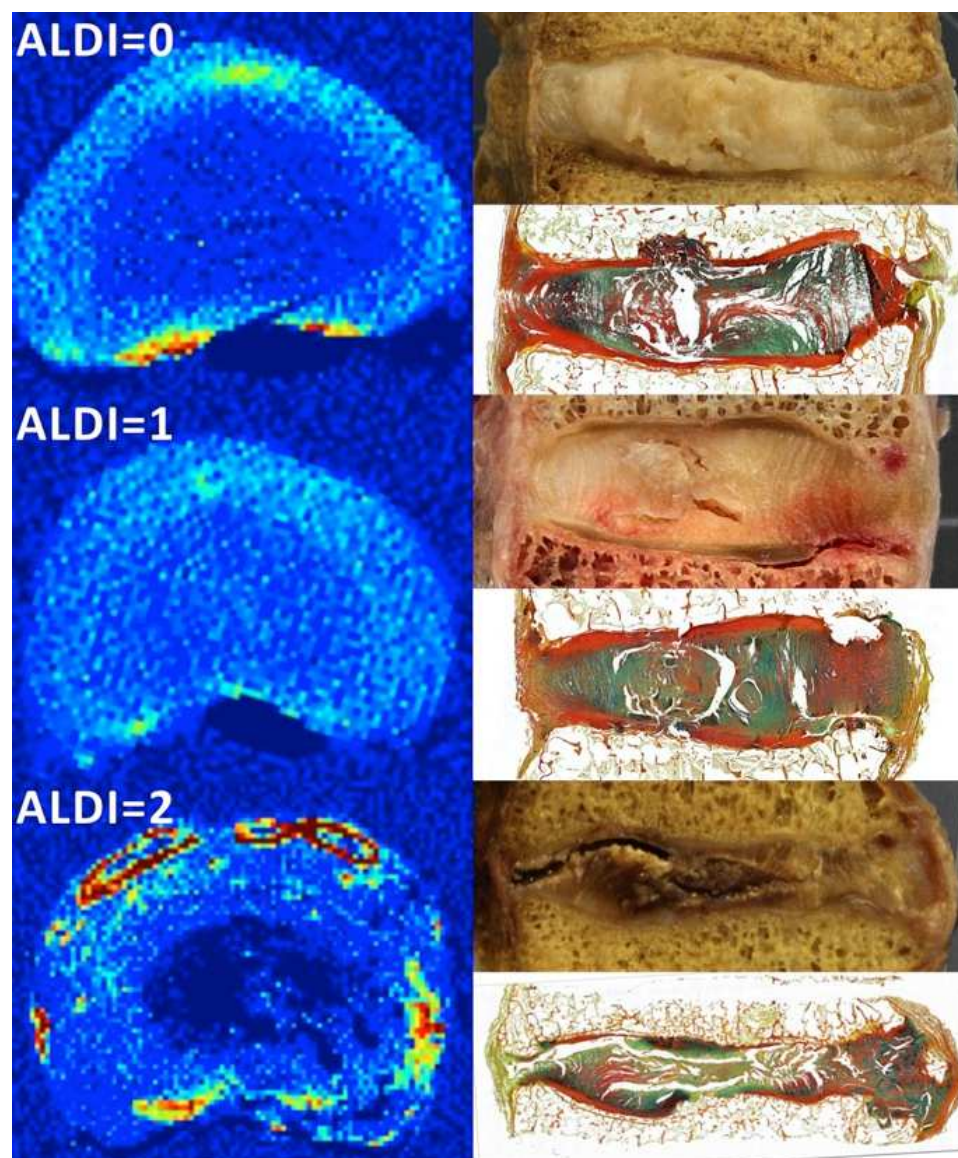


Figure 2.4 ALDI scoring: Shown at the left in each of the three rows is a transverse QCT slice of the IVD (acquired prior to mechanical testing). The ALDI score is shown at the top left. Yellow, orange, and red regions are portions of the endplates and calcification within the IVD; no osteophytes were present in the QCT images of the mid-sections of these three IVDs. Shown at the top and bottom right in each row are a corresponding optical image and histological section (FAST staining⁷⁵), respectively, of a sagittal cross-section (acquired after mechanical testing).

Statistical Analyses

For each parameter of bone microstructure, a repeated-measures analysis of variance (ANOVA) (JMP 9.0, SAS Institute Inc., Cary, NC) was carried out with load increment as the within-subjects factor and the microstructural parameter as a between-subjects factor. An additional factor, the distance of the VOI to the site of initial deflection (“VOI distance”; Figure 2.5), was included in the ANOVA model, to control for the distance when evaluating the association between deflection and microstructure (*i.e.*, to account for the possibility that large deflection would be more likely in regions close to the site of initial deflection). An ANOVA was performed for each load increment individually, as a *post-hoc* test to determine how the association between trabecular microstructure and endplate deflection changed as loading progressed. A paired *t*-test with ALDI score as the grouping variable was used to compare median deflection in the region of endplate adjacent to the NP and AF at the single increment just after the ultimate point. A significance level of 0.05 was used for all statistical analyses.

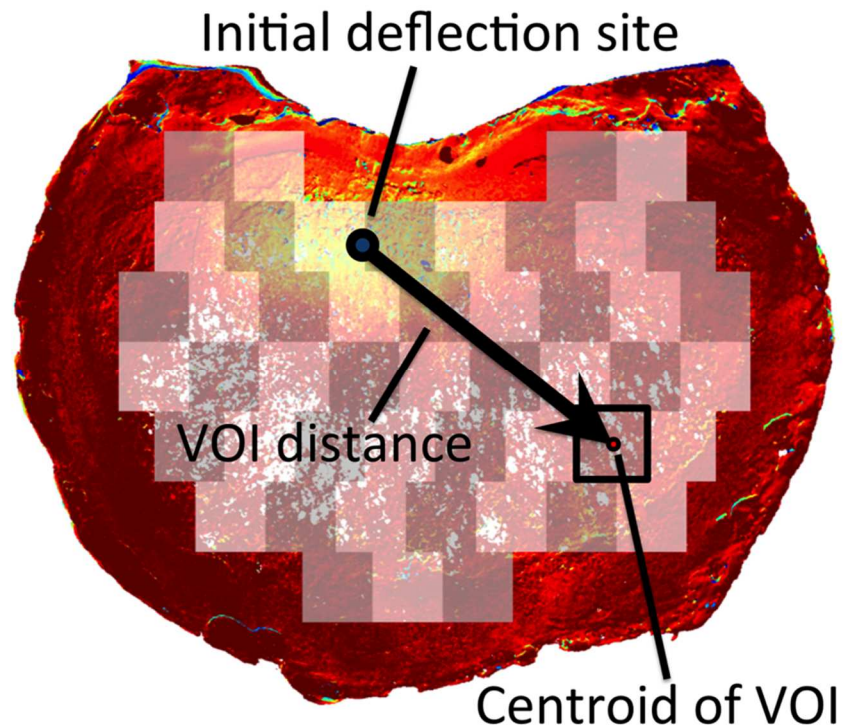


Figure 2.5 VOI distance is defined as the in-plane distance from site of initial deflection to the center of a given VOI used for evaluating trabecular microstructure. Yellow indicates areas of higher endplate deflection, while red indicates areas with little or no deflection.

RESULTS

The superior endplates exhibited a marked increase in deflection that coincided with a drop in the load-displacement curve (Figure 2.6, Table 2.1). The average (\pm standard deviation) maximum deflection of the superior endplate was 0.91 (\pm 0.60) mm prior to the drop in load and then increased 1.22 mm on average (Figure 2.7, Table 2.2). Circumferential cracks appeared in six of the ten superior endplates. Eight failed in the posterior half—and specifically in the ring apophysis for five of these eight—while

two failed in the anterior half. On average, 68% ($\pm 18\%$) of the maximum deflection at the last loading increment remained in the superior endplate after unloading. Deflection of the inferior endplates never exceeded 0.15 mm at any load increment.

Table 2.1 Ultimate force (in N) and the drop in force occurring after the ultimate point (in N and as a percentage of the ultimate force): values presented are mean \pm standard deviation (SD), minimum and maximum for the 10 specimens.

		Mean \pm SD	Min.	Max.
Ultimate Force (N)		2,184 \pm 702	1,138	3,055
Drop in Force Following Ultimate Point	N	196 \pm 92	71	329
	%	11.0 \pm 8.3	2.9	28.9

Table 2.2 Maximum endplate deflection measured before and after the load drop and increase in deflection between these two load increments, expressed in mm and as a percentage of the height of the vertebral body: values presented are mean \pm standard deviation (SD), minimum and maximum for the 10 specimens.

	Mean \pm SD	Min.	Max.
	mm	mm	mm
	(%)	(%)	(%)
Maximum Deflection at Ultimate Point	0.91 \pm 0.60 (3.7 \pm 2.7)	0.37 (1.6)	2.41 (10.7)
Maximum Deflection at After Load Drop	2.13 \pm 0.83 (8.6 \pm 3.7)	1.44 (5.2)	3.92 (17.5)
Increase in Deflection	1.22 \pm 0.44 (4.9 \pm 1.8)	0.63 (2.2)	2.07 (7.6)

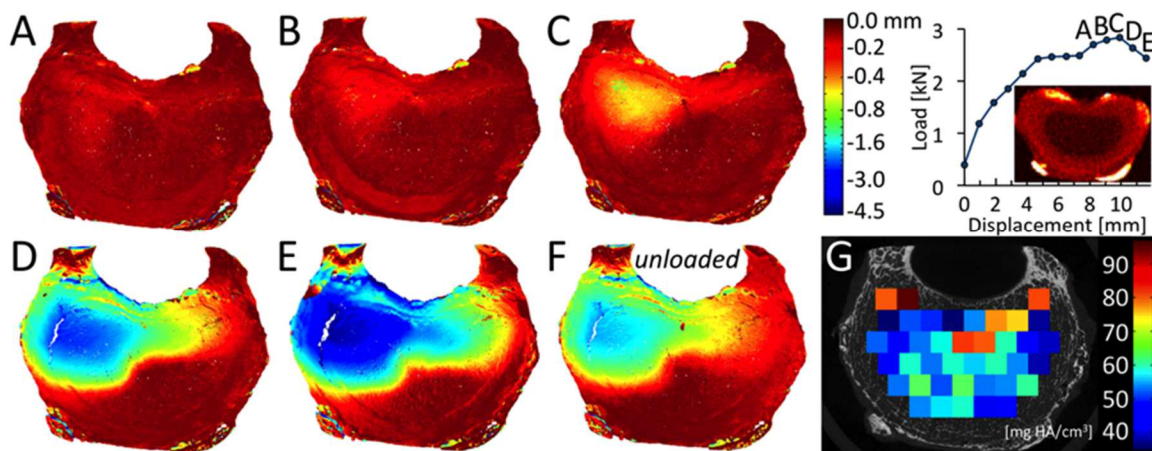


Figure 2.6 (A–E) Axial deflection (negative values indicate downward movement) in the superior endplate for the six loading increments labeled on the load-displacement curve. For this vertebra, increment C is the increment of marked increase in endplate deflection. (F) Endplate deflection after unloading. (G) ρ_{app} for each VOI of subchondral trabecular bone. The deflection colorscale is non-linear, and the red image above the abscissa is the QCT image used for ALDI scoring.

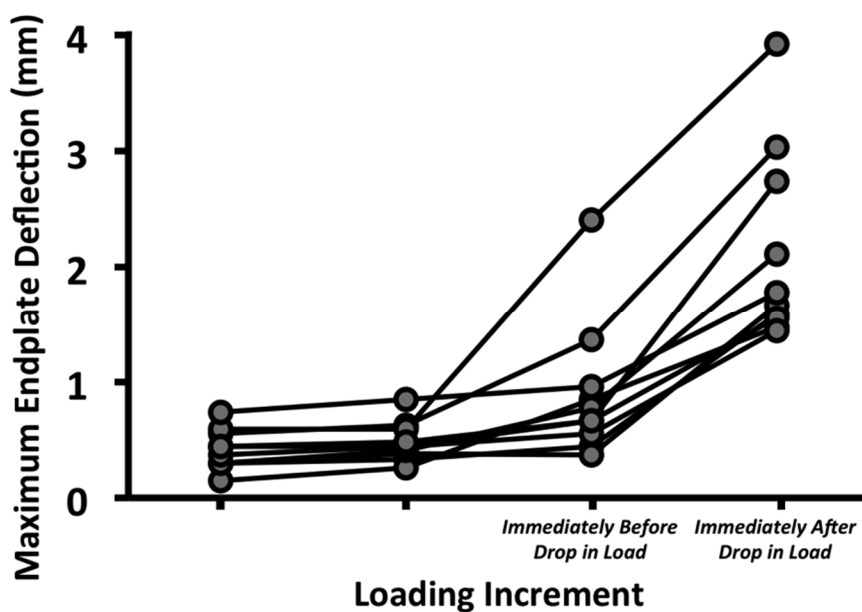


Figure 2.7 Maximum endplate deflection for each specimen at loading increments leading up to and immediately after the drop in the load-displacement curve.

Irrespective of VOI distance and for all load increments, endplate deflection was higher in regions with high Tb.Sp*, SMI (Figure 2.8A), and DA ($p < 0.001$) and lower in regions with high Tb.N*, ConnD, and Ep.BV/TV (Figure 2.8B) ($p < 0.009$), though substantial variations were observed among specimens. An effect of load increment was observed ($p < 0.034$) in that the aforementioned associations tended to weaken as loading progressed. VOIs with higher ρ_{app} experienced smaller deflections ($p = 0.003$) at the first of the three increments; no correlation was found in the other two increments ($p > 0.324$). For the increment corresponding to the large drop in the load-displacement curve, the median endplate deflection in the NP region was higher than that in the AF region (0.46 mm vs. 0.21 mm, $p = 0.035$), irrespective of disc grade ($p = 0.346$).

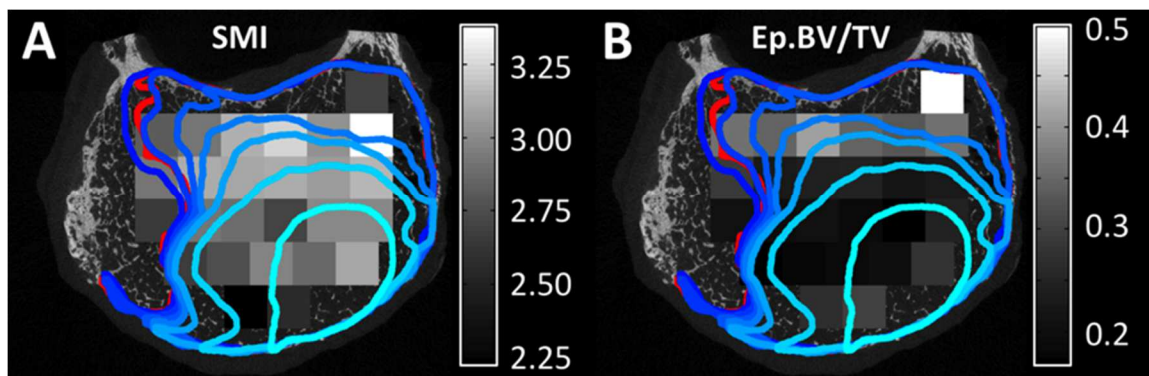


Figure 2.8 Regions of large endplate deflection (outlined in blue and red), defined as >0.5 mm, and (A) distribution of SMI in the VOIs of subchondral bone (grayscale) or (B) distribution of Ep.BV/TV in the VOIs of subchondral endplate (grayscale): The lightest blue outline corresponds to the increment at which endplate deflection clearly initiated. The boundaries at subsequent increments are represented with progressively darker shades of blue. The red outline corresponds to the unloaded scan. SMI values typically range from 1 (plate-like trabeculae) to 3 (rod-like trabeculae) and can include values up to 4 (sphere-like trabeculae).

DISCUSSION

With both clinical classifications^{31,58,59} and biomechanical studies^{39,42,99,109} identifying endplate deflection as a frequent feature of vertebral fractures and deformities, our goal in this study was to examine the relationship between endplate deflection and vertebral failure. Further, to understand the mechanisms underlying this relationship, we investigated associations between endplate deflection and structural properties of the endplate, adjacent bone and IVD. We found that sudden and non-recoverable endplate deflection was a defining feature of biomechanical failure of the vertebra. Although large endplate deflection was initially localized, a marked increase in endplate deflection indicated that the mechanical competence of the vertebra had been severely compromised. Endplate deflection initially propagated preferentially to regions of lower Ep.BV/TV and less robust trabecular microstructure, and these associations with bone microstructure then waned as loading progressed. Immediately after the point of vertebral failure (the ultimate point), deflection was larger in regions adjoining the NP, for all IVD grades. These results connote a biomechanical basis for clinical use of large endplate deflection as a characteristic of vertebral deformities and fracture,^{31,58,59} and they suggest that the failure mechanisms relate to anatomical features of the endplate, neighboring bone, and IVD.

A novel aspect of this study is that it examined both the initiation and propagation of endplate deflection using quantitative and three-dimensional techniques. Deflection was measured across the entire surface with high spatial resolution, allowing for comparison between regional deflection and local microstructure of the endplate and

subchondral trabecular bone. Another strength of this study is that it made direct temporal connections between the observed endplate deflection and the load-carrying capacity of the vertebral body under axial compression.

After the sudden increase in endplate deflection, trabecular collapse was observed primarily in the superior third of the vertebral body. In time-lapsed failure analyses of specimens of trabecular bone, Nazarian et al. reported that failure occurred in a localized band with surrounding portions staying relatively intact.⁹² This failure pattern is similar to the local band of trabecular collapse observed in this study, just underneath the superior endplate, where bone density is low.⁵⁰ These observations further indicate that the subchondral trabecular bone is critically involved in endplate deflection and vertebral failure. The disparity between superior and inferior endplate deflection supports previous findings that superior endplates are more susceptible to failure.^{96,122} The larger endplate deflection underlying the NP vs. AF may reflect regional variations in endplate thickness,¹³⁸ trabecular microstructure, and intradiscal pressure.² The last factor may not be dominant, given that no effect of disc grade was found; however, a larger sample size is required to provide a definitive conclusion.

The limitations of this study primarily relate to experimental procedures. First, the temporal resolution of deflection data was coarse, providing on average only 14 load increments and as few as three increments after initiation of endplate deflection. The number of increments was limited because of long scan times and the perishable nature of the tissue. Ancillary time-course experiments of five L3 vertebrae scanned repeatedly over 72 hours showed no change in attenuation of the bone tissue ($p > 0.08$). In contrast,

marrow attenuation decreased 27% on average over 72 hours in four of the specimens ($p < 0.01$). Thus, the current protocol is sufficient for quantifying bone parameters over several days, but the prospect of increasing the duration must be evaluated with caution. Scan times could be reduced by imaging only the endplates; however, acquiring images of the entire vertebral body aids in image registration. Second, due to size constraints of the μ CT scanner, the posterior elements were removed from the vertebral body prior to testing. The neural arch may act to support the posterior cortical shell, and its absence may have led to some of the posterior (as opposed to anterior) endplate failures observed here. Future studies with thoracic segments or with larger capacity μ CT scanners are needed to examine how the posterior elements affect vertebral load transmission, both in axial compression and anterior bending, a loading condition that may be associated with wedge fractures. Third, static loads differ from the dynamic loading conditions experienced *in vivo*.⁴⁶ Sustained loading exudates fluid from the IVD, causing a drop in NP pressure that shifts the load distribution to the periphery.⁸³ However, the ultimate loads recorded in this study agree with those obtained from continuous loading of lumbar vertebral segments.⁸² Prior studies of trabecular bone have also shown good correlation between mechanical properties obtained with continuous vs. step-wise loading.⁹¹ Fourth, QCT is less sensitive than magnetic resonance imaging¹⁰⁰ for characterizing the internal anatomy of the IVD; however, the QCT-based ALDI scores⁴⁹ agreed well with the assessments based on photographs and histological sections.

In spite of these limitations, the measurements obtained in this study demonstrate that progression of endplate deflection is associated with the microstructure of the

endplate and the adjoining trabecular bone, and the anatomy of the adjacent IVD. Non-recoverable endplate deflection was observed when the mechanical competence of the vertebra had been compromised, while much of the vertebral body remained undeformed. These results indicate that vertebral failure initiates as endplate deflection and that additional study of the mechanisms of endplate deflection may further elucidate the pathogenesis of age-related vertebral fractures.

CHAPTER THREE

DEVELOPMENT OF A POLYURETHANE CALIBRATION LAYER TO FUNCTION AS A MULTI-AXIAL LOAD CELL

INTRODUCTION

Vertebral wedge fractures are the most commonly observed type of clinical vertebral fracture^{26,57,86} and are associated with a combination of compression and bending loads.³⁷ While endplate deflection is a defining feature of vertebral failure under axial compression,⁵⁴ the role of endplate deflection and deformation in the anterior cortex for spine segments tested under anterior flexion remains unclear. Mechanical testing of spine segments in conjunction with micro-computed tomography (μ CT) can be utilized to visualize the progression of vertebral fractures and quantify deflections at both the endplates and anterior cortex as the vertebra is loaded to failure. Spine segments loaded under a combination of compression and bending loads require a multi-axial load cell to accurately describe the loading environment during mechanical testing; however, spatial constraints in the μ CT equipment precluded the use of commercially available multi-axial load cells that would measure the loads and moments experienced by the spine segment under anterior flexion.

To measure the non-uniform distribution of force along the inferior surface of the spine segment, a calibration layer was employed to operate as a multi-axial load cell. The calibration layer—made from polyurethane (McMaster Carr, Elmhurst, IL; diameter: 2 in.; thickness: 0.5 in.; durometer hardness: 40A)—was located underneath the spine segment (Figure 3.1) and deformed as force was applied to the spine segment. The force distribution across the top surface of the calibration layer, and hence across the bottom

surface of the spine segment, could be inferred from measurement of the deformation of the calibration layer and knowledge of the material properties of the polyurethane.

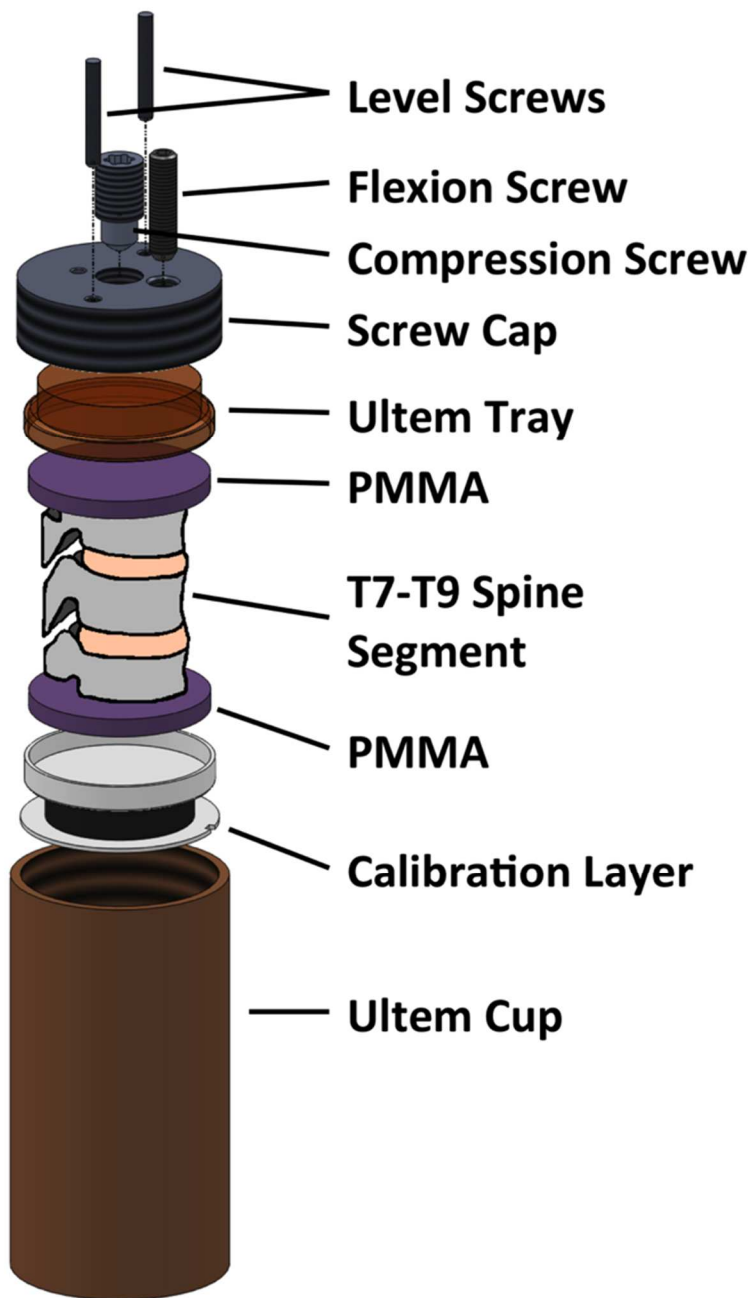


Figure 3.1 Schematic of experimental apparatus for testing spine segments under anterior flexion

ASSEMBLY

The polyurethane was affixed with cyanoacrylate (CA100; 3M, St. Paul, MN) to the top of a thin polyvinyl chloride (PVC) plate and to the bottom of a PVC potting tray that holds the potted spine segment (Figure 3.2). To improve adhesion, the PVC surfaces in contact with the polyurethane were first abraded with coarse sand paper (80 grit; 346U aluminum oxide; 3M, St. Paul, MN) and scored with a scalpel before applying the cyanoacrylate. Affixing the potting tray to the calibration layer with cyanoacrylate glue was deemed essential to prevent lateral slippage during application of the flexion moment and to ensure known, lateral displacements of the polyurethane at the top and bottom boundaries. The glue was required to hold the polyurethane in place to enforce known boundary conditions by preventing any radial expansion of the material at the PVC interface. The circumferential surfaces of the polyurethane and the cyanoacrylate were covered in a layer of petroleum jelly as a protective coating. During mechanical testing of the spine segments, the loading device was filled with a 60:40 mixture of phosphate-buffered saline and 25% ethanol, both to keep the tissues hydrated and to impede their decomposition.

During proof-of-concept testing for the calibration layer, the glue-polyurethane interface was found to remain intact up to 4kN of axial compression without appreciably expanding (Figure 3.3). Further, the protective coating was observed to sufficiently prevent any appreciable dissolution of the cyanoacrylate in the ethanol.

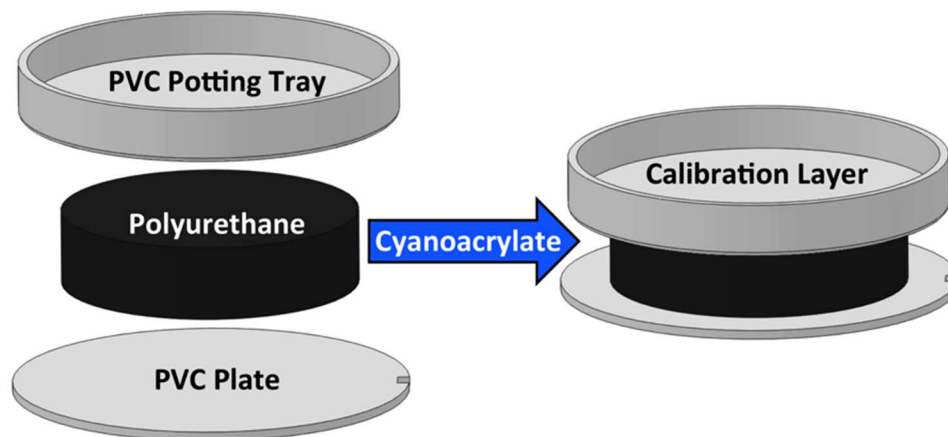


Figure 3.2 Assembly schematic for calibration layer

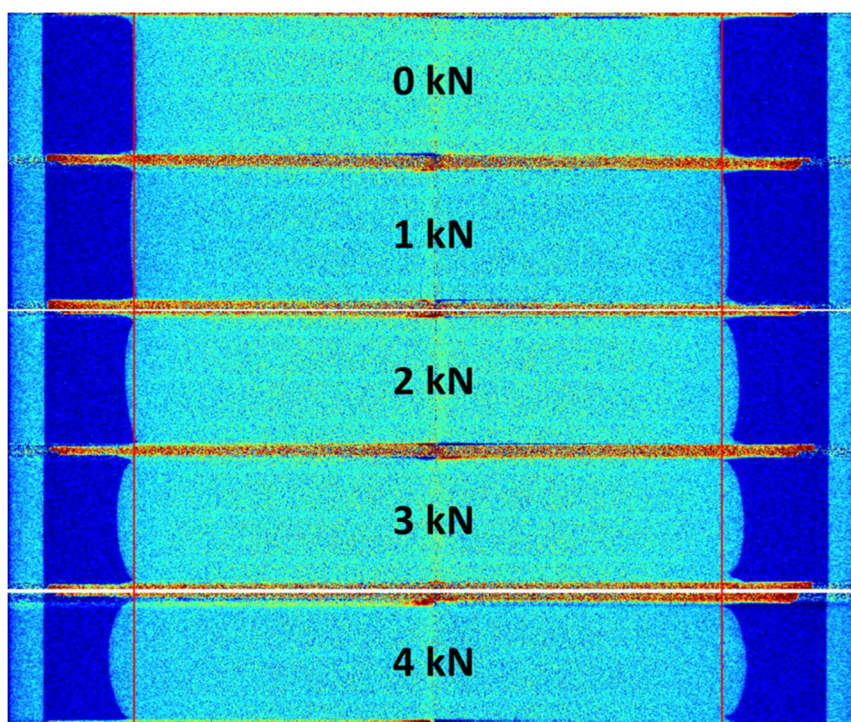


Figure 3.3 Mid-sagittal cross-sections of the calibration layer loaded under 0, 1, 2, 3, and 4 kN with a red line superimposed over the stack of aligned images to mark the unloaded profile of the calibration layer; A color map was applied to the images to improve visualization: red corresponds to the high attenuating PVC plates while the dark blue corresponds to air.

MECHANICAL TESTING AND IMAGE ANALYSIS

Prior to testing, the calibration layer was subjected to eight cycles of preconditioning up to 30% strain. After mechanical testing, the same preconditioning cycles were applied to the calibration layer to confirm that the mechanical behavior of the polyurethane was not altered during the experiment (Figure 3.4). During stepwise mechanical testing of the thoracic spine segment, the calibration layer was scanned at each load increment (μ CT 80, Scanco Medical, Brüttisellen, Switzerland; $37 \mu\text{m}/\text{voxel}$; beam hardening: Al), and the deformation of the polyurethane was measured by tracking displacement of the PVC plate and potting tray using a custom-built, semi-automated algorithm in MATLAB (MathWorks Inc., Natick, MA). This algorithm applied a Gaussian filter (sigma: 2, support: 4) and a global threshold to identify the global position of the PVC surfaces adjacent to the polyurethane. Scanning artifacts (caused by scanning flat surfaces parallel to the beam path) were observed near the center of the calibration layer, so the algorithm applied a mask to select a 10-voxel-thick ring around the outer edge and interpolated through the interior of the PVC surface based on the position of the outer edge (Figure 3.5). For cases where the PVC tray was observed to bow, it was necessary to allow manual assistance to track the interior of the PVC surface. In this case, the algorithm presented axial images of the calibration layer (Figure 3.6) and allowed the user to pick points positioned at the PVC surface. The user was required to pick up to 5 points on each image, depending on the image location in the calibration layer, to obtain a total of 25 points. These manually entered points were used with the position data of the outer edge to interpolate across the entire surface. After interpolation, a mask was applied

to exclude surface data outside the diameter of the polyurethane. The position data for each load step was compared to the unloaded image set to determine the displacements applied to the polyurethane for each load step.

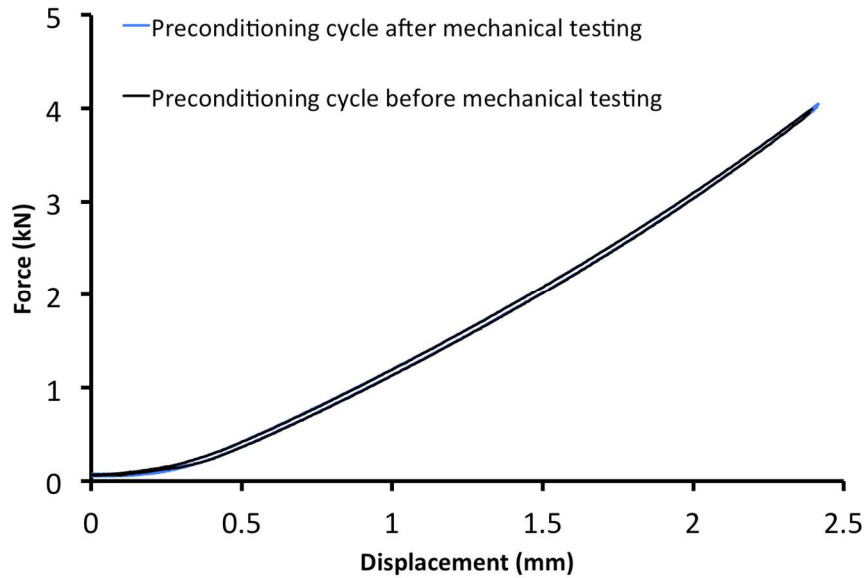


Figure 3.4 Preconditioning cycles for the calibration layer before and after mechanical testing

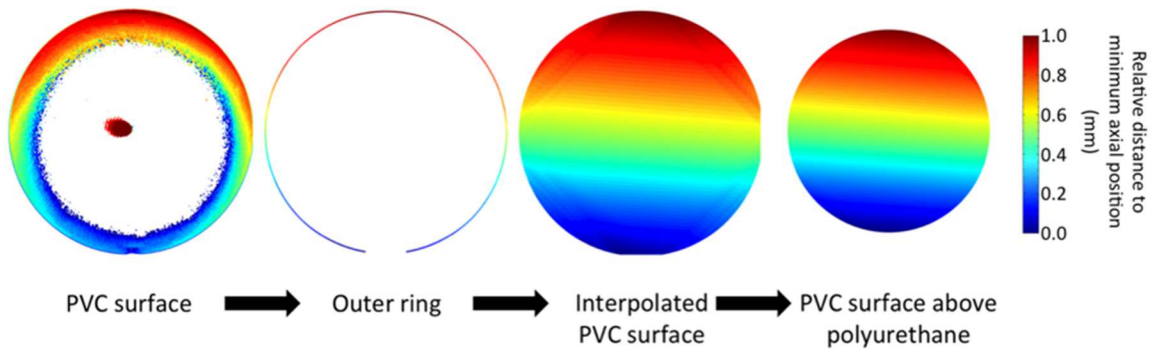


Figure 3.5 Procedure to interpolate PVC surface from original filtered and segmented data; The gap in the outer ring corresponds to a notch cut into the PVC plate to interface with a pin in the loading device that prevented any rotational movement.

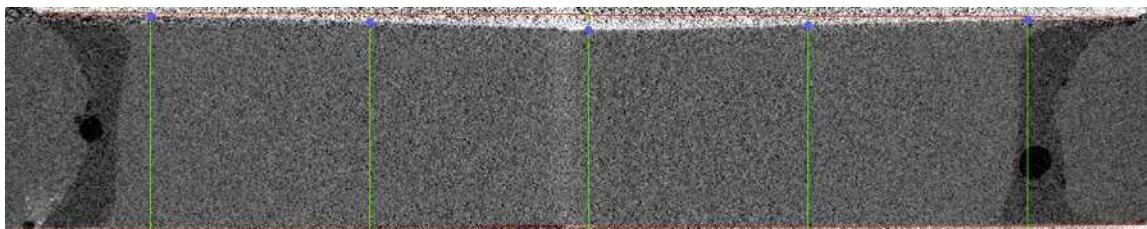


Figure 3.6 Mid-sagittal cross section of the calibration layer featuring bowing in the PVC potting tray. The user identifies where the PVC surface intersects with each green line.

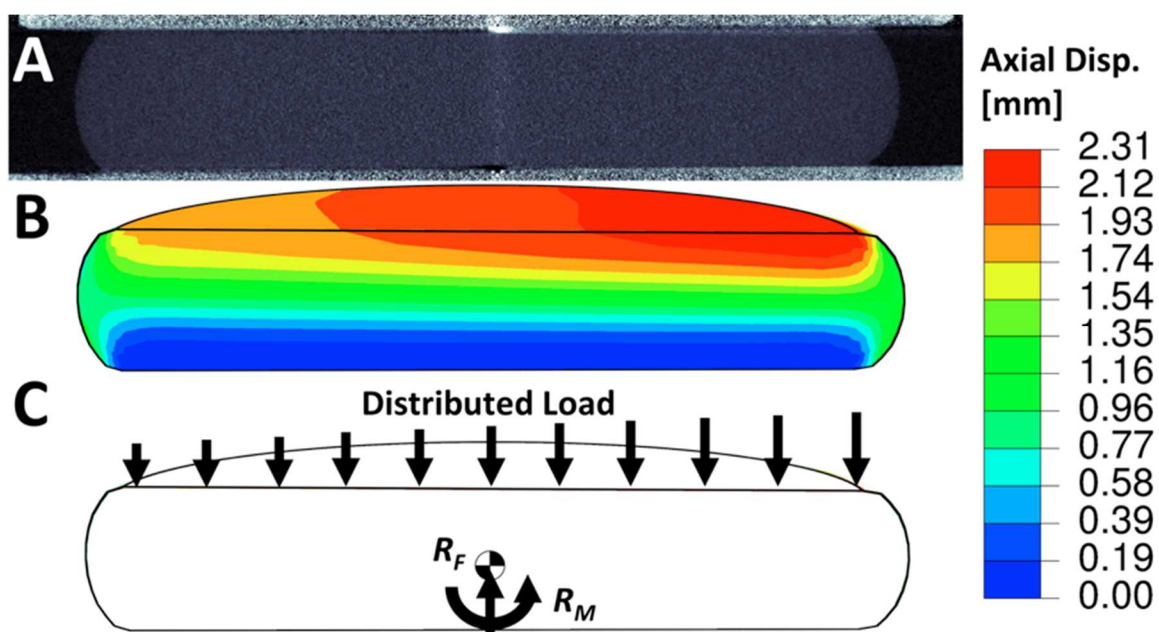


Figure 3.7 A) Mid-sagittal cross section of the calibration layer, imaged using μ CT; B) 3-D view of half-section of FE model, with the color map corresponding to axial displacements obtained at the surfaces by tracking the position of the PVC potting tray and plate, and elsewhere by FE analysis; C) Schematic of distributed load at superior surface of calibration layer and the corresponding reaction force (R_F) and moment (R_M) about the center of mass.

MATERIAL MODELING

The displacements measured across the surface of the calibration layer (Figure 3.7B) were used as the boundary conditions for a nonlinear finite element (FE) model of the layer. The FE mesh consisted of hexahedral elements with a side length of approximately 1 mm. The polyurethane was modeled as a three-element Wiechert model: a spring in parallel with two Maxwell elements. To determine the material behavior of the polyurethane, stress-strain and stress-relaxation curves of the polyurethane were obtained from polyurethane disks that had not been glued to any PVC plates. The top and bottom surfaces of the polyurethane were lubricated to reduce friction at the platen-disk interface as much as possible, and then the polyurethane was compressed up to 40% strain in unconfined compression for four cycles (Figure 3.8; Instron, Norwood, MA). Stepwise stress-relaxation data were obtained for the polyurethane at 1, 2, 3, and 4 kN, with a loading ramp rate of 1 kN per five seconds and a hold period of 600 seconds (Figure 3.9). The experimental curves were imported into MCalibration (Veryst Engineering, Needham, MA) to fit the material constants. The nonlinear elastic response, modeled by a spring in the Wiechert model, was modeled as a neo-Hookean material with strain energy density function (W , MPa) defined as:

$$W = C_1 \left(J^{-\frac{2}{3}} I_1 - 3 \right) + D_1 (J - 1)^2 \quad \text{Eq. 3.1}$$

where J is the determinant of the deformation gradient ($J = \det(\mathbf{F}) = \lambda_1 \lambda_2 \lambda_3$), λ_i are the principal stretch ratios, I_1 is the first invariant of the right Cauchy-Green strain tensor ($I_1 = \text{tr}(\mathbf{C})$), and C_1 and D_1 are material constants. The viscoelastic response,

represented by the two Maxwell elements, was modeled using a power-law strain hardening model, defined as:

$$\dot{\bar{\epsilon}}^{cr} = [A\tilde{q}^n(m+1)\bar{\epsilon}^{cr}]^{\frac{1}{m+1}} \quad \text{Eq. 3.2}$$

where \tilde{q} is the equivalent, deviatoric Kirchhoff stress (in MPa) of the Neo-Hookean material and $\bar{\epsilon}^{cr}$ and $\dot{\bar{\epsilon}}^{cr}$ are the equivalent strain (in mm/mm) and strain rate (in mm/mm·s), respectively. Equivalent strain is defined as a scalar value that describes the strain state in a solid, isotropic material $\bar{\epsilon} = \sqrt{\frac{2}{3}\boldsymbol{\epsilon}^{dev}:\boldsymbol{\epsilon}^{dev}}$, where $\boldsymbol{\epsilon}^{dev} = \boldsymbol{\epsilon} - \frac{1}{3}tr(\boldsymbol{\epsilon})\mathbf{I}$, $\boldsymbol{\epsilon}$ is the infinitesimal strain tensor, and \mathbf{I} is the identity tensor. A , m , and n are material constants. The contribution of each element to the overall response of the material is determined by the stiffness ratio, which is defined as the fraction of the elastic response that will be supported by a given element (the sum of stiffness ratios for all three elements must equal one). The first and second viscoelastic elements were assigned a stiffness ratio of 0.25 and 0.05, respectively, in MCalibration. The stiffness ratio represents the relative contribution of each network to the overall response of the material in the FEA software. When the sum of the stiffness ratios is less than one, the purely elastic network is assigned a stiffness ratio equal to one minus the sum of the stiffness ratios from the viscoelastic elements. In this case, a stiffness ratio of 0.7 was automatically assigned to the purely elastic network.

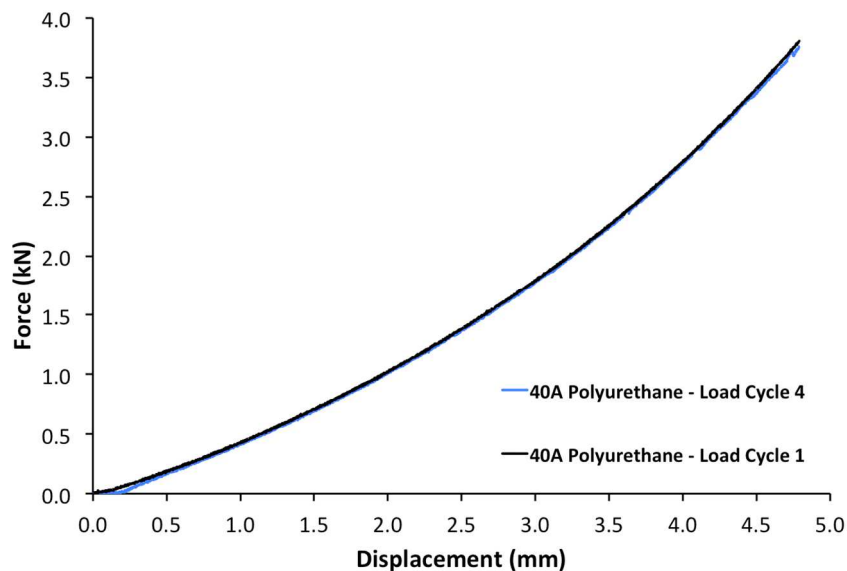


Figure 3.8 Force-displacement curves of 40A polyurethane loaded under axial compression in unconfined compression for four cycles. To reduce friction as much as possible, the polyurethane was lubricated on the surfaces that interfaced with the hydraulic compressor.

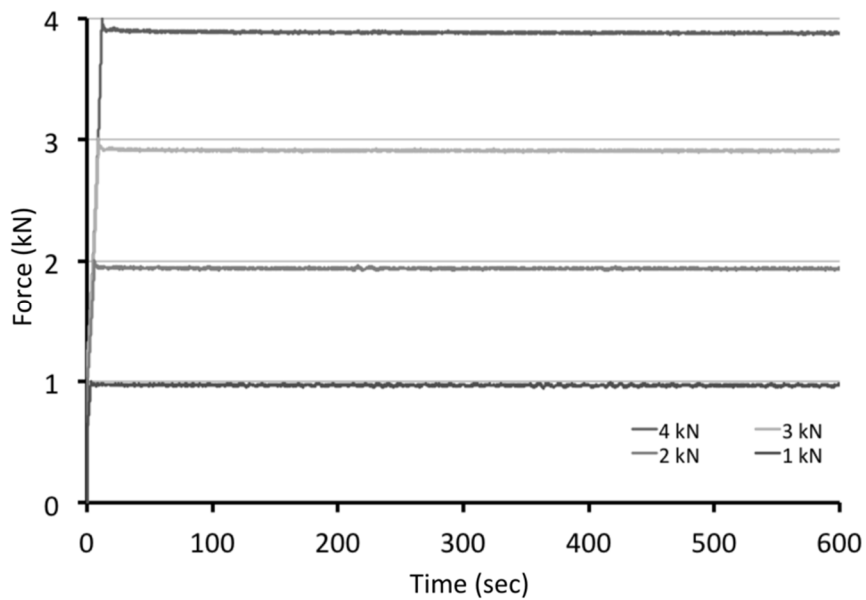


Figure 3.9 Force-relaxation curves for 40A polyurethane loaded under 1, 2, 3, and 4 kN of axial force.

VALIDATION

To validate the material properties obtained from loading polyurethane in unconfined compression, calibration layers (polyurethane glued to PVC plates) were loaded in a stepwise manner up to 4kN and scanned after each load step. The first calibration layer was loaded to 1, 2, 3, and 4kN, while the second was loaded to 0.5, 1.5, 2.5, and 3.5 kN. After applying the load, the calibration layer was held for approximately 2 hours (the scans of the spine segments typically run for 2–2.3 hours) and scanned for 1.5 hours for a combined hold period of 3.5 hours. A load cell was placed in the loading apparatus to record the axial force at each load step. The displacements in the polyurethane were measured using the same techniques described above and the FE model was analyzed with a loading-ramp time of 10 seconds (Abaqus FEA 6.12, Dassault Systèmes, Vélizy-Villacoublay, France). The axial force was determined as the sum of the reaction forces in the z-direction for all nodes on the superior surface of the mesh (Figure 3.7C). Medial-lateral and anterior-posterior shear forces were also obtained. Figure 3.10 compares the experimentally obtained force from the load cell with the FE-computed force. Further, the polyurethane barreling was comparable to the simulated barreling from the FE simulations (Figure 3.7). The anterior bending moment was determined by first obtaining the moment arm from the origin to the location of the FE node, where the origin was defined the center of mass of the polyurethane. The reaction force at each node was multiplied by the sagittal distance from the origin, and the product was summed for all nodes to obtain the anterior bending moment about the origin (Figure 3.7C).

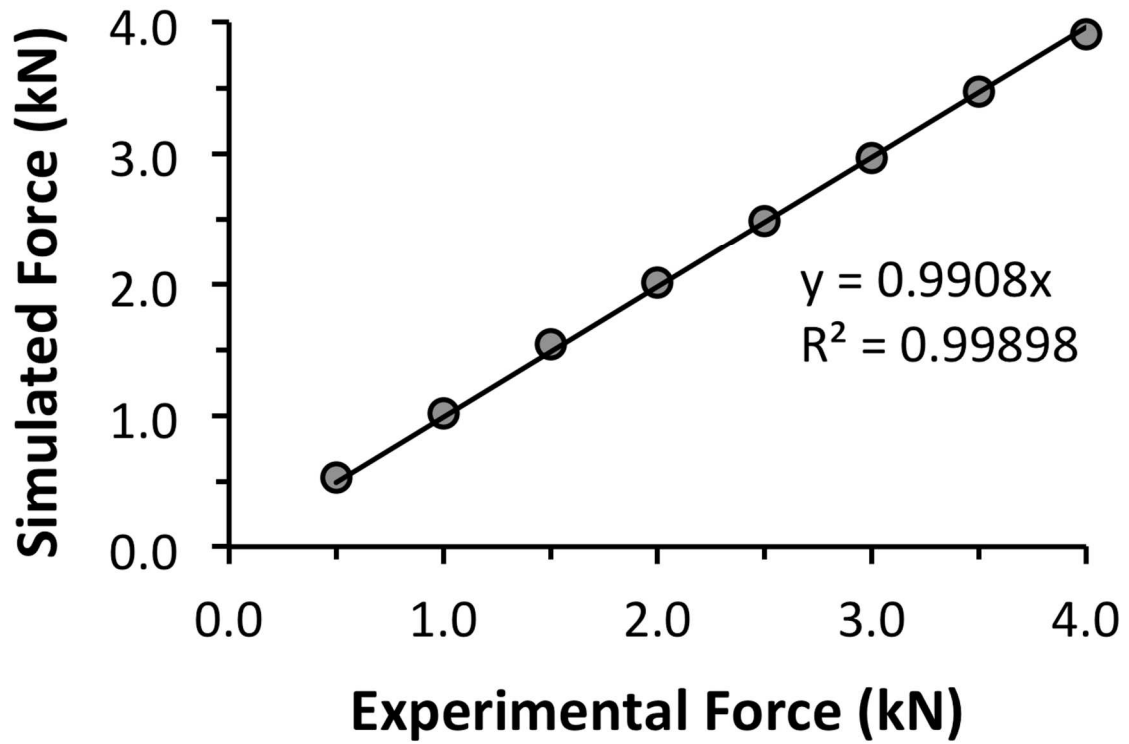


Figure 3.10 Comparison between experimentally measured and simulated force on the polyurethane calibration layer.

CHAPTER FOUR

EXPERIMENTAL MEASUREMENT OF PROGRESSION OF VERTEBRAL FRACTURES

INTRODUCTION

Vertebral fractures represent nearly half of the approximately 1.2 million osteoporotic fractures reported in the United States each year.¹⁰⁵ Identifying patients with incident and prevalent fractures has been a subject of disagreement among clinicians: About one half of vertebral fractures may be asymptomatic, and the natural variation in vertebral shape may confound the classification of mild fractures.²⁶ Wedge fractures are the most commonly observed type of clinical vertebral fracture^{26,57,86} and have been associated with a combination of compression and bending loads,³⁷ while biconcave and compression fractures have been assumed to be associated with only compression loads.^{10,133} Further, a finite element study found that predicted vertebral strength decreased under forward bending when compared to axial compression,⁸¹ suggesting that understanding the failure mechanisms involved in developing wedge and biconcave fractures will likely have a substantial clinical impact regarding fracture prevention and care. Morphological features such as the distribution of trabecular bone underlying the endplate or the health and structure of the adjacent intervertebral disc may predispose the vertebra for a fracture, but few investigations have reported on this topic definitively.^{3,36,132}

The risk for developing a wedge fracture pattern rather than a biconcave or crush fracture may be associated with a combination of degenerative changes in the subchondral trabecular bone and loading patterns that apply larger forces to the anterior

vertebral body. Degenerative changes in the intervertebral disc (IVD) may shield the anterior vertebral body from loads under typical, everyday loading conditions¹⁰¹ and, while bone mineral density (BMD) in the lumbar spine has been shown to decrease over time, the posterior-to-anterior ratio of BMD increases over time.³⁶ A reduction of anterior bone density has been observed for specimens with degenerated IVDs when compared to specimens with healthy IVDs,^{3,132} and could be attributed to IVD degeneration and narrowing of the adjacent IVD space.³ These results suggest that the underlying trabecular bone is adapting to the new mechanical environment and may not be able to support the eccentric loads applied when the spine is in flexion. Biomechanical experiments^{9,101,135} and finite element (FE) simulations^{19,136} have reported increased anterior loading of the endplates under anterior flexion. Under axial compression, local endplate deflection has been identified as an indicator that the mechanical competence of the vertebra has been compromised, even though much of the vertebra remained undeformed.⁵⁴ Studies have observed that initial failure tends to occur at the central endplate for vertebrae tested in compression and under moderate amounts of flexion,³⁷ suggesting that the central endplate may play a vital role in initial failure, regardless of the applied load distribution. While it has been hypothesized that damage then progresses anteriorly within the vertebra under anterior flexion, resulting in a wedge fracture pattern,¹³⁶ the etiology of vertebral fractures—specifically, whether failure initiates at the cortex or at the endplate and then progresses anteriorly—remains largely unknown.

The precise location of initial failure in the vertebral body as the specimen is loaded to failure can be visualized and quantitatively assessed using image-guide failure

analysis. Sites of initial deformation in the vertebra and the progression of deformation into a clinical fracture pattern can be examined by images acquired before and after a fracture has developed. The heterogeneous microstructure of the trabecular bone can be used to track local deformations in whole, intact bones, provided there is a way to image the bone with sufficient resolution. Nazarian et al. used time-lapsed micro-computed tomography (μ CT) to visualize in trabecular bone cores after failure, using both step-wise and continuous loading protocols.^{91,92} These initial studies provided only qualitative measures of deformations and did not quantify the heterogeneous deformation field throughout the trabecular bone. Digital volume correlation (DVC), an adaptation of the previously established 2-D method, has been utilized to provide quantitative information on the failure patterns in a region of interest.^{5,74} Time-lapsed μ CT, in conjunction with DVC, has been used to visualize failure patterns and quantify the displacement field throughout whole bones loaded in axial compression.⁴⁸ DVC quantifies the deformation field throughout a volume of images by applying irregular subregions that conform to the geometry of the vertebra and determining the displacement at the corners of each subregion such that, within each subregion, the intensity of the deformed images best matches the intensity of the original images. With a series of images taken as the vertebra is loaded incrementally to failure, DVC provides a technique with which the onset and progression of a vertebral fracture may be analyzed.

The overall goal of this study was to investigate the development of fracture patterns in thoracic vertebrae loaded in anterior flexion or axial compression. The specific objectives of this study were: 1) to quantify deformations throughout the entire

vertebral body using time-lapsed μ CT and DVC as the vertebra is loaded to failure in anterior flexion or axial compression; 2) to examine the involvement of the endplate and cortex in the initiation of vertebral failure; and 3) to identify associations between endplate deflection and the microstructure of the endplate and subchondral trabecular bone.

METHODS

Specimen Preparation

Twenty-eight T7–T9 spine segments were dissected from fresh-frozen human spines (age: 35–91 years; 8 male, 6 female; NDRI, Philadelphia, PA, and LifeLegacy Foundation, Tucson, AZ) by making transverse cuts through the T6–T7 and T9–T10 IVDs and removing soft tissue of the exposed IVDs (Figure 4.1). A notch was cut into the posterior elements on T7 and T9 such that the posterior elements and zygapophysial joints remained intact but only the T7 and T9 vertebral bodies were embedded in the bone cement to which loading was applied. Thus, no loading was applied to the posterior elements directly by the operator, but no restrictions were placed on load transfer across the T7/T8 and T8/T9 zygapophysial joints. Using a dental tool (Komet USA, Rock Hill, SC), the trabecular bone in the T7 and T9 vertebral bodies was hollowed out and filled with polymethyl methacrylate (PMMA), leaving *at least* 5mm of trabecular bone near the T8 vertebra. This procedure was performed on the vertebrae adjacent to T8 to bias the segment towards failure at T8, while the remaining trabecular bone was left to maintain loading contains as physiologically relevant as possible. The exposed endplates of the T7 and T9 vertebral bodies were potted in circular dishes filled with PMMA. The spine

segment was embedded in cement with the T8 vertebra oriented in the axial direction of the loading device and the T7 and T9 vertebrae were angled according to the natural curvature presented by the spine segment. The spine segments were kept hydrated at all times and, when not in use, wrapped in saline-soaked gauze, sealed in plastic bags, and stored at -20°C .

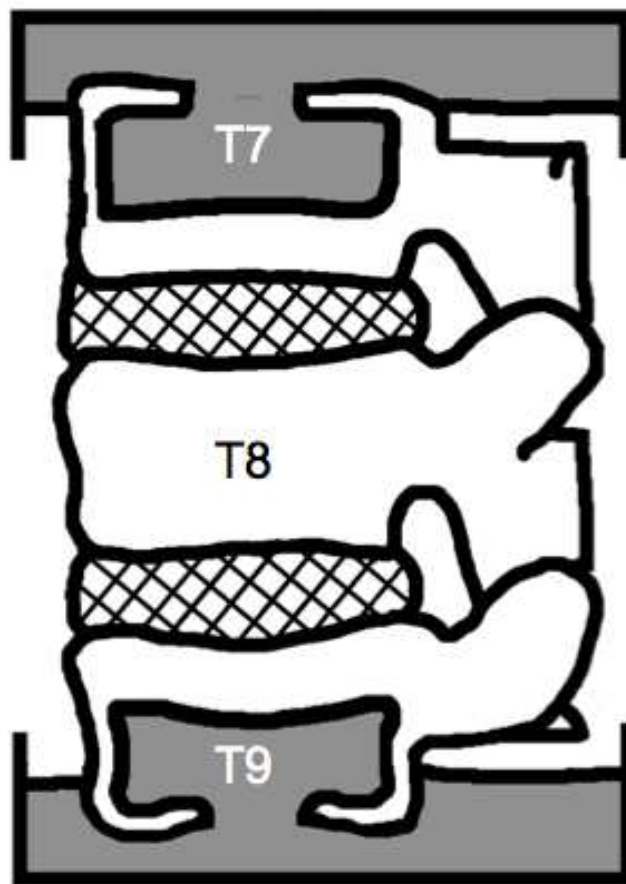


Figure 4.1 Schematic of dissected T7–T9 spines segment for mechanical testing under either axial compression or axial compression with anterior flexion

Mechanical Testing and Imaging

The spine segments were randomly divided into a set for testing under axial compression ($n = 14$) and a set for testing under axial compression with anterior flexion ($n = 14$). Each spine segment was first imaged with quantitative computed tomography (QCT; GE Lightspeed VCT; GE Healthcare, Milwaukee, WI; 0.3125x0.3125x0.625 mm/voxel) and then placed in a custom-built, radiolucent device for mechanical testing (Figure 4.2) that has been filled with 60% saline and 40% of 50-proof ethanol.⁴⁸ After ten cycles of preconditioning to $\sim 300\text{N}$, the spine segments were imaged with μCT (μCT 80; Scanco Medical, Brüttisellen, Switzerland; 37 $\mu\text{m}/\text{voxel}$). The settings for voltage, current and integration time were 70 kVp, 114 mA, and 300 ms, respectively. Each specimen was then loaded in a stepwise manner (0.5mm per step for axial compression; 0.25mm and 0.5° per step for anterior flexion).^{48,54} The compression screw and flexion screw applied the axial compression and angle, respectively, of each step, while the level screws ensured that the angle was only applied in the sagittal plane. After a 20-minute relaxation period, the loaded specimen underwent another μCT scan with the same scan settings. This stepwise loading continued to failure, identified by visible deformation in the T8 vertebral body via lateral scout views. For anterior flexion, the load increment at the “peak of loading” was defined as the load increment immediately before the onset of visible deformation in the T8 vertebra as observed on scout views of the spine segment and later confirmed by measuring endplate deflection. Under axial compression, the axial load was recorded for each load increment using a 22-kN load cell (LLB450, Futek Advanced Sensor Technology, Irvine, CA) inserted into the bottom of the mechanical

testing device. For specimens tested under anterior flexion, the axial force and the anteriorly directed moment experienced by the spine segment were obtained for each load increment using the calibration layer as discussed in Chapter Three. For this study, positive moments indicate an anteriorly directed moment. After failure, the specimen was then unloaded and imaged with μ CT to quantify any post-loading recovery.

A semi-quantitative technique³⁴ was used to assess whether the T8 vertebra had reached the minimum standard for a clinical fracture. Lateral scout views for each load step were obtained and the posterior, central, and anterior height of T8 was measured at each step. Wedge and biconcave fractures were defined as a difference in posterior height to anterior and central height, respectively, of at least 20% of the posterior height (Figure 1.4), while crush fractures were defined as a difference in posterior height of at least 20% between the preloaded and subsequent increments.

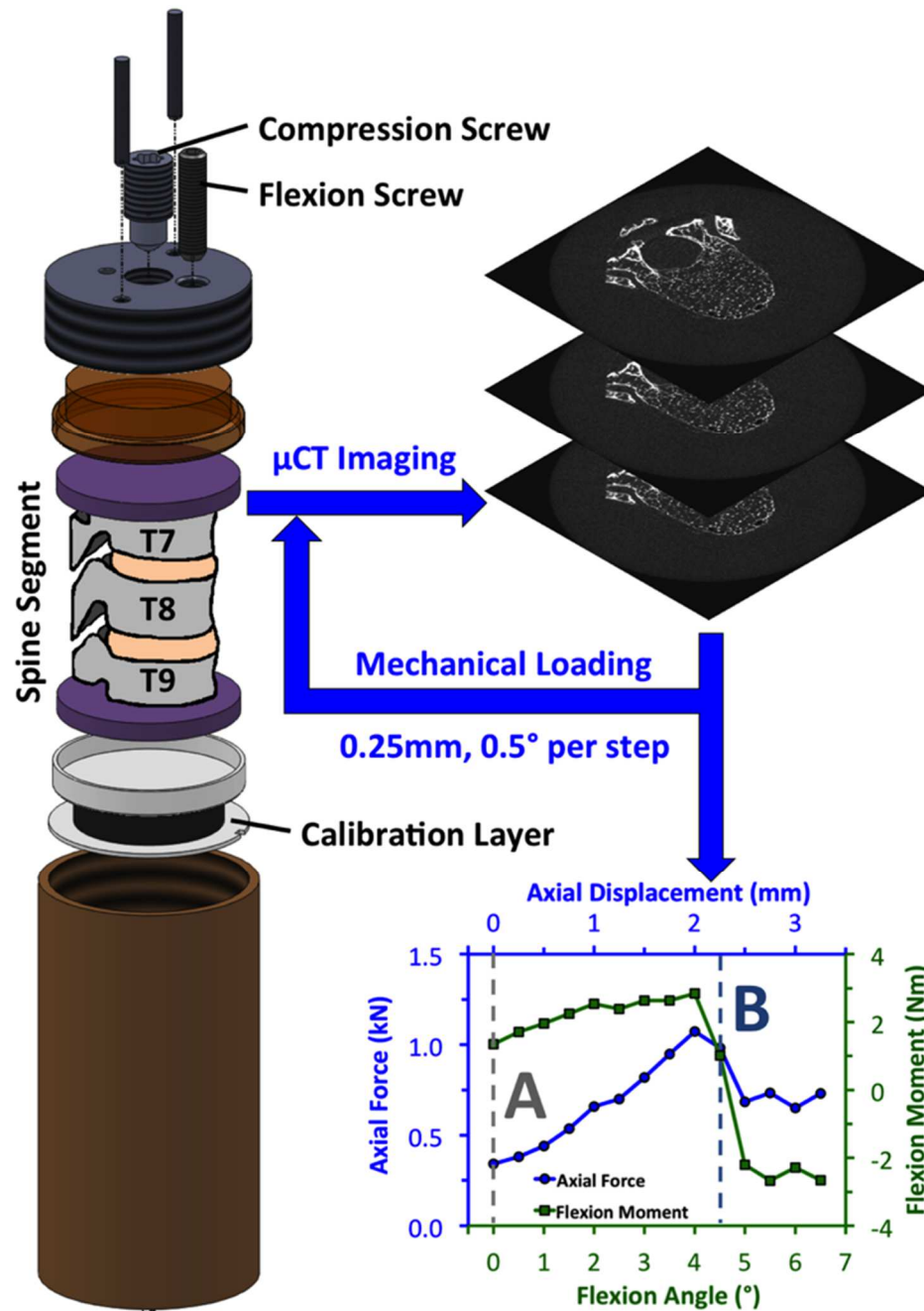


Figure 4.2 Schematic of experimental apparatus for testing spine segments under anterior flexion; The compression screw and flexion screw applied the axial compression and angle, respectively, of each step, while the level screws ensured that the angle was only applied in the sagittal plane.

Endplate Deflection

The surfaces of the calcified endplates of T8 were determined from the aligned images using a semi-automated, custom algorithm in MATLAB (MathWorks, Inc., Natick, MA).⁵⁴ This algorithm used a Gaussian filter (sigma: 1, support: 2) and a global threshold to identify the boundary between calcified and cartilaginous endplate. The threshold, 15% of the maximum grayscale intensity (or 4915 on a 16-bit scale), was selected based on an adaptive, iterative technique (Scanco Medical) for segmentation of bone tissue from marrow. Endplate deflection, defined as the change in axial position between the aligned images, was measured at each pixel on the calcified endplate surface at each load increment (Figure 2.2). The four load increments that immediately followed the peak of loading were identified.

Digital Volume Correlation

The methods for using DVC with time-lapsed μ CT images of human vertebrae were reported previously.⁴⁸ Briefly, image registration (IPL; Scanco Medical) was used to align the series of images of the T8 vertebral body; visual inspection was also performed to ensure the images were properly aligned. A minimum acceptable correlation coefficient between pairs of registered images was set at 0.8; visual inspection of image sets was also performed to ensure the image sets were properly aligned. An irregular mesh that conforms to the geometry of the vertebral body was generated using hexahedral elements with ~ 1.9 mm side lengths (Figure 4.3).

Maximum Likelihood Estimation is an iterative process used to find the displacements at the nodes of each subregion such that the subregions best match the

intensities between the two image sets. Displacements at the nodes were determined by finding the displacement field $\mathbf{u}(x)$ that minimized the functional π :^{78,104}

$$\pi(\mathbf{u}(x)) = \frac{1}{2} \int_{\Omega} (I_1(x) - I_2(x + \mathbf{u}(x)))^2 d\Omega + \frac{1}{2} \int_{\Omega} \alpha (\nabla \mathbf{u}(x) : \nabla \mathbf{u}(x)) d\Omega \quad \text{Eq. 4.1}$$

where I_1 and I_2 are image intensities for the two image sets, Ω is the image domain, and α is a scalar regularization parameter that punishes large displacement gradients. To find the optimal value of α , an artificial displacement was applied to a set of images and the value of α that yielded the most accurate displacement field was identified. All calculations using the MLE method were performed on a supercomputing system (2 eight-core 2.6 GHz, Intel Xeon E5-2670 processors with 256 GB shared RAM) until it converged to an acceptable solution and output displacements at each node. DVC analyses were performed for each load increment up to and including the first increment after the peak of loading. Up to the peak of loading, the displacements obtained from the previous increment were used as the initial guess for the displacement field at the next increment. For the increment immediately after the peak of loading, the experimentally measured deflections at the endplates were used as an initial guess for DVC analyses.

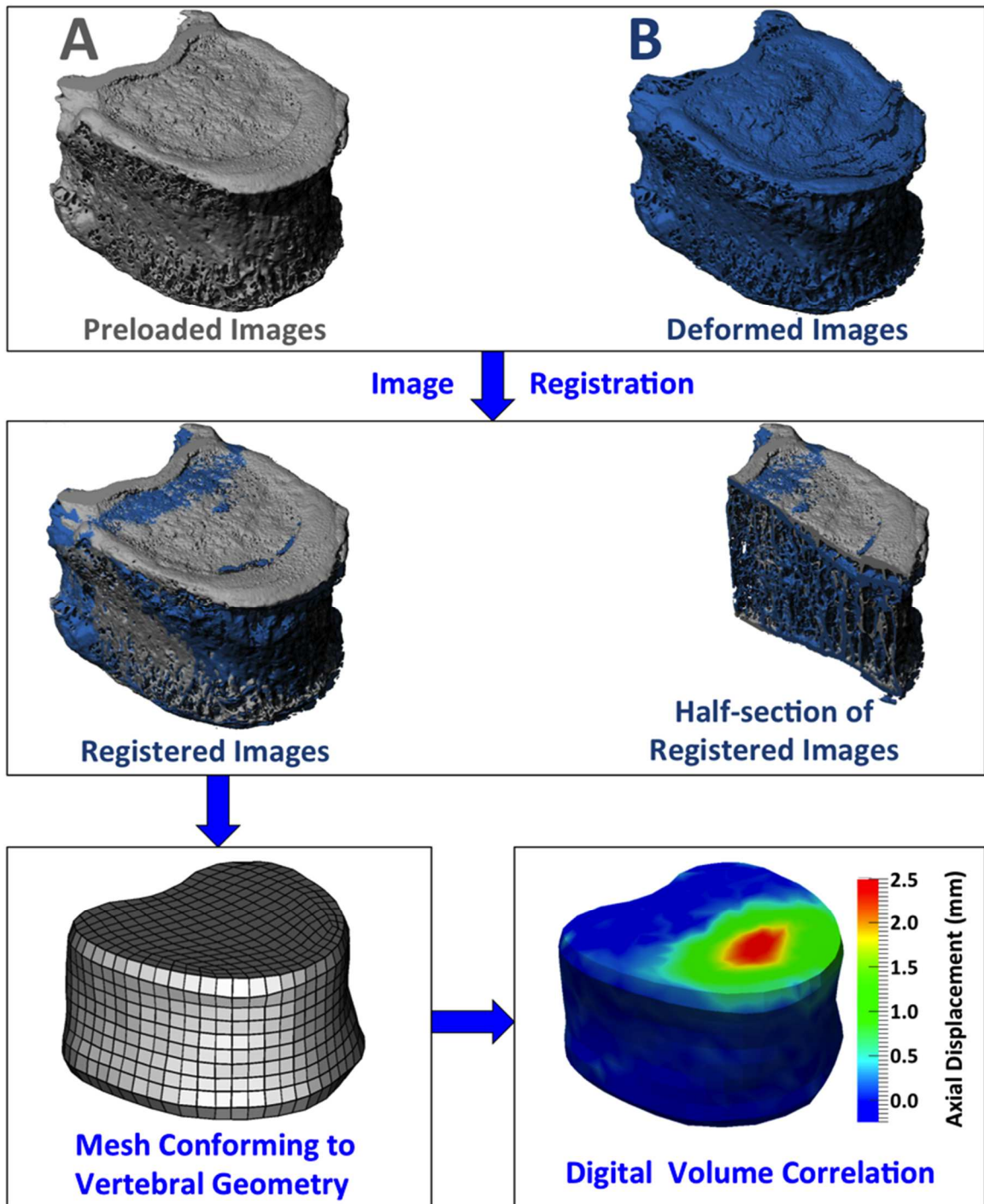


Figure 4.3 Schematic for generating the 3-D, irregularly shaped mesh that was applied to aligned images for digital volume correlation.

Subchondral Trabecular Microstructure and Endplate Volume Fraction

A grid of contiguous, 5mm squares was defined just under the superior endplate. Each square defined the sides of a 3-D volume of interest (VOI) that extended from the inferior aspect of the endplate down to a depth of 5 mm (Figure 2.3). Apparent density (ρ_{app}), volume fraction (BV/TV), trabecular separation (Tb.Sp*), trabecular number (Tb.N*), connectivity density (ConnD), degree of anisotropy (DA), structural model index (SMI), and mean deflection were evaluated for each VOI. The same grid of 5mm squares, but with a VOI depth of 2 mm that started from the superior aspect of the endplate,¹⁰⁸ was used for computation of volume fraction, termed as endplate volume fraction (Ep.BV/TV). All analyses used a Gaussian filter (sigma = 0.8; support = 1) and threshold of 4915.

Statistical Analyses

For each parameter of bone microstructure, a repeated-measures analysis of variance (ANOVA) (JMP 11.0, SAS Institute Inc., Cary, NC) was carried out with load increment as the within-subjects factor and the microstructural parameter as a between-subjects factor. An additional factor, the distance of the VOI to the site of initial deflection (“VOI distance”; Figure 2.5), was included in the ANOVA model, to control for the distance when evaluating the association between deflection and microstructure (*i.e.* to account for the possibility that large deflection would be more likely in regions close to the site of initial deflection). An ANOVA was performed for each load increment individually, as a *post-hoc* test to determine how the association between trabecular microstructure and endplate deflection changed as loading progressed. Contingency

analyses were performed to determine whether ALDI score was associated with the region of initial endplate deflection and pattern of the load-displacement and moment-angle curves. A significance level of 0.05 was used for all statistical analyses.

RESULTS

Anterior Flexion

Immediately after the peak of loading, the superior T8 endplate began to deflect at the anterior central region for eight specimens (Figure 4.4), and at the anterior ring apophysis for six specimens (Figure 4.5). Initial deflection in the anterior central endplate was observed more frequently in specimens with lower ALDI score (healthier IVD): six of eight specimens with initial deflection at the anterior central endplate featured an ALDI score of 0, while the remaining two of eight specimens had an ALDI score of 2. By contrast, an ALDI score of 0, 1, and 2 was each observed for two of the six specimens with initial deflection at the anterior ring apophysis. However, a contingency analysis determined that this pattern was not significant ($p > 0.10$). At the peak of loading, forces of $1,255 \pm 556$ N (mean \pm standard deviation) and moments of 6.77 ± 7.13 Nm (mean \pm standard deviation) were observed (Table 4.1). After the peak of loading, large increases in deflection of the superior endplate (maximum deflection ranged from 0.37–2.78 mm) were observed (Table 4.2) and corresponded to a decline in axial load in nine of 14 specimens (Table 4.1). After the peak of loading, a decrease in anteriorly directed moment of 2.11 ± 1.86 Nm (mean \pm standard deviation) was observed for all specimens and corresponded to a 0.98 ± 0.50 mm (mean \pm standard deviation) increase in deflection of the superior endplate, causing the load to shift further towards the posterior half of the

vertebral body. The force-displacement and moment-angle curves for each specimen could be grouped into the following cases (Figure 4.6): (1) six specimens exhibited maximum positive moment and axial force at the peak of loading, (2) two specimens exhibited maximum positive moment but not maximum axial force at the peak of loading and experienced an increase in axial force immediately after the peak of loading, (3) two specimens exhibited maximum axial force but not maximum positive moment at the peak of loading and experienced a decrease in both positive moment and axial force immediately after the peak of loading, and (4) four specimens exhibited neither the maximum positive moment nor the maximum axial force at the peak of loading and experienced a decrease in anterior moment and an increase in the axial force immediately after the peak of loading. Using contingency analysis, no apparent pattern was observed between IVD health and the four loading cases ($p > 0.45$): Case 1 featured two, one, and three specimen(s) with ALDI score of 0, 1, and 2, respectively; Case 2 featured two specimens with ALDI score of 0; Case 3 featured a specimen with ALDI score of 0 and a specimen with ALDI score of 1; and Case 4 featured two, one and one specimen(s) with ALDI score of 0, 1, and 2, respectively.

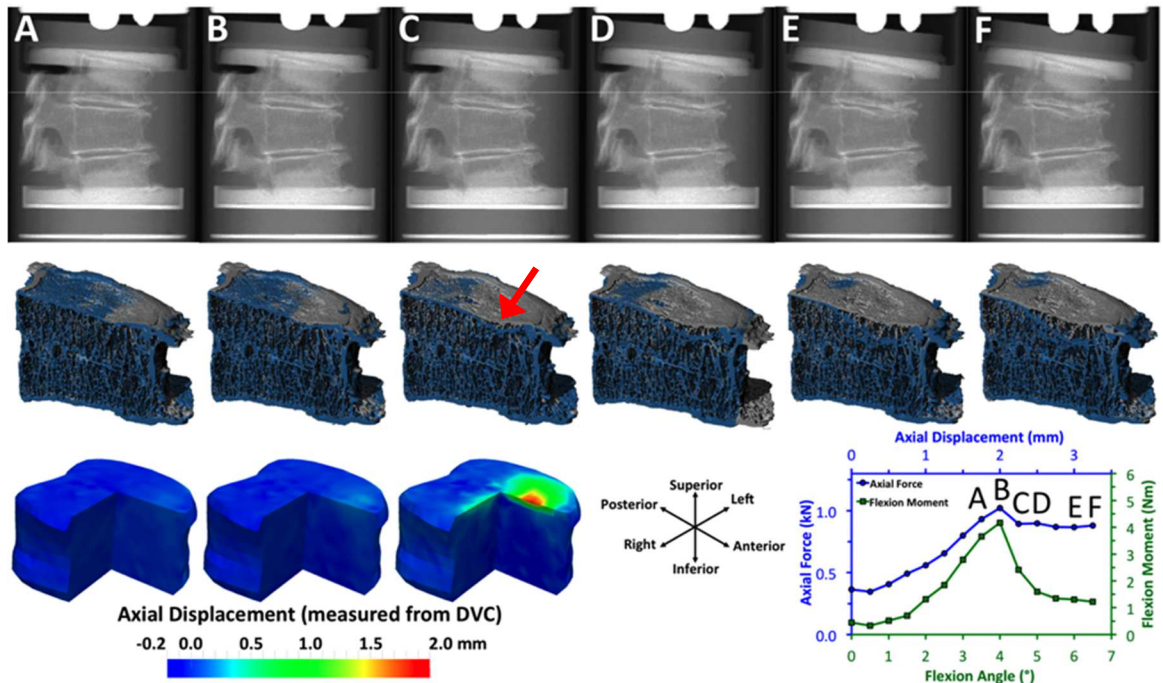


Figure 4.4 For anterior flexion: (Top) Lateral radiographic views (created from μ CT); (Middle) Sagittal half-section of vertebra before loading (gray) and at load increment (blue) noted on the load-displacement and moment-angle curve; (Bottom) For increments A–C, three-quarter section views of experimental displacement field in axial direction; positive values indicate downward displacement. The arrow indicates the site of initial deflection.

Table 4.1 Anterior flexion: Force (in N) and Moment (in Nm) at the peak of loading and the drop in force (in N and as a percentage of the ultimate force) and moment (in Nm and as a percentage of the ultimate moment) occurring after the peak of loading: values presented are mean \pm standard deviation (SD), minimum and maximum for the 14 specimens.

		Mean \pm SD	Min.	Max.
Force at Peak of Loading (N)		1,225 \pm 556	224	2,322
Moment at Peak of Loading (Nm)		6.77 \pm 7.13	0.50	28.81
Force Drop Following Peak of Loading	N	109 \pm 173	-34	583
	%	11.0 \pm 17.4	-3.0	58.3
Moment Drop Following Peak of Loading	Nm	2.11 \pm 1.86	0.39	8.08
	%	65.8 \pm 79.8	5.2	255.0

Table 4.2 Anterior flexion: Maximum endplate deflection measured at and immediately after the peak of loading and increase in deflection between these two load increments, expressed in mm and as a percentage of the height of the vertebral body: values presented are mean \pm standard deviation (SD), minimum and maximum for the 14 specimens.

	Mean \pm SD	Min.	Max.
	(mm)	(mm)	(mm)
	(%)	(%)	(%)
Maximum Deflection at Peak of Loading	0.38 \pm 0.25 (1.9 \pm 1.3)	0.19 (0.9)	1.00 (5.5)
Maximum Deflection Immediately After Peak of Loading	1.36 \pm 0.66 (6.9 \pm 3.5)	0.37 (1.8)	2.78 (15.2)
Increase in Deflection	0.98 \pm 0.50 (5.0 \pm 2.6)	0.15 (0.7)	1.78 (9.8)

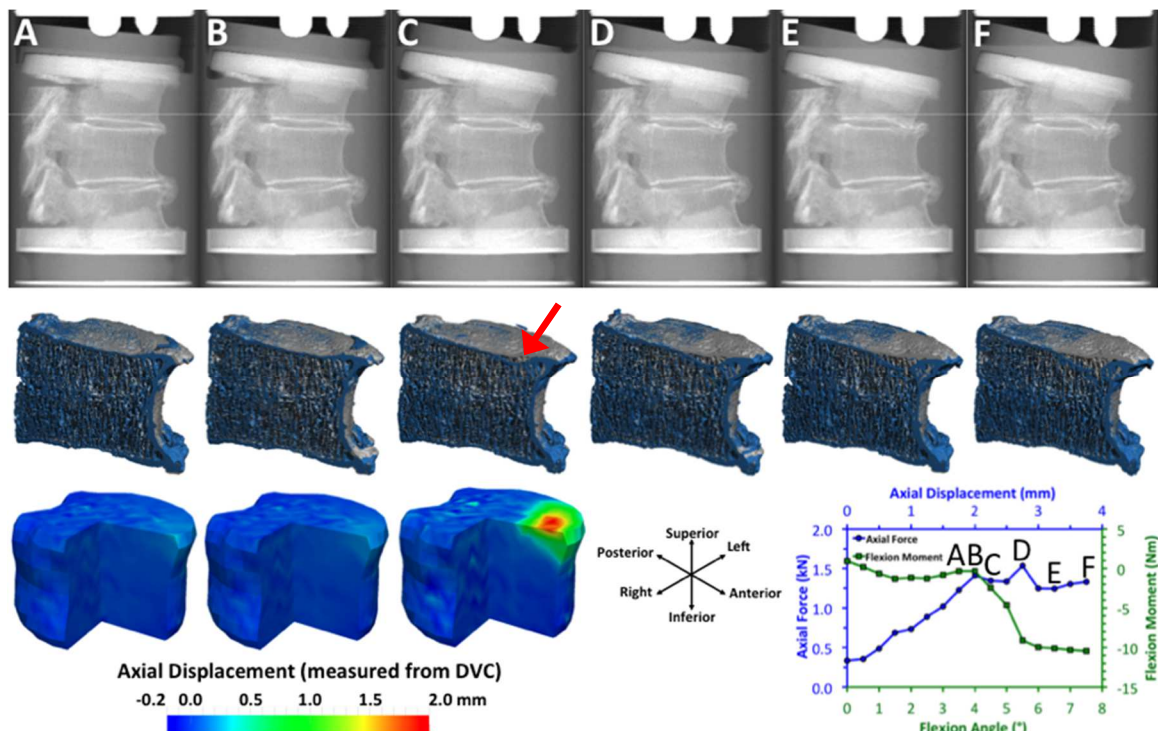


Figure 4.5 For anterior flexion: (Top) Lateral radiographic views (created from μ CT); (Middle) Sagittal half-section of vertebra before loading (gray) and at load increment (blue) noted on the load-displacement and moment-angle curve; (Bottom) For increments A–C, three-quarter section views of experimental displacement field in axial direction; positive values indicate downward displacement. The arrow indicates the site of initial deflection.

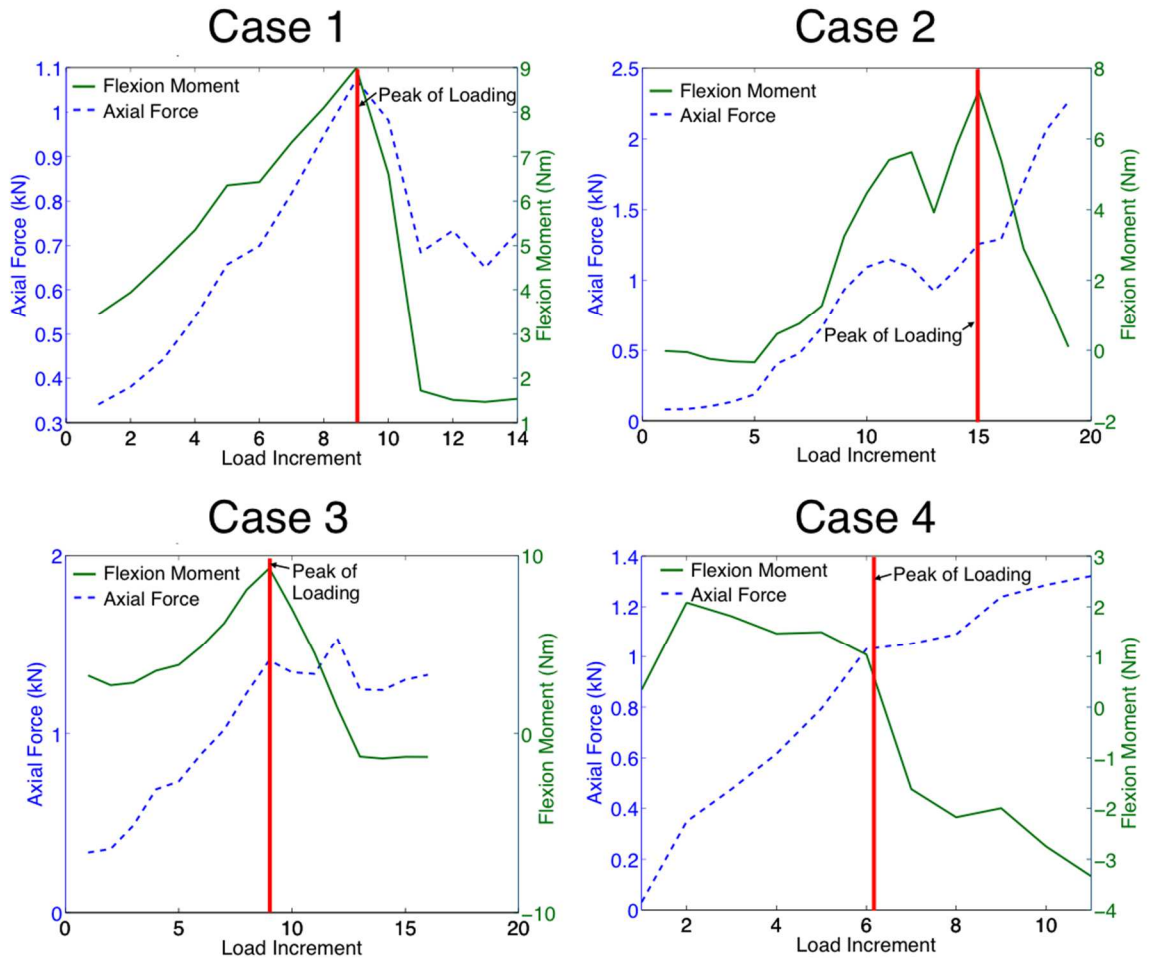


Figure 4.6 Axial force (dashed blue) and anterior moment (solid green) curves for four cases observed during mechanical testing; The vertical red line indicates the increment that corresponds to the peak of loading.

As damage progressed in the vertebral body after the peak of loading, the anterior cortex was observed to bulge anteriorly (Figure 4.7), and the anterior half of the superior endplate deformed while the posterior half remained largely intact. Deformation remained localized to the superior half of the vertebral body (Figure 4.8). At the peak of loading, maximum displacement of the anterior cortex in the anterior direction increased from 0.063 ± 0.062 mm (mean \pm standard deviation) to 0.256 ± 0.131 mm (mean \pm standard deviation) immediately after the peak of loading (Table 4.3). As a percentage of the maximum axial displacement in the endplate for the corresponding specimen and load increment, the maximum anterior displacement increased from 15.8 ± 12.7 % of the maximum endplate deflection at the peak of loading to 19.9 ± 7.2 % of the maximum endplate deflection at the increment immediately after the peak of loading (Figure 4.9). In addition, the maximum anterior bulge was correlated with the maximum endplate deflection at the increment immediately after the peak of loading (Figure 4.10; $R^2 = 0.385$, $p = 0.0179$).

Using a semi-quantitative technique³⁴ to assess vertebral fractures, no specimen reached the definition of a wedge fracture until *at least* two load increments after the peak of loading. By the fourth load increment after the peak of loading, five of 14 specimens met the criteria for both mild wedge and mild biconcave fracture, four of 14 specimens met the criteria for a mild wedge fracture only, two of 14 specimens met the criteria for a mild biconcave fracture only, and three of 14 specimens did not meet the criteria for any clinical fracture. No specimens met the criteria for a crush fracture at any load increment.

Table 4.3 Anterior flexion: Maximum anterior displacement in the anterior direction measured at and immediately after the peak of loading and increase in displacement between these two load increments, expressed in mm and as a percentage of the maximum endplate deflection in the corresponding specimen and load increment: values presented are mean \pm standard deviation (SD), minimum and maximum for the 14 specimens.

	Mean \pm SD mm (%)	Min. mm (%)	Max. mm (%)
Maximum Anterior Displacement at Peak of Loading	0.063 \pm 0.062 (15.8 \pm 12.7)	0.001 (0.5)	0.204 (47.3)
Maximum Anterior Displacement Immediately After Peak of Loading	0.256 \pm 0.131 (19.9 \pm 7.2)	0.075 (10.3)	0.565 (33.2)
Increase in Anterior Displacement	0.192 \pm 0.134 (22.9 \pm 12.9)	0.045 (4.6)	0.548 (40.0)

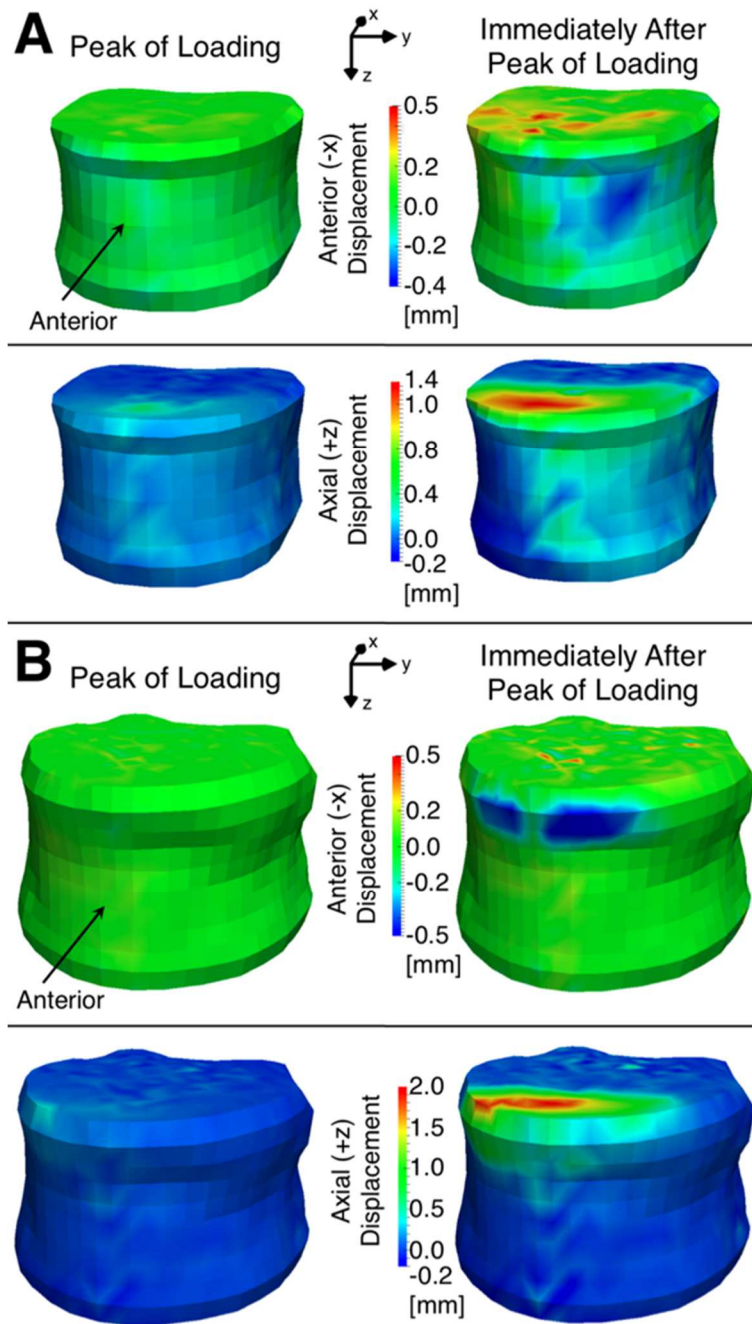


Figure 4.7 Experimental displacement fields in axial and anterior/posterior direction for a T8 vertebra featuring (A) initial deformation at the central endplate and (B) initial deformation at the anterior ring apophysis; Positive values in the axial direction indicate downward displacement and negative values in the anterior/posterior direction indicate anterior displacement.

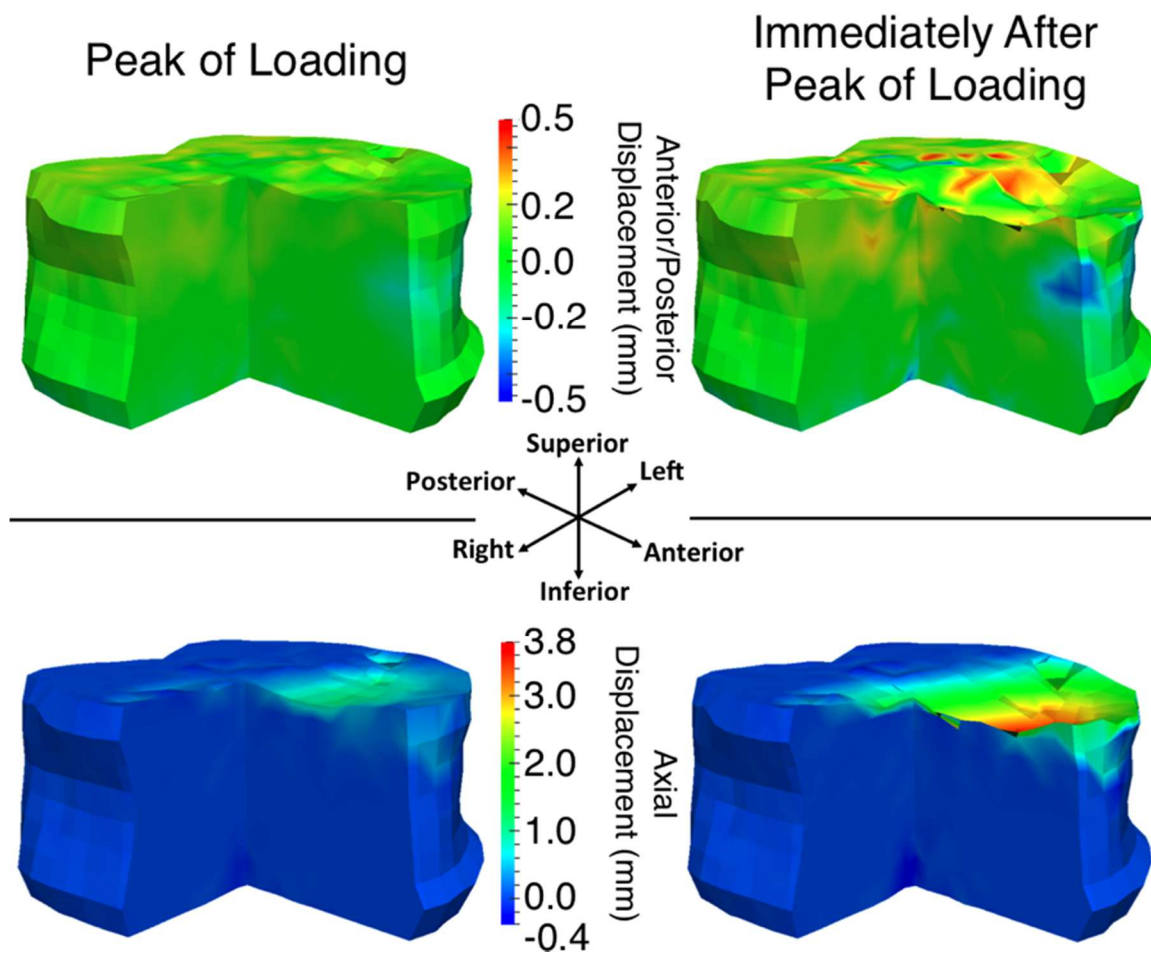


Figure 4.8 Three-quarter section views of experimental displacement fields in axial and anterior/posterior directions at and immediately after the peak of loading for a representative specimen loaded under anterior flexion; Positive values in the axial direction indicate downward displacement and negative values in the anterior/posterior direction indicate anterior displacement.

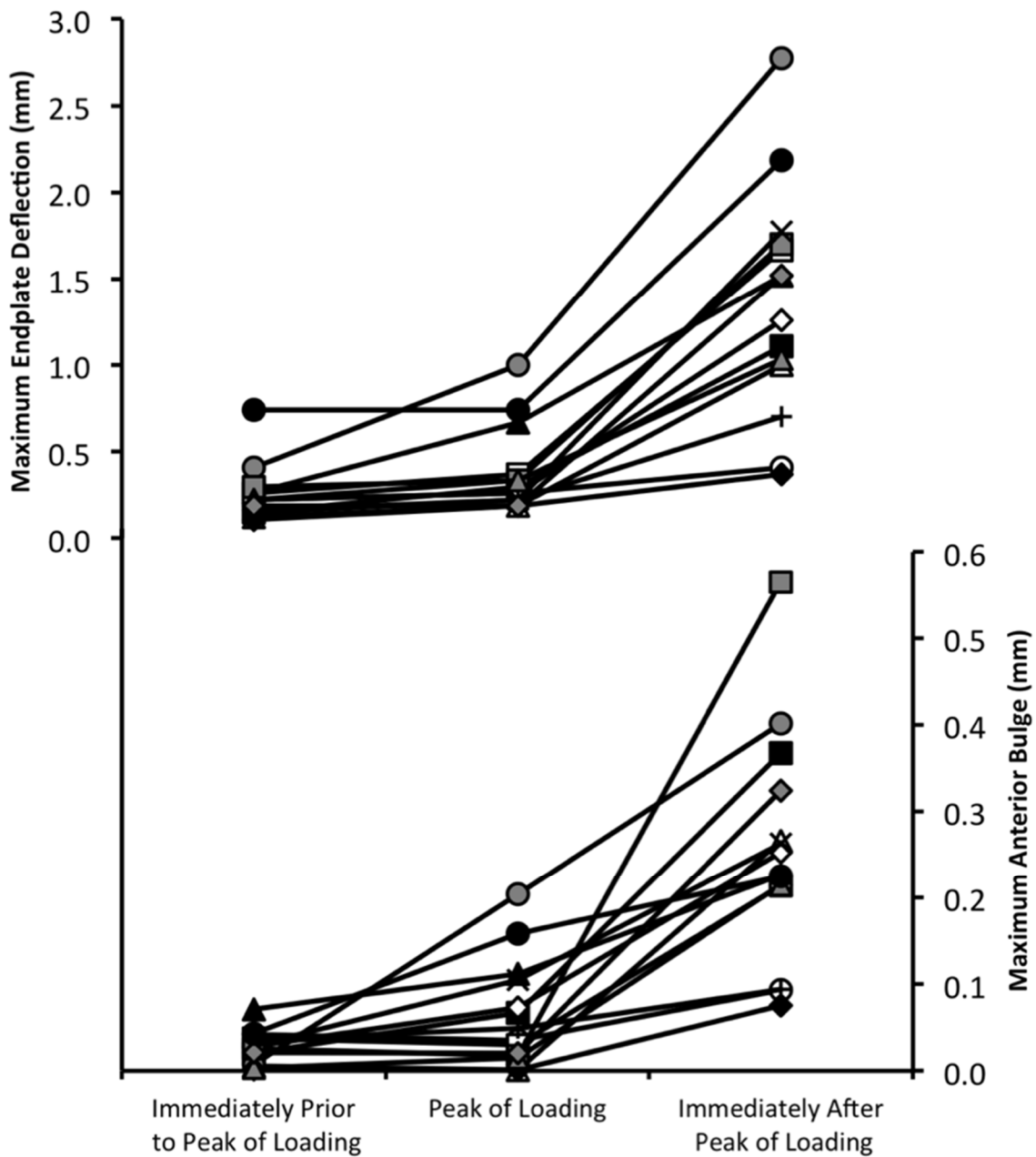


Figure 4.9 Maximum deflection in the superior endplate (top) and maximum anterior bulge (bottom) prior to, at, and after the peak of loading for all specimens loaded under anterior flexion; Each specimen has a unique marker.

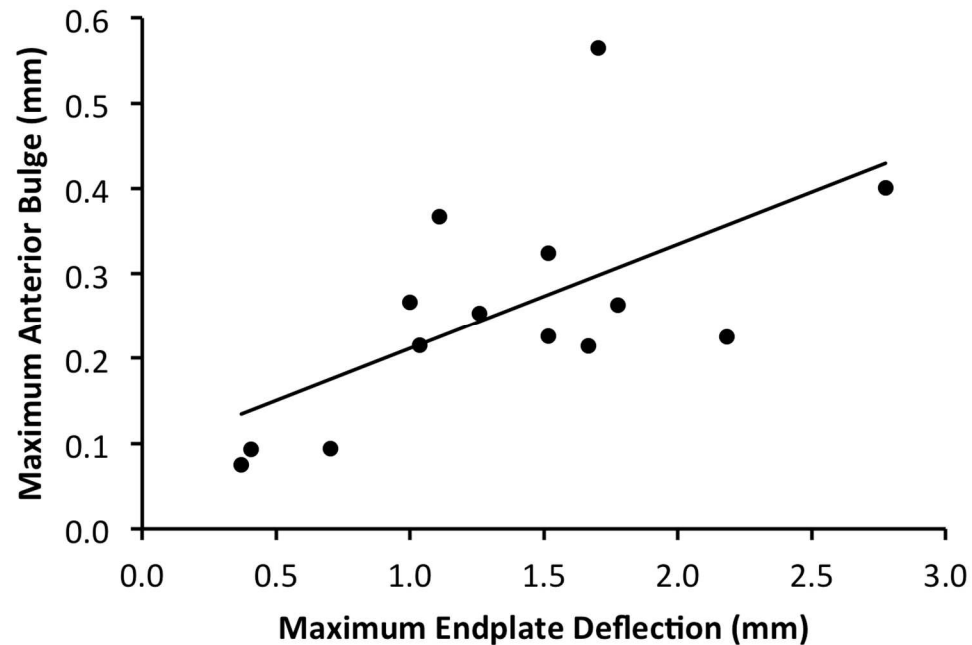


Figure 4.10 Linear regression of the maximum deflection in the superior endplate and maximum anterior bulge in the anterior cortex after the peak of loading for all specimens loaded under anterior flexion ($R^2 = 0.385$, $p = 0.0179$).

Endplate deflection was correlated with the volume fraction of the endplate and underlying trabecular bone irrespective of VOI distance and for all load increments. Endplate deflection was higher in regions with high Tb.Sp*, SMI, and DA ($p < 0.0001$) and lower in regions with high ρ_{app} , BV/TV, Tb.N*, ConnD, and Ep.BV/TV (Figure 4.11; $p < 0.0001$), though substantial variations were observed among specimens. At low distances between the VOI and the site of initial deflection, the curve for the predicted model between microstructure and endplate deflection was less pronounced in five, five, and four of 14 specimens for ρ_{app} , Tb.N*, and ConnD, respectively. By contrast, the curve for the predicted model between microstructure and endplate deflection was less pronounced in only one, two, and two of 14 specimens for DA, SMI, and Ep.BV/TV,

respectively. An effect of load increment was observed ($p < 0.001$) in that the aforementioned associations tended to weaken as loading progressed.

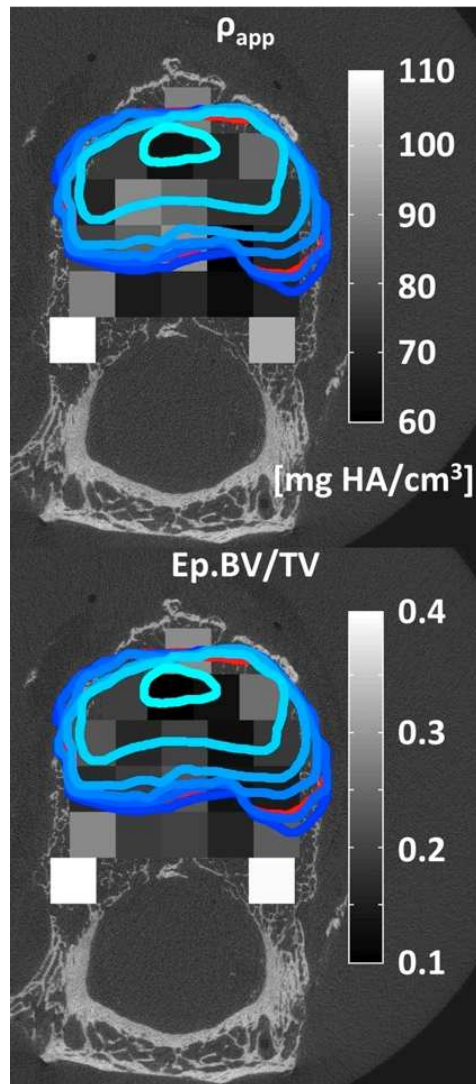


Figure 4.11 Regions of large endplate deflection (outlined in blue and red), defined as $>0.5\text{mm}$, and (above) distribution of apparent density in the VOIs of subchondral bone (grayscale) or (below) distribution of Ep.BV/TV in the VOIs of subchondral endplate (grayscale): The lightest blue outline corresponds to the increment at which endplate deflection clearly initiated. The boundaries at subsequent increments are represented with progressively darker shades of blue. The red outline corresponds to the unloaded scan.

Axial Compression

For the axial compression set, the superior endplate exhibited a marked increase in deflection that coincided with a drop in the load-displacement curve in ten of 14 specimens (Figure 4.12). In the remaining four specimens, the inferior endplate exhibited a similar increase in deflection coinciding with a drop in the load-displacement curve (Table 4.4). The average (\pm standard deviation) maximum deflection of the deflecting endplate was 0.46 (\pm 0.26) mm at the ultimate point and then increased 1.04 (\pm 0.26) mm (Table 4.5) at the increment immediately following the ultimate point (Figure 4.13). For all specimens, the deflection in the opposite endplate of the vertebra never exceeded 0.2 mm. The sites of initial endplate deflection for each specimen varied: two at the anterior ring apophysis, three at the anterior central endplate, six at the medial central endplate, two at the mediolateral ring apophysis, and one at the posterior ring apophysis (Figure 4.14). Using contingency analysis, no apparent pattern of ALDI score and the site of initial deflection was observed ($p > 0.54$): An ALDI score of 0, 1, and 2 was observed for one, two, and 3 specimens, respectively, that featured initial deflection in the ring apophysis; and an ALDI score of 0, 1, and 2, was observed for three, one, and four specimens, respectively, that featured initial deflection in the central endplate.

Table 4.4 Axial compression: Experimentally measured ultimate force (in N) and the drop in force occurring after the ultimate point (in N and as a percentage of the ultimate force) for the axial compression set: values presented are mean \pm standard deviation (SD), minimum and maximum for the 14 specimens.

		Mean \pm SD	Min.	Max.
Ultimate Force (N)		2,369 \pm 944	758	3,881
Force Drop Following Ultimate Point	N	160 \pm 155	16	570
	%	6.8 \pm 6.6	1.3	21.8

Table 4.5 Axial compression: Maximum endplate deflection measured before and after the load drop and increase in deflection between these two load increments, expressed in mm and as a percentage of the height of the vertebral body: values presented are mean \pm standard deviation (SD), minimum and maximum for the 14 specimens of the axial compression set.

	Mean \pm SD	Min.	Max.
	mm	mm	mm
	(%)	(%)	(%)
Maximum Deflection at Ultimate Point	0.46 \pm 0.26 (2.4 \pm 1.3)	0.11 (0.6)	1.04 (5.0)
Maximum Deflection at After Load Drop	1.49 \pm 0.54 (7.7 \pm 2.8)	0.56 (2.8)	2.78 (14.4)
Increase in Deflection	1.04 \pm 0.53 (5.4 \pm 2.8)	0.26 (1.3)	2.22 (11.5)

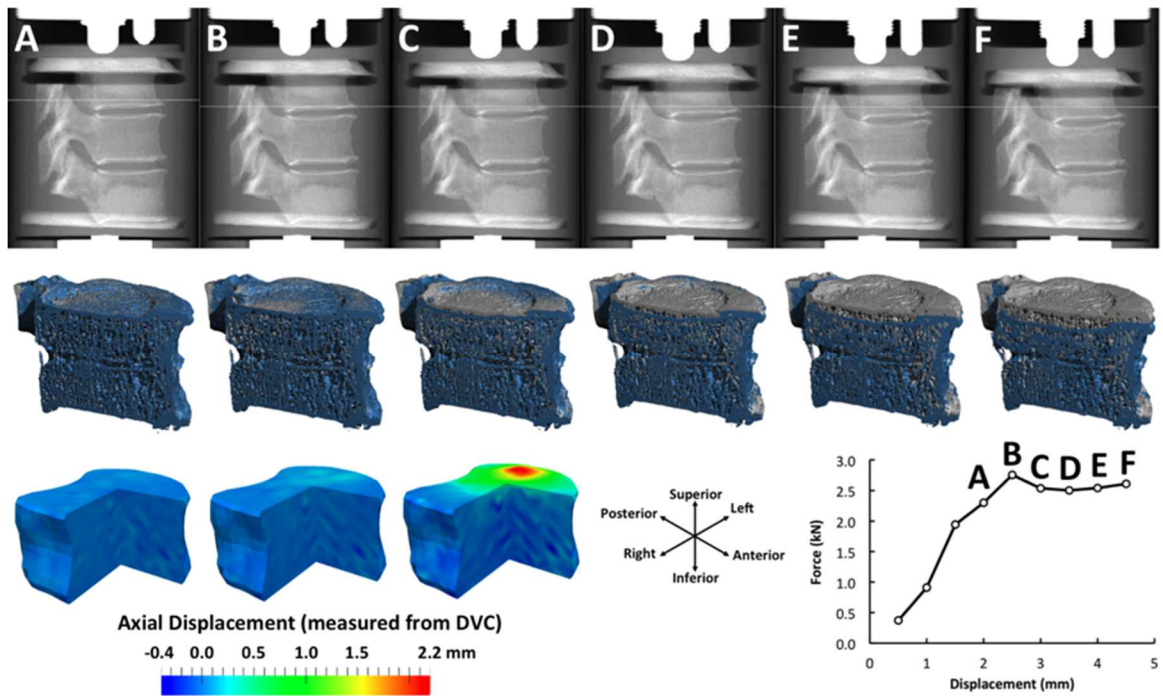


Figure 4.12 For axial compression: (Top) Lateral radiographic views (created from μ CT); (Middle) Sagittal half-section of vertebra before loading (gray) and at load increment (blue) noted on the load-displacement curve; (Bottom) For increments A–C, three-quarter section views of experimental displacement field in axial direction; positive values indicate downward displacement.

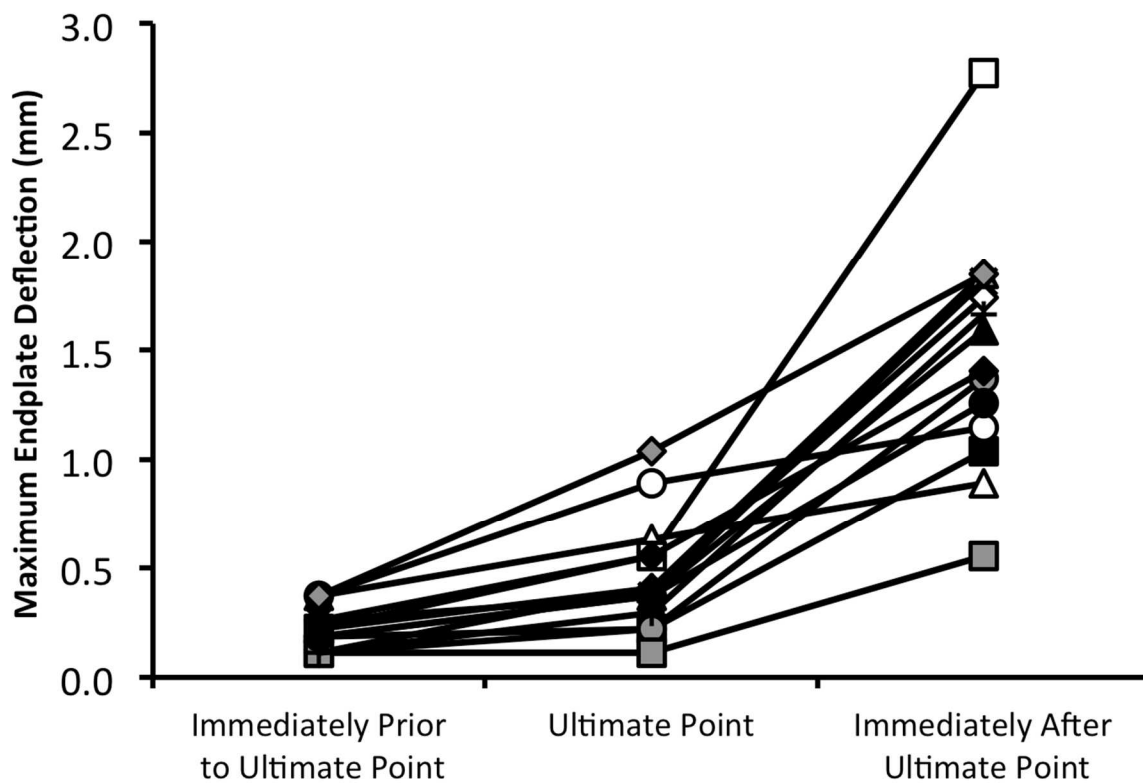


Figure 4.13 Maximum deflection in the superior endplate prior to, at, and after the ultimate point for all specimens loaded under axial compression; Each specimen has a unique marker.

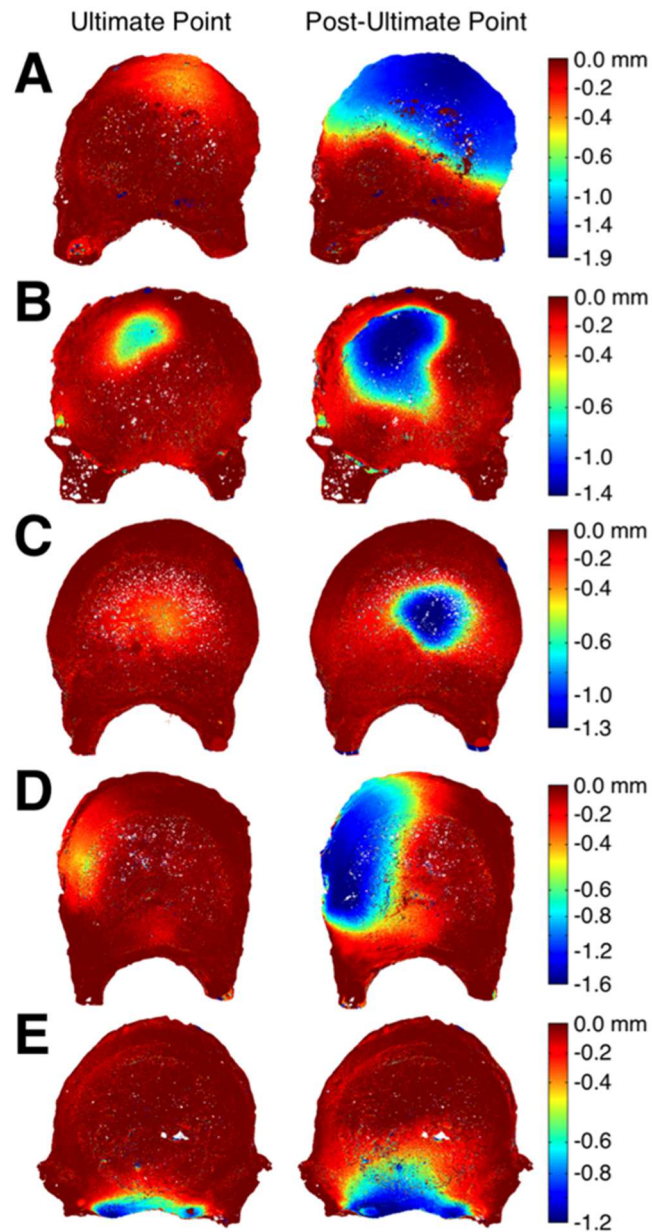


Figure 4.14 Axial deflection (negative values indicate downward movement) in the endplate at and immediately following the ultimate point for a representative case of initial endplate deflection at (A) the anterior ring apophysis, (B) the anterior central endplate, (C) the medial central endplate, (D) the mediolateral ring apophysis, and (E) the posterior ring apophysis. The deflection colorscale is nonlinear, and the center of each site of initial deflection was used for qualitative comparison in Figures 4.16 and 4.18.

As damage progressed after the ultimate point, the cortex was observed to specimens that featured axial endplate deflection at or near the ring apophysis. The cortex near the region of localized axial deformation was often observed to bulge outward. In contrast to the anterior bulge observed in specimens loaded to failure under anterior flexion, the outward bulging observed in specimens loaded to failure under axial compression was at or just inferior to the ring apophysis (Figure 4.15). In specimens that featured deformation observed only in the central endplate, no bulge was observed in the cortex.

Using a semi-quantitative technique to assess vertebral fractures, only one specimen reached the definition of a biconcave fracture within two load increments after the ultimate point. By the third load increment after the peak of loading, three of 14 specimens met the criteria for both mild wedge and mild biconcave fracture, no specimens met the criteria for a mild wedge fracture only, six of 14 specimens met the criteria for a mild biconcave fracture only, and five of 14 specimens did not meet the criteria for any clinical fracture. No specimens met the criteria for a crush fracture at any load increment.

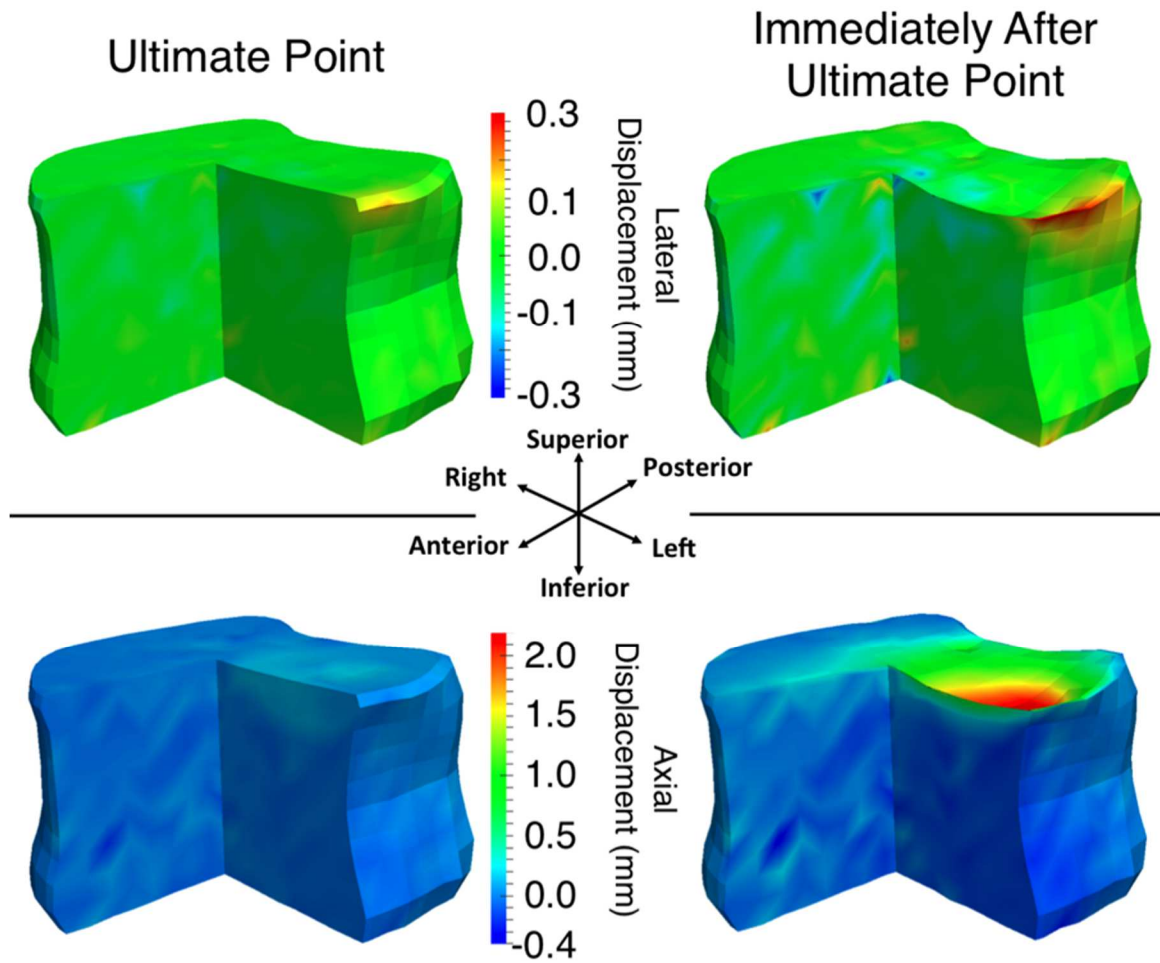


Figure 4.15 Three-quarter section views of experimental displacement fields in axial and lateral directions at and immediately after the ultimate point for a representative specimen loaded under axial compression; Positive values in the axial direction indicate downward displacement and positive values in the lateral direction indicate displacement towards the left.

DISCUSSION

With studies observing that initial failure tends to occur at the central endplate for vertebrae tested in compression and under moderate amounts of flexion,³⁷ the goal of this study was to investigate the development of fracture patterns as the vertebrae were loaded to failure under anterior flexion or axial compression. Localized regions of deformation were observed for specimens loaded under both types of loading. While the site of initial deflection was observed at or just anterior to the anterior central endplate for specimens tested under anterior flexion, the sites of initial deflection were more widely dispersed across the endplate surface for specimens loaded under axial compression (Figure 4.16). Irrespective of the loading applied, endplate deflection was commonly observed at the central endplate, indicating that the central endplate may play a vital role in the initial development of vertebral fractures.

Under anterior flexion, we found that initial damage tends to occur at or near the anterior central endplate and, at least within the relatively coarse temporal resolution of this study, simultaneously at the anterior cortex. At and after the peak of loading, the ratio of maximum anterior bulge to maximum endplate deflection increased only mildly. As loading continued after the peak of loading, damage then progressed anteriorly and inferiorly, while the posterior half of the vertebra remained intact, leading to a pattern of wedge fracture. Upon a marked increase in endplate deflection, the ability of the vertebral body to support bending moments had been compromised for all four loading cases (Figure 4.6), even before the development of a clinical wedge fracture pattern.

After the peak of loading, the anterior moment was markedly reduced while the axial load may or may not have decreased. This finding suggests that, at least initially, damage to the anterior endplate may not affect the ability of the vertebra to carry axial loads but may inhibit the vertebra's ability to support anterior bending moments. Specimens observed in this study with a negative anterior moment at the peak of loading had experienced damage to the anterior region of the inferior T7 endplate during loading, while the remaining spine segments featured damage only to the superior half of the T8 vertebra. While the damage at the adjacent vertebra corresponded to a drop in bending moment, all specimens exhibited further decline in anterior bending moment after the peak of loading.

The central endplate may play a vital role in the initiation of a clinical fracture. The minimum clinical standard for a wedge fracture was met more frequently when the specimen was loaded under anterior flexion compared to axial compression. In contrast, biconcave fractures, indicating deflection in the central endplate relative to the posterior ring apophysis, were observed to develop irrespective of the loading applied. The minimum standard for a biconcave fracture was commonly observed for specimens loaded under either anterior flexion or axial compression, suggesting that deflection in the central endplate is a defining feature of vertebral fracture regardless of the applied loading.

The inclusion of the neural arch in mechanical testing appears to bolster the load-carrying capacity of the vertebra and largely reduce the frequency of failures initiating at the posterior ridge of the endplate. When compared to L1 vertebrae (loaded under axial

compression with the posterior elements removed; Table 2.1), the average vertebral strength of the T8 vertebrae (loaded under axial compression with the neural arch intact; Table 4.4) was higher despite being smaller vertebrae. The bone mineral density from the largest cylindrical ellipse that could fit in the trabecular bone of the vertebral body was computed and normalized by the cross-sectional area of the ellipse for both the T8 and L1 vertebral bodies. An analysis of covariance performed between the two data sets found a trend ($p = 0.0556$) that T8 vertebrae were stronger for a given amount of bone per unit height than the L1 vertebrae (Figure 4.17). McCubbery et al. measured vertebral strength for spine segments without posterior elements.⁸² The mean L1 strength was within 0.5 standard deviations of the vertebral strength reported by McCubbery et al., however the mean strength for T8 vertebrae with an intact neural arch was 1.5 standard deviations above the mean reported by McCubbery et al.⁸² While the mean L1 strength fell within the reported range for specimens that are tested without posterior elements, the mean T8 strength with the neural arch intact poorly matches the mean T8 strength for vertebrae without posterior elements. Further, failure in the L1 vertebrae with removed posterior elements was observed primarily in the posterior half of the endplate, causing the posterior cortical shell to buckle outward. The vertebrae with intact neural arches featured relatively few failures in the posterior half (Figure 4.18), indicating that the neural arch plays a significant role in vertebral strength and in the post-failure deformation patterns that occur in the vertebral body. Future studies that include biomechanical testing of spine segments should strongly consider keeping the neural arch intact if possible.

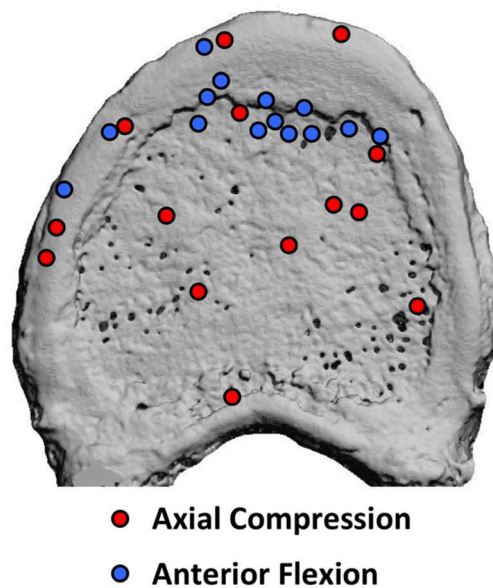


Figure 4.16 Relative location of the center of the initial endplate deflection site for spine segments loaded under axial compression and anterior flexion

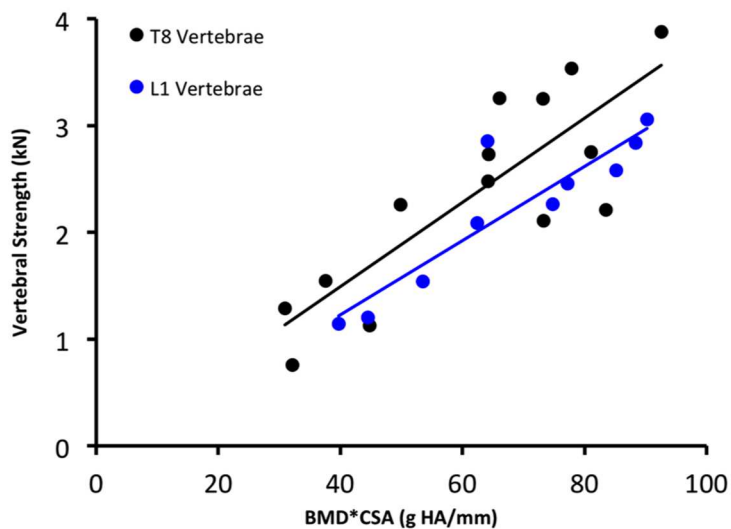


Figure 4.17 Vertebral strength vs. bone mineral density multiplied with cross sectional area for T8 ($R^2 = 0.70$) and L1 ($R^2 = 0.82$) vertebrae, as determined by examining the bone mineral density and transverse area of the largest elliptical cylinder that fit in the centrum of the vertebral body; The T8 vertebrae featured an intact neural arch, whereas all posterior elements were removed from the L1 vertebrae.

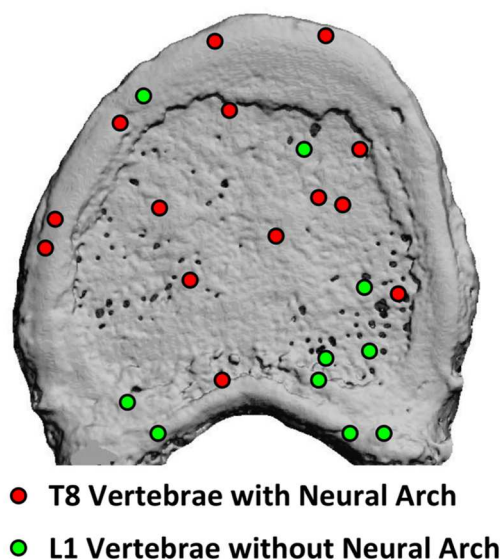


Figure 4.18 Relative location of the center of the initial endplate deflection site for T8 and L1 vertebrae loaded to failure under axial compression; The posterior elements of the L1 vertebrae were removed (Chapter 2) while the T8 vertebrae featured an intact neural arch and zygapophysial joints

A novel aspect of this study is that it examined both the initiation and progression of wedge fracture patterns using quantitative assessments from displacement fields throughout the vertebral body, and the deflections at the endplates and anterior cortex were measured with high spatial resolution. Another strength of this study is that, similar to prior studies under axial compression,⁵⁴ it allowed for the direct comparison between observed deflections in the endplate and anterior cortex and the ability of the vertebral body to carry loads.

The limitations of this study primarily involve the biomechanical testing procedures. First, as with similar experimental procedures,^{48,54} the temporal resolution of deflection data was coarse, providing on average only 15 load increments and as few as

four increments after initial deformation was observed near the endplates of T8. The number of increments was limited because of long scan times and the perishable nature of the tissue. Ancillary time-course experiments of five L3 vertebrae scanned repeatedly over 72 hours showed no change in attenuation of the bone tissue ($p > 0.08$). In contrast, marrow attenuation decreased 27% on average over 72 hours in four of the specimens ($p < 0.01$). Thus, the current protocol is sufficient for quantifying bone parameters over several days, but the prospect of increasing the duration must be evaluated with caution. Due to the coarse temporal resolution, the finding that the endplate and anterior cortex were observed to deflect simultaneously under anterior flexion should be interpreted with caution. Future studies with real-time loading and imaging or even with reduced scan times would be better suited to identify the precise nature of the relationship between endplate deflection and deformation in the anterior cortex. Second, while the neural arch of T8 and the T7–T8 and T8–T9 zygapophysial joints were left intact so that the loading of the T8 vertebra would remain as physiologically relevant as possible, a notch was cut into the posterior elements of the T7 and T9 vertebrae to prevent the posterior elements from becoming embedded in the bone cement, on which the loading was applied. This was done to simplify the biomechanics involved and ensure that the load was transferred through the vertebral bodies. Some fraction of the load would likely be transferred through the T7/T8 and T8/T9 zygapophysial joints and the extent to which this loading has been modified from *in-vivo* conditions remains unclear. Third, static loads differ from the dynamic loading conditions experienced *in vivo*.⁴⁶ Sustained loading exudates fluid from the IVD, causing a drop in NP pressure that shifts the load distribution to the

periphery.⁸³ However, the ultimate loads recorded in this study agree with those obtained from continuous loading of lumbar vertebral segments.⁸² Prior studies of trabecular bone have also shown good correlation between mechanical properties obtained with continuous vs. step-wise loading.⁹¹ Fourth, T7 and T9 were partially cored and filled with bone cement to ensure that failure occurred in T8. While at least 5mm of trabecular bone were left intact near the endplates adjacent to T8, the bone cement would likely have some effect on the load distribution transmitted to T8. Furthermore, failure occurred in these regions of intact trabecular bone at T7 in five specimens. Despite failure initiating in T7, loading continued and the initiation of a wedge fracture pattern was observed at T8 for all specimens.

In spite of these limitations, this study demonstrates that endplate deflection was commonly observed at the central endplate irrespective of the loading applied, suggesting that the central endplate plays a vital role in the initial development of vertebral fractures. Under moderate amounts of flexion, vertebral failure tends to initiate at or just anterior to the central endplate, and damage then progresses inferiorly and anteriorly to exhibit a wedge fracture pattern. Clinical observation of large endplate deflection in the central/anterior endplate may indicate that the ability of the vertebra to support loads has been markedly reduced.

CHAPTER FIVE

**ACCURACY OF QCT-BASED FINITE ELEMENT PREDICTIONS
OF VERTEBRAL FRACTURE UNDER AXIAL COMPRESSION
AND ANTERIOR FLEXION**

INTRODUCTION

Vertebral fractures are the most common type of osteoporotic fracture¹³ and are associated with increased morbidity¹⁴ and mortality.¹⁵ Identifying patients with incident and prevalent fractures has been a subject of disagreement among clinicians: About one half of vertebral fractures may be asymptomatic, and the natural variation in vertebral shape may confound the classification of mild fractures.²⁶ Currently, measurements of bone mineral density (BMD) are used to estimate fracture risk, but these values only explain ~60% of the variation in vertebral strength¹⁶ and almost half of patients with vertebral fractures do not exhibit osteoporotic levels of BMD.⁶⁴ BMD measurements do not incorporate factors that may be critical to vertebral strength, such as: variation in intervertebral microstructure, vertebral geometry, and the load distributions applied to the endplates. Patient-specific finite element (FE) models built from quantitative computed tomography (QCT) scans allow for predictions of bone strength and fracture patterns.^{18,20,21,30} If fully validated, these QCT-based FE models could provide accurate noninvasive analyses with many applications, including the assessment of the efficacy of new drug therapies and orthopaedic implant designs.

While the QCT-based FE models have promise for accurate predictions of vertebral strength and fracture risk, the advantage of QCT-based FE models over bone mineral density (BMD) for estimating fracture risk is not yet fully established.^{11,17,20,21}

Wang et al. and Kopperdahl et al. have demonstrated that clinically assessed FE-computed strength can predict fracture risk as well or better than BMD-based techniques;^{70,131} however the accuracy of these models for predicting vertebral strength under loading associated with wedge fractures has been questioned.⁹ Further, for the FE model to be an appropriate clinical tool for both fracture prevention and implant design, QCT-based simulations should accurately predict the clinically observed failure patterns and not just vertebral strength. Even for simple axial compression of the spine, loading across the vertebral endplate is highly non-uniform,⁵⁴ suggesting that QCT-based FE simulations must carefully consider the choice of boundary conditions. Using measured deformation fields obtained from digital volume correlation (DVC) analyses of time-lapsed micro-computed tomography (μ CT) images as a gold standard, a recent study found substantial inaccuracies in FE analyses that used highly idealized boundary conditions.⁵¹

The overall goal of this study was to assess the accuracy of vertebral strength and failure patterns in nonlinear FE analyses for spine segments loaded under both axial compression and anterior flexion. The objectives were: 1) to examine whether FE analyses incorporating experimentally observed deflections at the endplates improved predictions of vertebral strength and failure patterns within the vertebra when compared to idealized loading conditions; and 2) to determine if boundary conditions based on non-invasive assessments of intervertebral disc (IVD) health can improve FE predictions of vertebral failure.

METHODS

Specimen Preparation

Twenty-eight T7–T9 spine segments were dissected from fresh-frozen human spines (age: 35–91 years; 8 male, 6 female; NDRI, Philadelphia, PA, and LifeLegacy Foundation, Tucson, AZ) by making transverse cuts through the T6–T7 and T9–T10 IVDs and removing soft tissue of the exposed IVDs. A notch was cut into the posterior elements on T7 and T9 such that the posterior elements and zygapophysial joints remained intact but no load was applied to them. The trabecular bone in the T7 and T9 vertebral bodies was hollowed out with a dental tool (Komet USA, Rock Hill, SC) and filled with polymethyl methacrylate (PMMA), leaving *at least* 5mm of trabecular bone near the T8 vertebra. This procedure was performed on the vertebrae adjacent to T8 to ensure that the spine segment failed at T8, while the remaining trabecular bone was left to maintain loading contains as physiologically relevant as possible. The exposed endplates of the T7 and T9 vertebral bodies were potted in circular dishes filled with PMMA. The spine segments were kept hydrated at all times and, when not in use, wrapped in saline-soaked gauze, sealed in plastic bags, and stored at -20°C.

Mechanical Testing and Imaging

The 28 dissected spine segments were randomly assigned to a set for testing under axial compression (n = 14) and a set for testing under axial compression (n = 14) with anterior flexion. Each spine segment was first imaged with quantitative computed tomography (QCT; GE Lightspeed VCT; GE Healthcare, Milwaukee, WI;

0.3125x0.3125x0.625 mm/voxel) and then placed in a custom-built, radiolucent device for mechanical testing (Figure 4.2). After ten cycles of preconditioning to ~300N, the spine segments were imaged with μ CT (μ CT 80; Scanco Medical, Brüttisellen, Switzerland; 37 μ m/voxel). The settings for voltage, current and integration time were 70 kVp, 114 mA, and 300 ms, respectively. Each specimen was then loaded in a stepwise manner (0.5mm per step for axial compression; 0.25mm and 0.5° per step for anterior flexion).^{48,54} The compression screw and flexion screw applied the axial compression and angle, respectively, of each step, while the level screws ensured that the angle was only applied in the sagittal plane. After a 20-minute relaxation period, the loaded specimen underwent another μ CT scan with the same scan settings. This stepwise loading continued to failure, identified by visible deformation in the T8 vertebral body via lateral scout views. For specimens tested under anterior flexion, the forces and moments experienced by the spine segment were obtained for each load increment using the calibration layer as discussed in Chapter Three. The axial load for specimens tested under axial compression was obtained with a load cell inserted into the bottom of the mechanical testing device.

Digital Volume Correlation

The methods for using DVC with time-lapsed μ CT images of human vertebrae were reported previously.⁴⁸ Briefly, image registration (IPL; Scanco Medical) was used to align the series of images of the T8 vertebral body. A minimum acceptable correlation coefficient between pairs of registered images was set at 0.8; visual inspection of image sets was also performed to ensure the image sets were properly aligned. An irregular

mesh that conforms to the geometry of the vertebral body was generated using hexahedral elements with ~1.9mm side lengths (Figure 4.3).

Maximum Likelihood Estimation is an iterative process used to find the displacements at the nodes of each subregion such that the subregions best match the intensities between the two image sets. Displacements at the nodes were determined by finding the displacement field $\mathbf{u}(x)$ that minimized the functional π :^{78,104}

$$\pi(\mathbf{u}(x)) = \frac{1}{2} \int_{\Omega} (I_1(x) - I_2(x + \mathbf{u}(x)))^2 d\Omega + \frac{1}{2} \int_{\Omega} \alpha (\nabla \mathbf{u}(x) : \nabla \mathbf{u}(x)) d\Omega \quad \text{Eq. 5.1}$$

where I_1 and I_2 are image intensities for the two image sets, Ω is the image domain, and α is a scalar regularization parameter that punishes large displacement gradients. To find the optimal value of α , an artificial displacement was applied to a set of images and the optimal value of α yielded the most accurate displacement field. All calculations using the MLE method were performed on a supercomputing system (2 eight-core 2.6 GHz, Intel Xeon E5-2670 processors with 256 GB shared RAM) until it converged to an acceptable solution and output displacements at each node.

IVD Grading

Using QCT images of a mid-transverse cross-section of each IVD, a trained observer assigned each disc an “apparent loss of disc integrity” (ALDI) score.⁴⁹ The ALDI grading scale is based on prior observations that IVD degeneration initiates with dehydration in the nucleus pulposus (NP),¹² which decreases swelling pressure and progresses to a loss of demarcation between the NP and annulus fibrosus (AF).^{6,100,119} The ALDI scale was developed from comparisons of transverse and sagittal QCT images

to histological sections, noting that a dark, central region in the QCT images corresponds to a healthy nucleus pulposus (NP). This difference in CT attenuation would be expected based on the high water content of healthy NP tissue. A loss of discernibility of the presumptive NP and/or the appearance of fissures indicated degenerative changes, with the presence of osteophytes being a secondary indicator.

Nonlinear FE Analyses

Voxel-based FE models of T8 were generated from QCT images (Figure 5.1). The boundary of the vertebra (including endplates and posterior elements) was defined using a semi-automated segmentation technique (Amira 5.6, Visage Imaging, Inc., San Diego, CA). Each voxel was converted into a hexahedral element with a 0.625mm side length. The mesh for each FE model consisted of approximately 90,000 elements and the run-time typically ranged from 5–10 hours (2.6 GHz, Intel Xeon E5-2670 processor with 128 GB shared RAM). Isotropic, linear elastic material properties and yield strength were assigned based on local bone mineral density.^{68,71} The mineral density was averaged for each FE element and the elastic modulus along the axial direction (E_{zz} , MPa) was assigned based on the experimentally determined relationship:⁷¹

$$E_{zz} = -34.7 + 3.230\rho_{QCT} \quad \text{Eq. 5.2}$$

where ρ_{QCT} is the bone mineral density in mg/cc. Any negative modulus values obtained by the above relationship for elements with low density values caused by air bubbles or large gaps in trabecular structure were assigned an elastic modulus of 0.1 kPa. The Poisson ratio was set for all elements:^{124,125}

$$\nu_{xy} = 0.381. \quad \text{Eq. 5.3}$$

Post-yield material behavior was modeled with two yield criteria: a crushable foam (CF) and von Mises (VM) yield surface (Abaqus FEA 6.12, Dassault Systèmes, Vélizy-Villacoublay, France). For the von Mises FE model, transversely isotropic elastic properties were determined based on the following ratios and values:^{90,123,124}

$$E_{vM,xx} = 0.333E_{zz} \quad \text{Eq. 5.4}$$

$$E_{vM,yy} = 0.333E_{zz} \quad \text{Eq. 5.5}$$

$$G_{vM,xy} = 0.121E_{zz} \quad \text{Eq. 5.6}$$

$$G_{vM,zx} = 0.157E_{zz} \quad \text{Eq. 5.7}$$

$$G_{vM,yz} = 0.157E_{zz} \quad \text{Eq. 5.8}$$

$$\nu_{vM,xz} = \nu_{vM,yz} = 0.104. \quad \text{Eq. 5.9}$$

For the crushable foam model, isotropic material properties were required and set to E_{zz} and ν_{xy} . The crushable foam plasticity model can be described by hydrostatic pressure p and von Mises stress q such that:⁶⁸

$$p = \frac{1}{3} \text{trace}(\boldsymbol{\sigma}) \quad \text{Eq. 5.10}$$

$$q = \sqrt{\frac{2}{3} \boldsymbol{\sigma}_{dev} : \boldsymbol{\sigma}_{dev}} \quad \text{Eq. 5.11}$$

where $\boldsymbol{\sigma}$ is the Cauchy stress and $\boldsymbol{\sigma}_{dev}$ is the deviatoric component of the Cauchy stress.

With these definitions, the yield surface $f(p, q)$ of the crushable foam model (Figure 5.2) can be expressed as a function of the hydrostatic pressure and von Mises stress:

$$f(p, q) = \sqrt{q^2 + \alpha^2(p - p_m)^2} - B = 0 \quad \text{Eq. 5.12}$$

where the parameters p_m , α , and B of the yield surface are related to the hydrostatic pressure in compression $p_{c,y}$ and tension $p_{t,y}$ by:

$$p_m = \frac{p_{c,y} - p_{t,y}}{2} \quad \text{Eq. 5.13}$$

$$B = \alpha \frac{p_{c,y} + p_{t,y}}{2}. \quad \text{Eq. 5.14}$$

The yield surface can be described by two dimensionless stress ratios:

$$k_c = \frac{\sigma_{c,y}}{p_{c,y}} \quad \text{Eq. 5.15}$$

$$k_t = \frac{p_{t,y}}{p_{c,y}} \quad \text{Eq. 5.16}$$

where $\sigma_{c,y}$ is the compressive yield stress. With these definitions, the parameters p_m , α , and B that defined the yield surface (Eq. 5.12) can be rewritten in terms of only these two dimensionless stress ratios and the compressive yield surface:

$$\alpha = \frac{3k_c}{\sqrt{(3k_t + k_c)(3 - k_c)}} \quad \text{Eq. 5.17}$$

$$p_m = \alpha \frac{\sigma_{c,y}}{2k_c} (1 - k_t) \quad \text{Eq. 5.18}$$

$$B = \alpha \frac{\sigma_{c,y}}{2k_c} (1 + k_t) \quad \text{Eq. 5.19}$$

Based on the crushable foam model demonstrated by Kinzl et al., the yield surface was defined by dimensionless stress ratios of 1.181 and 0.540 in compression and tension, respectively.⁶⁸ The post-yield behavior was modeled as perfectly plastic behavior with equivalent compressive and tensile yield stresses. The yield stress (σ_y , MPa) for each element was assigned based on the experimentally determined relationship:⁷¹

$$\sigma_y = -0.75 + 0.0249\rho_{QCT}. \quad \text{Eq. 5.20}$$

The strength properties and moduli were scaled by a factor of 1.28 to account for side-artifact errors that were observed for the experimental relationships.^{122,123}

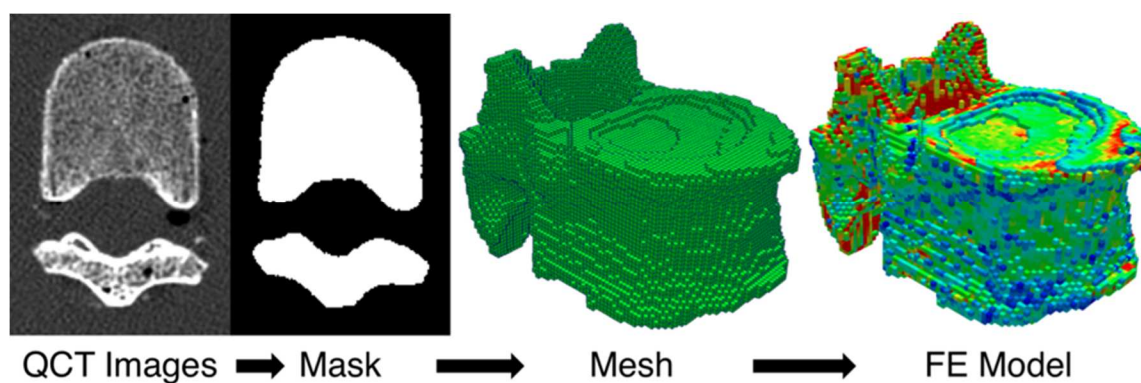


Figure 5.1 Procedure to develop specimen-specific, QCT-based FE models

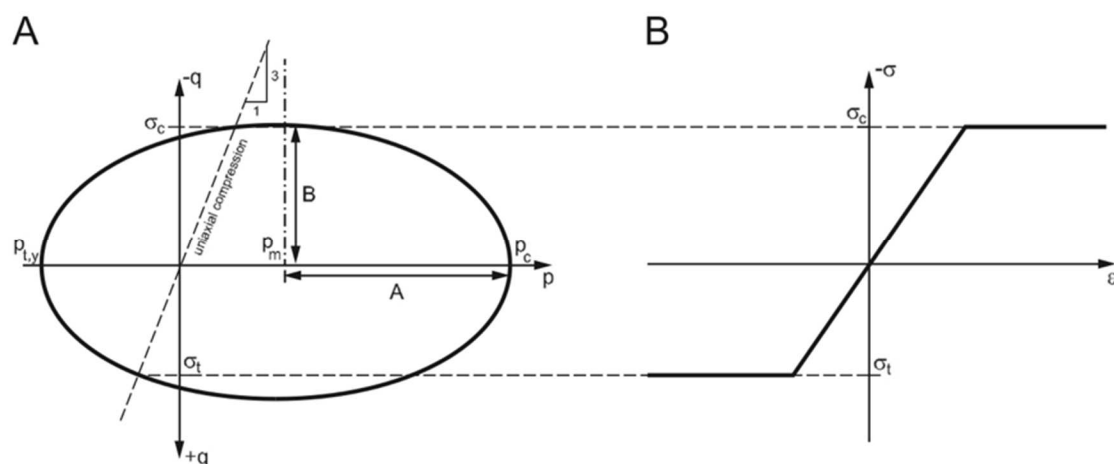


Figure 5.2 Yield surface of the crushable foam material model with the parameters that define the shape.

Intradiscal Pressure Measurements

The methods describing the experimental procedure for collecting intradiscal pressure measurements have been reported elsewhere.²³ Briefly, 26 thoracic spine segments (eight T9–T11 and 18 T10–T12; NDRI, Philadelphia, PA, and LifeLegacy Foundation, Tucson, AZ) were dissected from fresh-frozen human spines (age: 35–86

years; mean \pm standard deviation: 68 ± 16 ; 16 male, 10 female) by making a transverse cut through the IVD and removing all IVD tissue. A notch was cut into the posterior elements on the outer vertebrae such that the posterior elements and zygapophysial joints remained intact but no load was applied to them. The exposed endplates of the vertebral bodies were potted in circular dishes filled with PMMA. Spine segments were imaged using QCT performed with a LightSpeed VCT CT system (GE Healthcare, Cleveland, OH, USA) with resolutions of either $0.3125 \times 0.3125 \times 0.625$ mm or $0.3906 \times 0.3906 \times 0.625$ mm. Using the QCT image of a mid-transverse cross-section, a trained observer who was blind to information on donor characteristics and pressure measurements assigned each disc an “apparent loss of disc integrity” (ALDI) score.⁴⁹ Prior to mechanical testing, the spine segments were thawed in a phosphate buffer solution (PBS) for one hour. After thawing, the specimens were affixed in the test frame (Instron 8875, Canton, MA) and subjected to a compressive preload of 300N for 30 minutes as a precaution against any superhydration effects.^{1,84} Throughout testing, the specimens were kept wrapped in PBS-soaked gauze to keep the IVDs hydrated. Samples were then subjected to a 500N load in either axial compression ($n=12$ specimens) or in anterior flexion (5° ; $n=14$ specimens).

A custom device (Figure 5.3) consisting of a 1.3-mm-diameter, high-pressure, needle-tip pressure transducer (Gaeltec Ltd., Dunvegan, Isle of Skye, UK) and a linear actuator equipped with a potentiometer (Firgelli Automations, Ferndale, WA, USA) to measure pressure and position within the disc, respectively. The pressure transducer was inserted entirely through the disc and then retracted at ~ 1 mm/s while the gauge pressure and position were sampled at a 1kHz rate (LabVIEW, National Instruments, Austin, TX).

The gauge-pressure data were amplified (linear gain: 105 V/V) and filtered with a 50Hz low-pass filter. Pressure measurements across mid-sagittal and mid-coronal lines were collected for both discs in the spine segment. Pressure measurements could not be made in the superior IVD in one specimen because bridging osteophytes prevented insertion of the transducer.

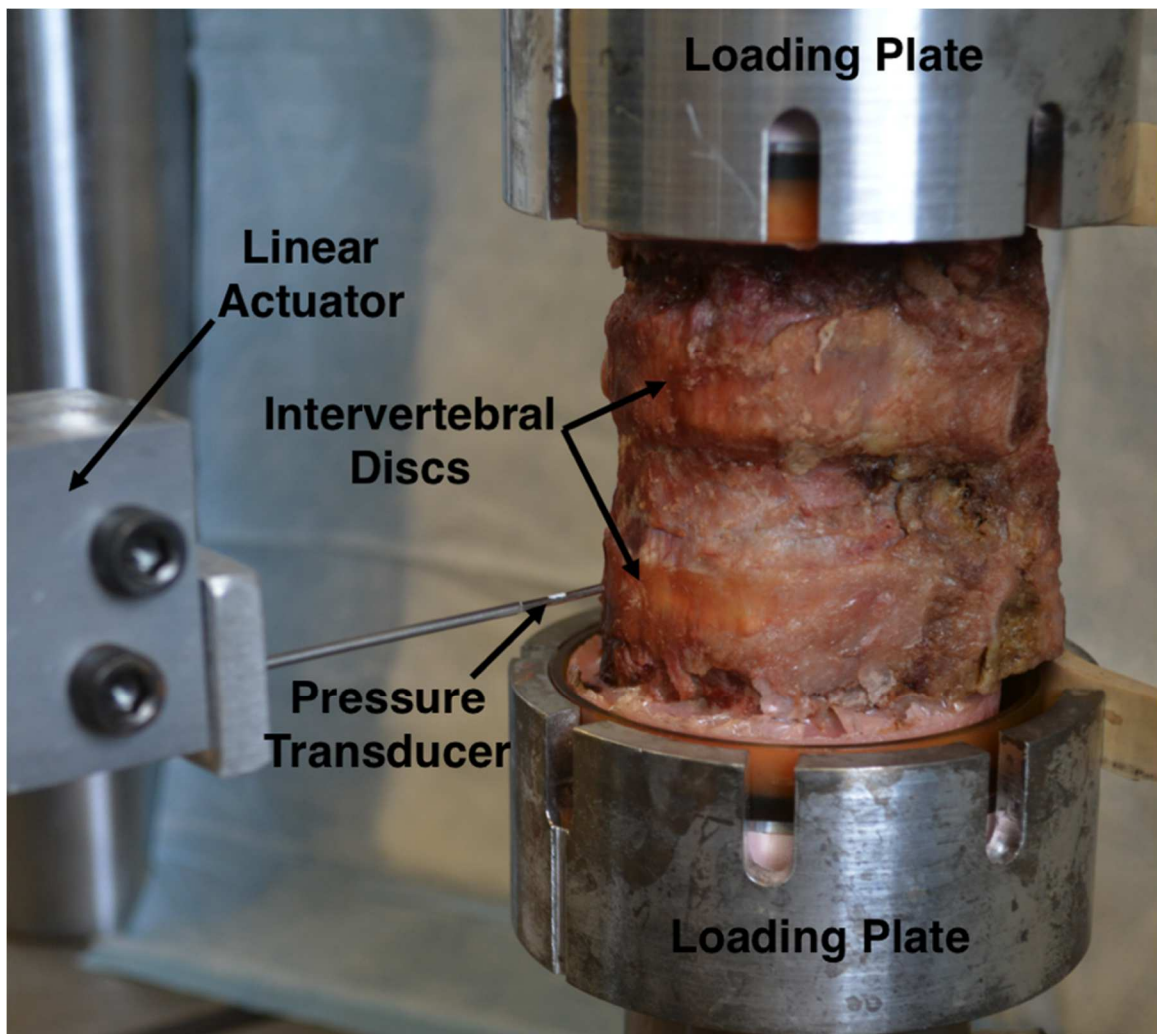


Figure 5.3 Photograph of spine segment with apparatus developed to obtain intradiscal pressure measurements; Image courtesy of Alex DelMonaco.

Boundary Conditions

Four sets of boundary conditions were used for each yield criterion and for each loading mode (Figures 5.4 – 5.5): 1) “Experimentally Matched” boundary conditions were DVC-measured displacements at the superior and inferior endplates; 2) “Idealized” boundary conditions were a uniform compressive displacement and a uniform angular displacement applied to the superior endplate for anterior flexion loading, and simply a uniform compressive displacement for axial compression loading; 3) “IVD-Generic” boundary conditions were based on intradiscal pressure measurements;²³ and 4) “IVD-Specific” boundary conditions were based on the measured intradiscal pressure profiles for only the IVDs with the same ALDI scoring as the IVDs adjacent to the vertebra being modeled. The intradiscal pressure profiles were resampled at fixed percentages of the width of the IVD, and then were normalized by a scaling factor such that the area underneath the profile was the same for every IVD of each loading mode. These normalized profiles were averaged for ALDI scores of 0 to 1, for scores of 2, and across all IVDs to obtain representative pressure distributions for each loading set for moderately healthy, degenerated, and generic (*i.e.*, all) IVDs. Mid-coronal profiles were modeled as an isosceles trapezoid based on pressure profiles observed experimentally and in FE simulations.^{23,56} The mid-coronal and mid-sagittal profiles were interpolated in the transverse plane of the IVD to produce an applied distributed load on the superior endplate. The total applied force matched the force developed when Experimentally Matched boundary conditions were applied. For 24 specimens, only small displacements (< 0.2 mm) were observed at the inferior endplate, thus the inferior endplate was fixed in

the Idealized, IVD-Generic, and IVD-Specific boundary conditions. The remaining 4 specimens (all loaded under axial compression) experienced failure in the inferior endplate and only small displacements (< 0.2 mm) were observed in the superior endplate. For the FE models of these four vertebrae, the superior endplate was fixed and the load was applied to the inferior endplate for the Idealized, IVD-Generic, and IVD-Specific boundary conditions.

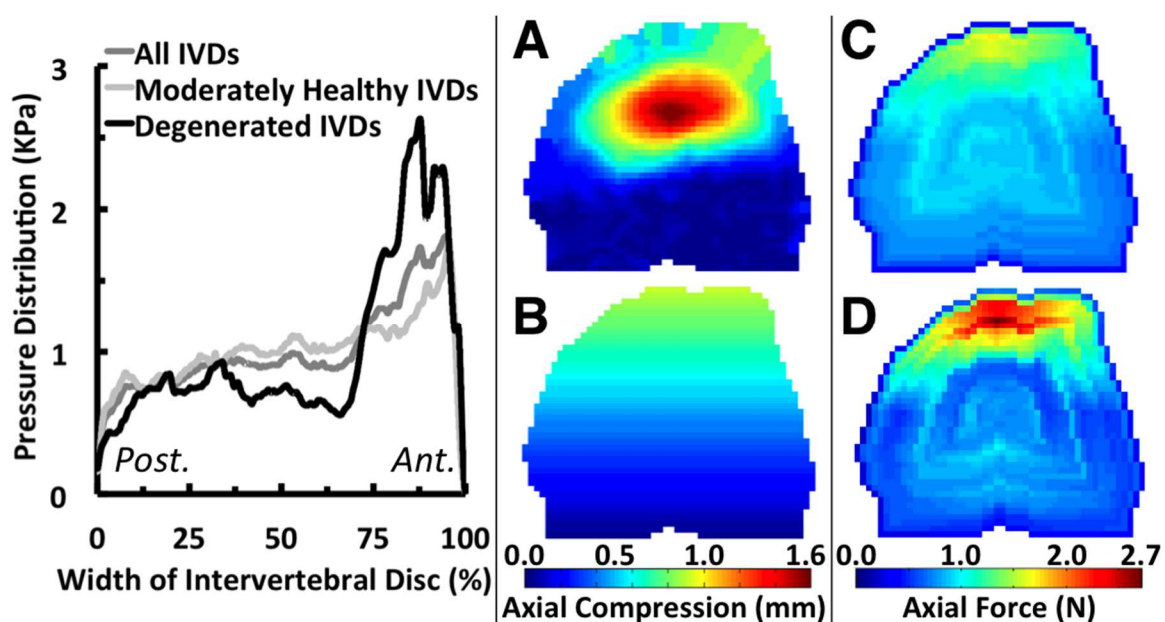


Figure 5.4 (Left) Measured mid-sagittal pressure profiles [7] averaged for moderately healthy (ALDI=0–1), degenerated (ALDI=2), and all (ALDI=0–2) IVDs loaded under anterior flexion. (Right) Color maps of the distributed load across the superior endplate for (A) Experimentally Matched, (B) Idealized, (C) IVD-Generic, and (D) IVD-Specific boundary conditions for the anterior flexion set.

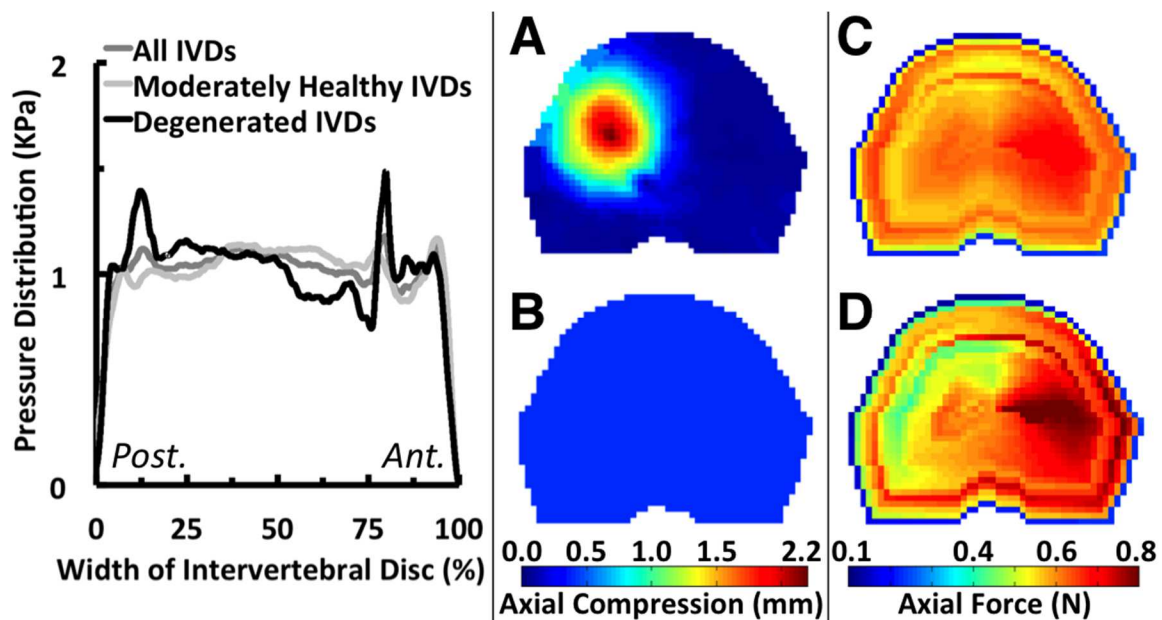


Figure 5.5 (Left) Measured mid-sagittal pressure profiles [7] averaged for moderately healthy (ALDI=0–1), degenerated (ALDI=2), and all (ALDI=0–2) IVDs loaded under axial compression. (Right) Color maps of the distributed load across the superior endplate for (A) Experimentally Matched, (B) Idealized, (C) IVD-Generic, and (D) IVD-Specific boundary conditions for the axial compression set.

Statistical Analyses

The experimentally measured displacements throughout the interior of T8 were regressed against the corresponding FE-computed displacements (JMP 11, SAS Institute, Cary, NC). For these comparisons, the FE nodal displacements were averaged over 2mm regions in order to match the spatial resolution of the DVC measurements, and points with measured displacements lower than the DVC detection limit (three times the standard deviation of the DVC displacement error (0.0556 mm)) were excluded.³⁵ The experimentally measured displacements and FE-computed displacements were transformed to fit a log-normal and a Johnson S_U distribution, respectively. Further, because the superior- and inferior-most layer of nodes of the DVC mesh were used to determine the Experimentally Matched boundary conditions, these nodes were excluded from all statistical analyses. Median displacement errors per specimen were compared using a repeated-measures ANOVA. In addition, displacement errors for the Experimentally Matched boundary conditions were compared for each yield criterion and loading mode using a repeated-measures ANOVA. FE-computed axial forces and moments were regressed against the corresponding measured values. The median percent errors between measured and FE-computed values of displacements were computed and compared via paired *t*-test. A significance level of 0.05 was used for all statistical analyses.

RESULTS

Anterior Flexion

All FE models captured some of the general, qualitative features of the deformation; however, the Idealized, IVD-Specific, and IVD-Generic models did not predict the localized deformation occurring superiorly (Figure 5.6). For the crushable foam FE models, R^2 values for the comparisons of measured and FE-computed displacements (Figure 5.7) in 13 specimens improved from 0.02–0.59 ($p = 0.0001$ – 0.088) for the case of Idealized boundary conditions to 0.19–0.78 (all $p < 0.0011$) for the case of Experimentally Matched boundary conditions (Figure 5.8). For the same 13 specimens, R^2 values for the case of IVD-Generic and IVD-Specific boundary conditions were 0.11–0.61 ($p = 0.0001$ – 0.0025) and 0.12–0.58 ($p = 0.0001$ – 0.0016), respectively. For the remaining specimen, displacements throughout the vertebral body remained small (≤ 0.3 mm) for the duration of loading, and poor agreement was observed for all cases ($R^2 < 0.03$, $p > 0.22$). Mean R^2 values for the regressions of FE-computed vs. measured displacements increased by 0.05 from Idealized to IVD-Generic, by 0.01 from IVD-Generic to IVD-Specific, and by 0.14 from IVD-Specific to Experimentally Matched boundary conditions.

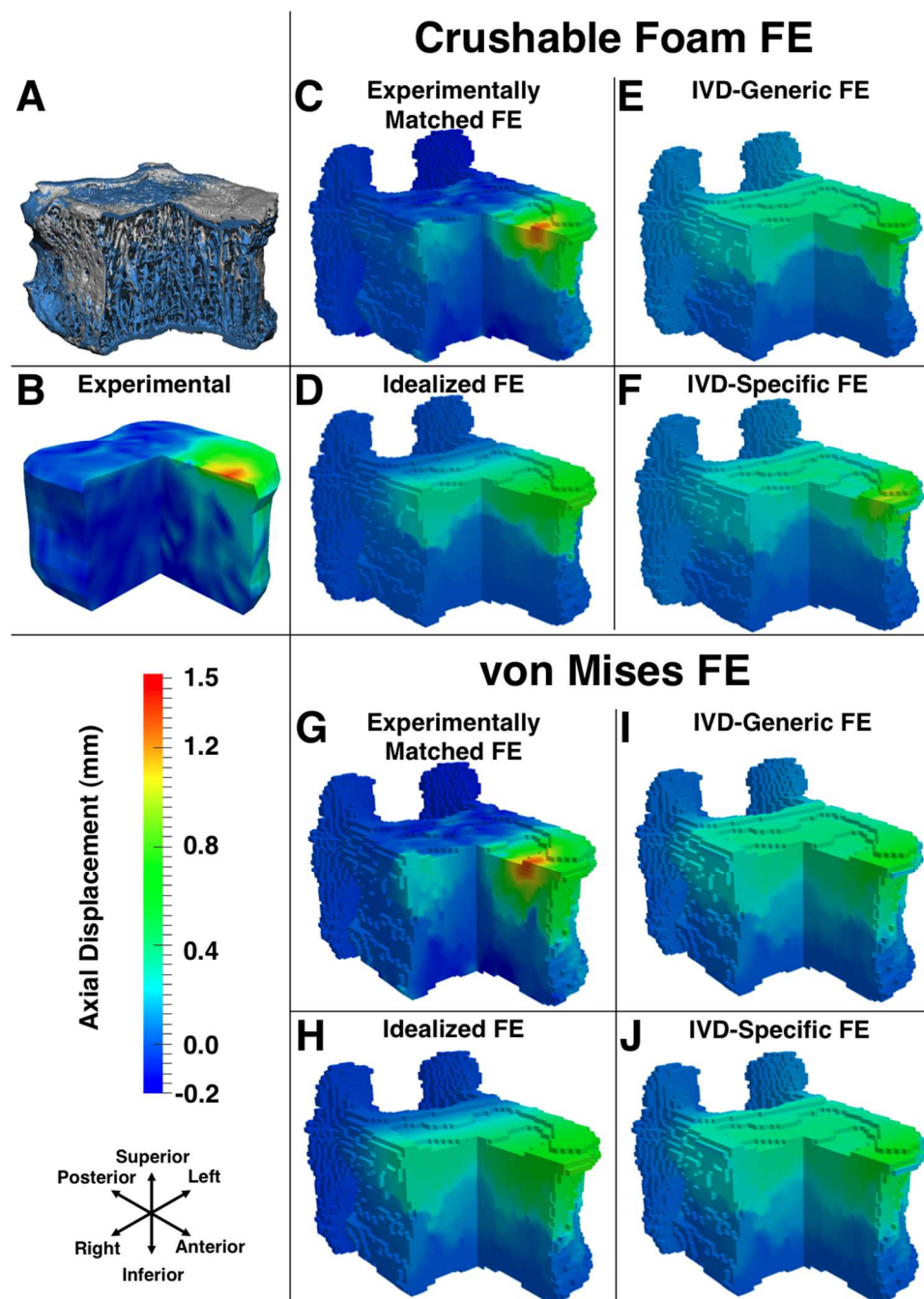


Figure 5.6 For anterior flexion: (A) Three-quarter section view of a representative T8 vertebral body before loading (gray) and at the load increment following peak of loading (blue); (B–J) Three-quarter section views of experimental and FE axial displacements (positive values are down-ward displacements) at the load increment following peak of loading for crushable foam (C–F) and von Mises (G–J) FE analyses.

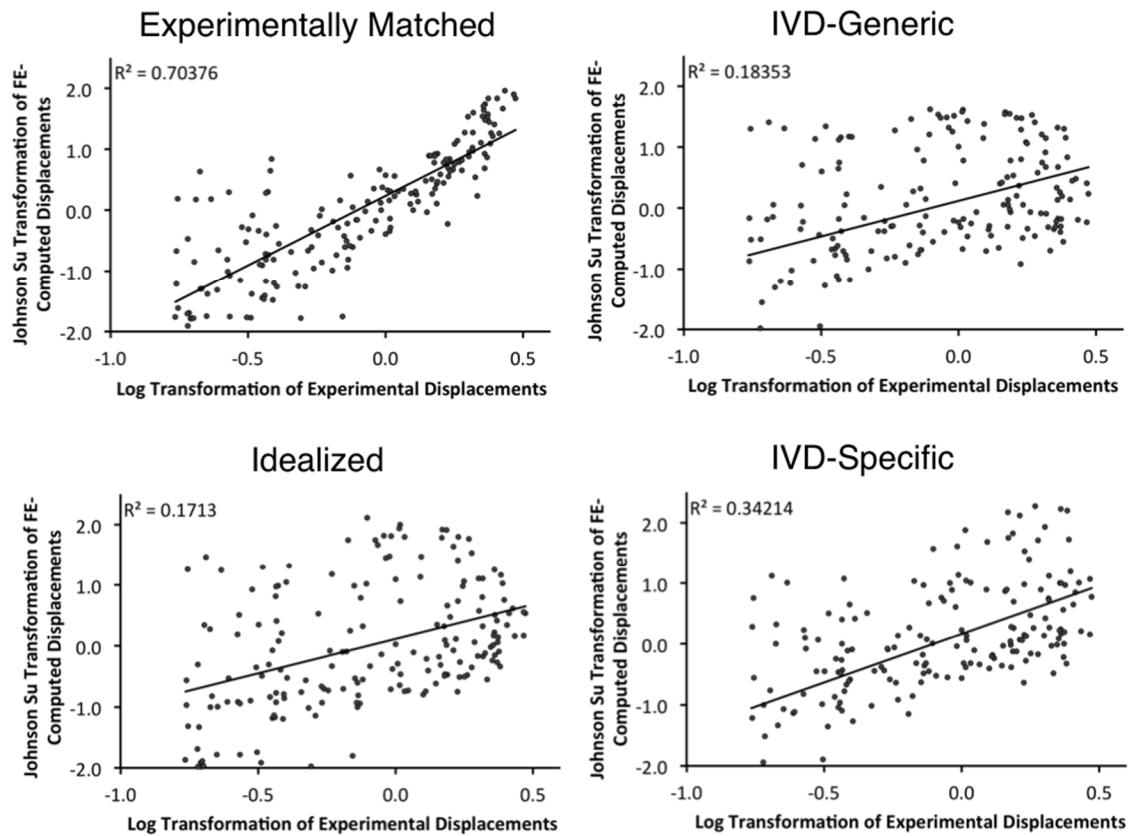


Figure 5.7 Linear regression performed on transformed experimental and FE-computed displacements for all boundary conditions from a representative specimen loaded under anterior flexion.

Comparable to the crushable foam FE models, the Idealized, IVD-Specific, and IVD-Generic models with von Mises yield criterion did not predict the localized deformation occurring superiorly. R^2 values for the comparisons of measured and FE-computed displacements in 13 specimens improved from 0.07–0.71 ($p = 0.0001$ – 0.002) for the case of Idealized boundary conditions to 0.13–0.84 (all $p < 0.0001$) for the case of Experimentally Matched boundary conditions (Figure 5.9). For the same 13 specimens, R^2 values for the case of IVD-Generic and IVD-Specific boundary conditions were 0.04–

0.64 ($p = 0.0001-0.019$) and 0.04–0.62 ($p = 0.0001 - 0.014$), respectively. For the remaining specimen, poor agreement was observed for all cases ($R^2 < 0.02$, $p > 0.14$). Mean R^2 values for the regressions of FE-computed vs. measured displacements increased by 0.02 from Idealized to IVD-Generic, by 0.04 from IVD-Generic to IVD-Specific, and by 0.16 from IVD-Specific to Experimentally Matched boundary conditions.

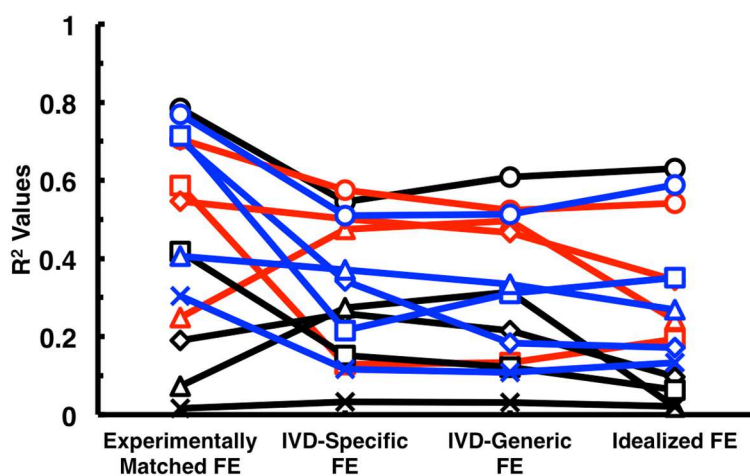


Figure 5.8 Crushable foam FE analyses: R^2 values for regressions of FE-computed vs. measured displacements of the anterior flexion set for all four boundary conditions. The color corresponds to ALDI score (blue=0, black=1, red=2), and for a given ALDI score each specimen is indicated with a different symbol.

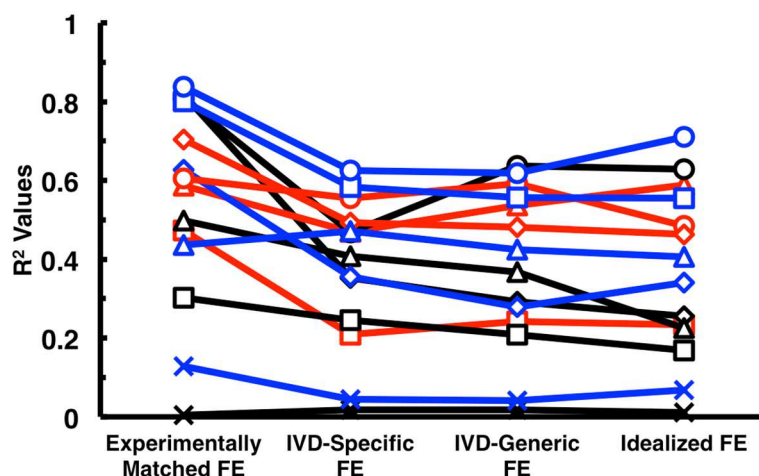


Figure 5.9 von Mises FE analyses: R^2 values for regressions of FE-computed vs. measured displacements of the anterior flexion set for all four boundary conditions. The color corresponds to ALDI score (blue=0, black=1, red=2), and for a given ALDI score each specimen is indicated with a different symbol.

Irrespective of the yield criterion used, the median percent error in displacement was higher for Idealized vs. Experimentally Matched boundary conditions ($p < 0.0029$; Figure 5.10). The median percent error was higher for IVD-Generic ($p < 0.037$) and IVD-Specific ($p < 0.038$) vs. Idealized for both yield criteria; however, when a Bonferroni correction²⁵ was applied to the six comparisons made among boundary conditions, the p -values of these comparisons were not below the new cutoff of $p < 0.0083$. For the von Mises models, median percent error was lower for Experimentally Matched boundary conditions compared to both IVD-Generic ($p < 0.0008$) and IVD-Specific ($p < 0.0004$) boundary conditions. For the remaining comparisons of median displacement errors, no other differences were found ($p > 0.50$).

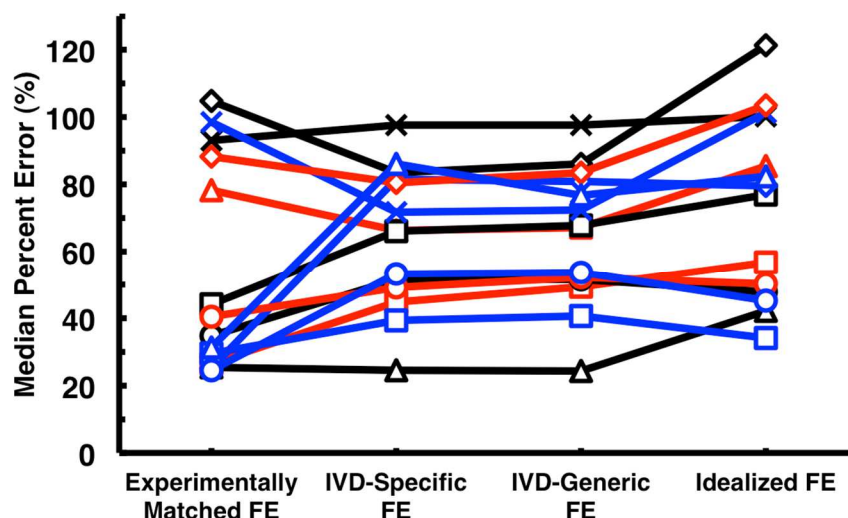


Figure 5.10 Median percent error for FE-computed axial displacements compared to experimental data using crushable foam FE yield criterion for specimens loaded under anterior flexion. The color corresponds to ALDI score (blue=0, black=1, red=2), and for a given ALDI score each specimen is indicated with a different symbol.

Irrespective of the yield criterion used, better agreement with measured values of ultimate force was also found with the Experimentally Matched boundary conditions when compared to the Idealized boundary conditions (Figure 5.11; CF: $R^2 = 0.58$ vs. 0.49, paired t -test p -value = 0.078 vs. 0.0004; VM: $R^2 = 0.40$ vs. 0.29, $p = 0.0149$ vs. 0.0279). For both boundary conditions, better agreement between experimental and FE-computed force was observed for the crushable foam models (Figure 5.11). However, no correlation was observed between the measured and FE-computed ultimate moments for either set of boundary conditions or yield criteria ($R^2 < 0.05$ (Figure 5.12); $p > 0.46$).

- Experimentally Matched von Mises FE:
 $R^2 = 0.40$; $p = 0.0149$
- Experimentally Matched Crushable Foam FE:
 $R^2 = 0.58$; $p = 0.0016$
- Idealized von Mises FE:
 $R^2 = 0.29$; $p = 0.0279$
- Idealized Crushable Foam FE:
 $R^2 = 0.49$; $p = 0.0050$

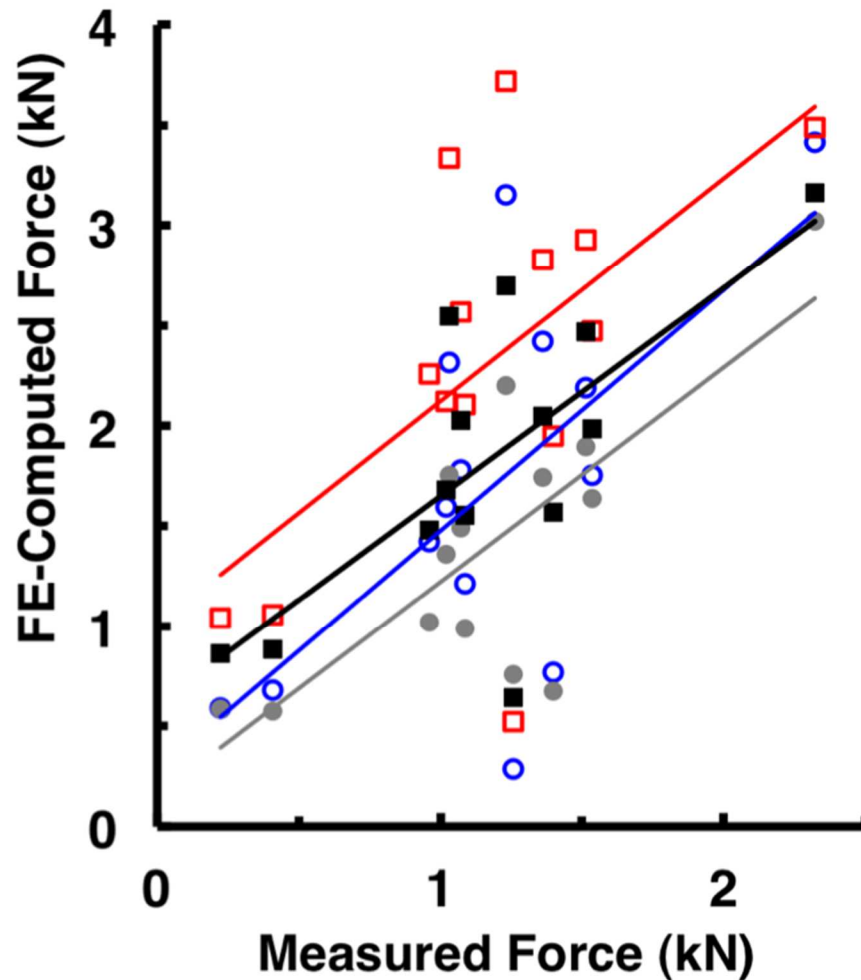


Figure 5.11 FE-computed axial force for each specimen loaded under anterior flexion plotted against experimental force

- Experimentally Matched von Mises FE:
 $R^2 = 0.05$; $p = 0.4602$
- Experimentally Matched Crushable Foam FE:
 $R^2 = 0.02$; $p = 0.5985$
- Idealized von Mises FE:
 $R^2 = 0.0004$; $p = 0.9476$
- Idealized Crushable Foam FE:
 $R^2 = 0.003$; $p = 0.8632$

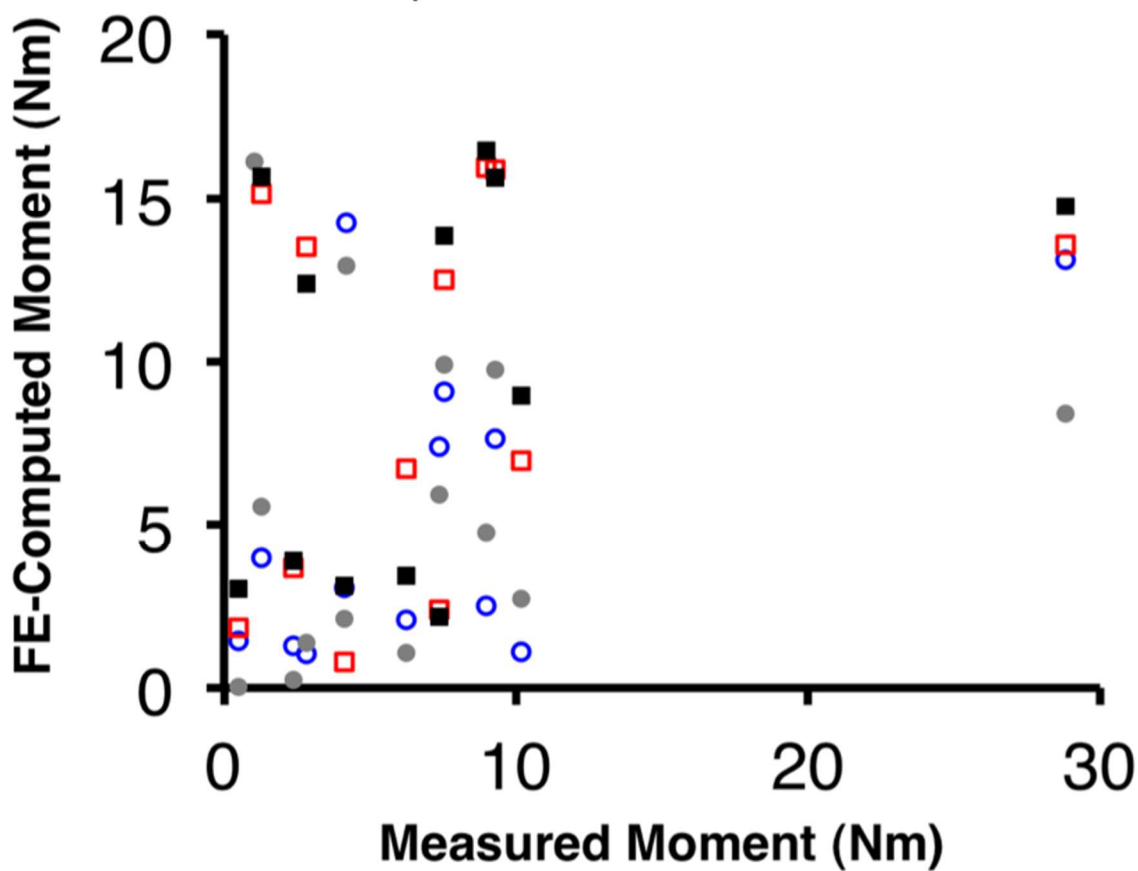


Figure 5.12 FE-computed moment for each specimen loaded under anterior flexion plotted against experimental anterior moment.

Axial Compression

In contrast to the anterior flexion set, the Idealized, IVD-Specific, and IVD-Generic models did not exhibit the qualitative features of deformation observed in the vertebrae loaded under axial compression (Figure 5.13). For the crushable foam FE models, R^2 values for the regressions of FE-computed vs. measured displacements improved from 0.02–0.39 ($p = 0.0001$ –0.17), 0.009–0.39 ($p = 0.0001$ –0.39), and 0.001–0.38 ($p = 0.0001$ –0.90) for the case of Idealized, IVD-Generic, and IVD-Specific boundary conditions, respectively, to 0.24–0.77 (all $p < 0.0001$) for the case of Experimentally Matched boundary conditions (Figure 5.14). For the von Mises FE models, R^2 values for the regressions of FE-computed vs. measured displacements improved from 0.08–0.44 ($p = 0.0001$ –0.0038), 0.05–0.38 ($p = 0.0001$ –0.0027), and 0.05–0.45 ($p = 0.0001$ –0.043) for the case of Idealized, IVD-Generic, and IVD-Specific boundary conditions, respectively, to 0.08–0.93 (all $p < 0.0001$) for the case of Experimentally Matched boundary conditions (Figure 5.15).

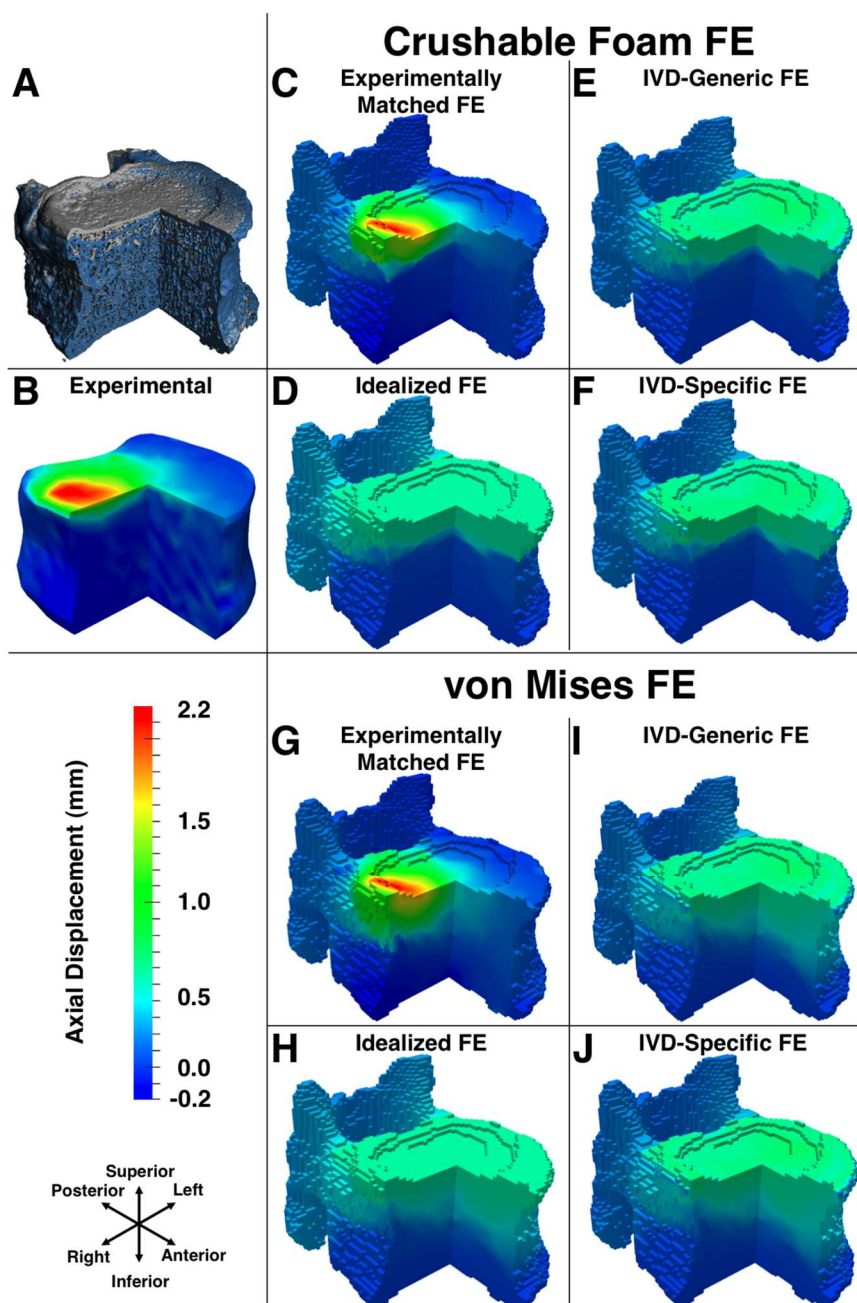


Figure 5.13 For axial compression: (A) Three-quarter section view of a representative T8 vertebral body before loading (gray) and at the load increment following peak of loading (blue); (B–J) Three-quarter section views of experimental and FE axial displacements (positive values are down-ward displacements) at the load increment following peak of loading for crushable foam (C–F) and von Mises (G–J) FE analyses.

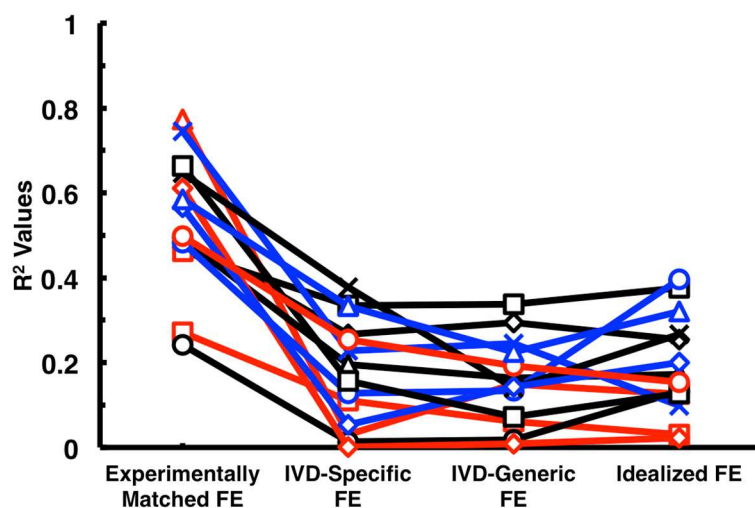


Figure 5.14 Crushable foam FE analyses: R^2 values for regressions of FE-computed vs. measured displacements of the axial compression set for all four boundary conditions. The color corresponds to ALDI score (blue=0, black=1, red=2), and for a given ALDI score each specimen is indicated with a different symbol.

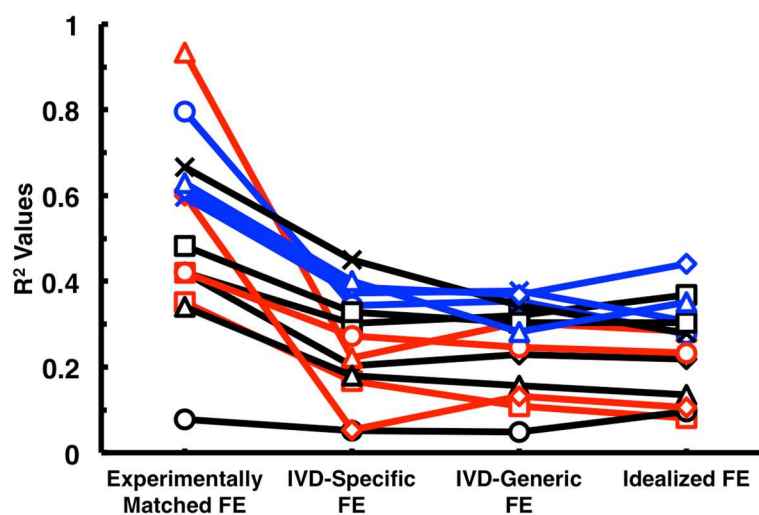


Figure 5.15 von Mises FE analyses: R^2 values for regressions of FE-computed vs. measured displacements of the axial compression set for all four boundary conditions. The color corresponds to ALDI score (blue=0, black=1, red=2), and for a given ALDI score each specimen is indicated with a different symbol.

Median percent error in axial displacement improved when Experimentally Matched boundary conditions were used compared to all other boundary conditions. Irrespective of the yield criterion used, the median percent error in displacement was higher for Idealized, IVD-Generic, and IVD-Specific boundary conditions when compared to Experimentally Matched boundary conditions ($p = 0.0004$ – 0.0077 ; Figure 5.16); no other differences were found ($p > 0.13$). In further contrast to the anterior flexion set, better agreement with measured values of ultimate force was found with the Idealized boundary conditions when compared to Experimentally Matched boundary conditions (Figure 5.17; CF: $R^2 = 0.62$ vs. 0.48 , paired t -test p -value = 0.0008 vs. 0.0063 ; VM: $R^2 = 0.53$ vs. 0.40 , $p = 0.003$ vs. 0.0144). As observed for the anterior flexion set, better agreement between experimental and FE-computed force was observed for the crushable foam models (Figure 5.11) than von Mises models.

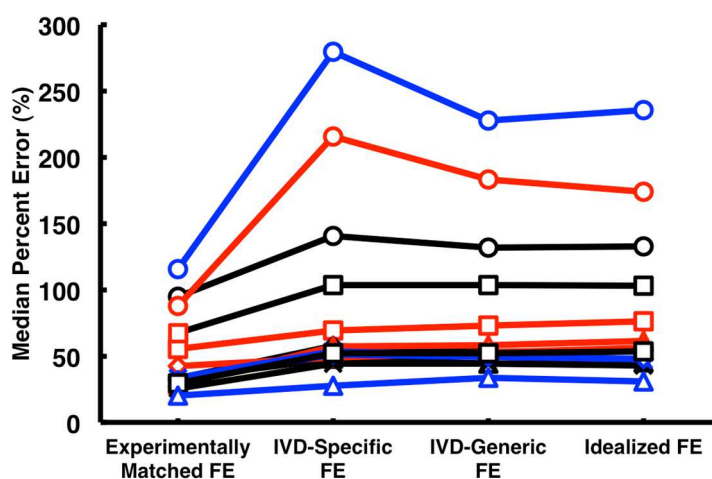


Figure 5.16 Median percent error for FE-computed axial displacements compared to experimental data using crushable foam FE yield criterion for specimens loaded under axial compression. The color corresponds to ALDI score (blue=0, black=1, red=2), and for a given ALDI score each specimen is indicated with a different symbol.

- Experimentally Matched von Mises FE:
 $R^2 = 0.40$; $p = 0.0144$
- Experimentally Matched Crushable Foam FE:
 $R^2 = 0.48$; $p = 0.0063$
- Idealized von Mises FE:
 $R^2 = 0.53$; $p = 0.0030$
- Idealized Crushable Foam FE:
 $R^2 = 0.62$; $p = 0.0008$

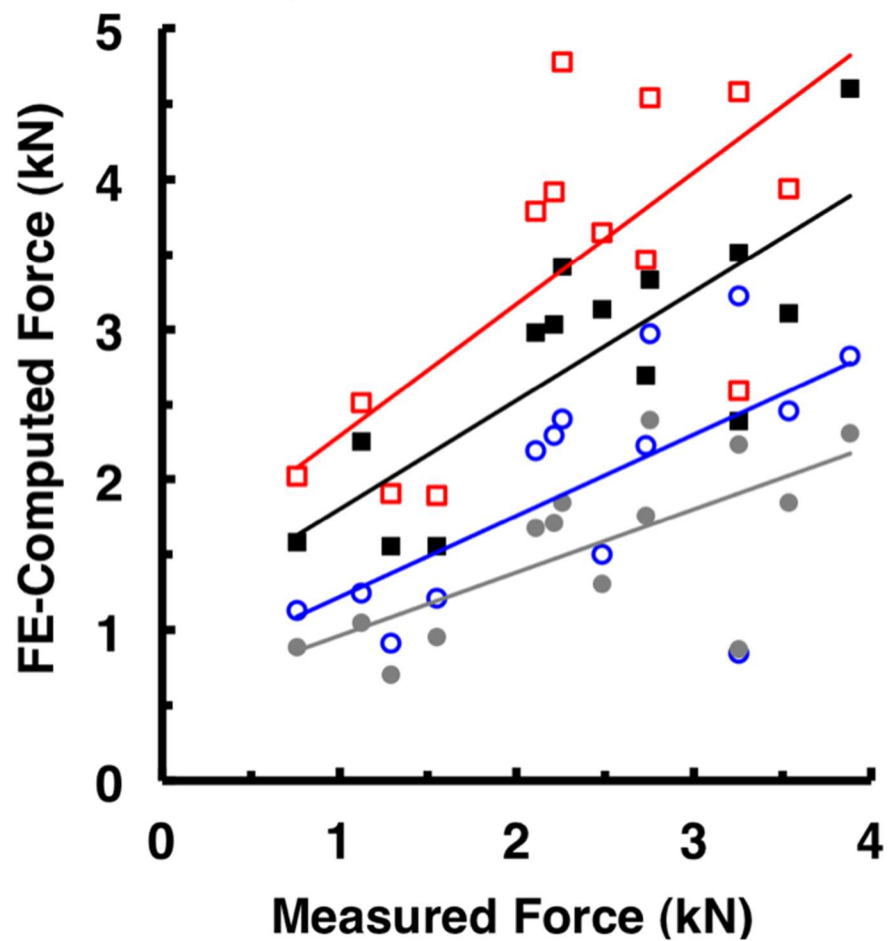


Figure 5.17 FE-computed axial force for each specimen loaded under axial compression plotted against experimental force.

Yield Criterion

The accuracy of the FE-computed displacement fields was affected by the yield criterion incorporated in the model. Irrespective of loading mode ($p = 0.5045$), errors between experimental and FE-computed displacements were lower in models with von Mises yield criterion compared to the crushable foam yield criterion ($p < 0.0001$), though substantial variation was observed between specimens ($p < 0.0001$). For all specimens grouped together, errors decreased from 0.266 ± 0.279 mm (mean \pm standard deviation) to 0.214 ± 0.199 (mean \pm standard deviation) for crushable foam and von Mises FE models, respectively, under axial compression and from 0.223 ± 0.293 (mean \pm standard deviation) to 0.201 ± 0.223 (mean \pm standard deviation) for crushable foam and von Mises FE models, respectively, under anterior flexion.

DISCUSSION

With QCT-based FE models showing tremendous promise for accurate predictions of clinical fracture risk,^{70,131} the overall goal of this study was to assess the accuracy of both vertebral strength and failure patterns in nonlinear FE analyses for spine segments loaded under both axial compression and anterior flexion. Although the loading applied to the T7–T9 spine segments was relatively simple, the T8 vertebral bodies within these segments experienced more complex loading conditions, which often featured large, localized displacements. Consequently, QCT-based FE simulations using idealized boundary conditions produced greater errors in predictions of vertebral deformation as compared to those that used experimentally matched boundary conditions. Under anterior flexion, the use of boundary conditions informed by measurements of

IVD pressure mitigated, but did not eliminate, this inaccuracy, regardless of whether boundary conditions used generic pressure measurements or pressure measurements from specimens of comparable disc health. FE analyses incorporating boundary conditions based on pressure profiles from IVDs of comparable disc health did not improve predictions of deformation over boundary conditions derived from generic pressure profiles. Overall, we found poor agreement between FE-predicted and experimentally observed failure patterns, indicating that further work is needed to accurately model the physiological loading conditions of the vertebra.

The crushable foam material model produced a thin band of deformation that more closely matched the failure pattern observed experimentally. Qualitatively, the crushable foam models produce a thin band of axial displacement localized in the superior half of the vertebra, often only near the superior endplate. The von Mises models predict a larger region of axial displacement with a smaller gradient at the boundary of the band of displacement. While many of the experimental displacements measured in the lower two-thirds of the vertebra fell within the expected DVC error range and thus were not used for comparison with FE-computed displacements, the crushable foam model appears to better predict the thin band with a relatively large gradient of displacement at the boundary of the band that is observed experimentally from both DVC displacements and μ CT images. However, FE analyses that incorporated transversely isotropic material properties and a yield criterion based only on the von Mises stress produced better predictions of displacements in regions featuring displacements higher than the DVC detection limit compared to FE analyses that incorporated a crushable foam yield

criterion. In addition, FE-computed vertebral strength was always higher for von Mises FE models compared to crushable foam FE models with comparable boundary conditions. Though better agreement was found between FE-computed and experimental strength for crushable foam models, a 1:1 ratio between FE-computed and experimental strength was not observed for crushable foam models under axial compression. While the crushable foam models produced failure patterns that better matched the general pattern observed experimentally, these models did not improve predictions of strength or predictions displacements in regions of large deformation over the von Mises models, suggesting further improvements to the material model—such as incorporating post-yield behavior that better matches experimental data—are warranted prior to use in clinical assessments.

A novel aspect of this study is that it incorporated both 3-D experimental measurements of deformation in the vertebra and experimental measurements of intradiscal pressure to define boundary conditions for FE models and, in the case of the former, to validate FE-computed displacements, allowing for direct comparisons of FE-computed vertebral strength *and* FE-computed displacements to experimental measurements. Another strength of this study is that it included non-invasive assessments of disc health as a consideration for boundary conditions. Patient-specific QCT-models have the promise of providing clinically feasible estimates of vertebral strength and risk of fracture; however, boundary conditions that consider patient-specific assessments of disc health and the mechanical implications have not previously been incorporated.

The performance of the boundary conditions based on intradiscal pressure profiles may to be impacted by the type of loading (*i.e.*, compression or bending loads) applied to the vertebra. The average intradiscal pressure profiles obtained under axial compression all featured—regardless of disc health—a relatively uniform pressure plateau and largely resembled the idealized boundary conditions (Figure 5.5). For the case of anterior flexion, the average pressure profiles were highly non-uniform when compared to idealized boundary conditions, featuring both a large peak at the anterior annulus and a plateau at the nucleus that varied with disc health (Figure 5.4). While the vertebral bodies loaded under anterior flexion featured localized displacements in a relatively compact area—located at or just anterior to the center of the superior endplate—the vertebral bodies loaded under axial compression featured localized displacements located in all broad regions of the endplate (Figure 4.13). For the case of anterior flexion (and in direct contrast to the axial compression case), the boundary conditions featuring intradiscal pressure profiles exhibited a localized increase in pressure at the anterior annulus, at or near the site of initial deflection of the vertebral endplate for all specimens. These results suggest that the stress concentrations observed in the anterior annulus of the IVD under moderate amounts of flexion should be incorporated into models loaded under anterior flexion.

FE-computed moments did not correlate with experimentally measured moments for specimens loaded under anterior flexion. The experimental procedure applied a relatively simple load distribution to the bone cement surrounding the superior endplate of T7, and the load distribution at the bone cement surrounding the inferior endplate of

T9 was determined with the calibration layer, detailed in Chapter Three. This load distribution was used to calculate the moment experienced by the spine segment. Under anterior flexion, IVDs have been observed to maintain a relatively uniform pressure across the nucleus,²³ indicating that the IVDs alter the applied load distribution. In addition, we found good agreement between FE-predicted and experimental strength, suggesting that, while the total load applied to the spine segment is conserved, the distribution of the load applied at T8 may be different than the distribution experienced by the calibration layer.

The limitations of this study relate to both the experimental and computational procedures. First, as with similar experimental procedures,^{48,54} the temporal resolution of deflection data was coarse, providing on average only 15 load increments and as few as four increments after initial deformation near the T8 endplates. The number of increments was limited because of long scan times and the perishable nature of the tissue. Ancillary time-course experiments of five L3 vertebrae scanned repeatedly over 72 hours showed no change in attenuation of the bone tissue ($p > 0.08$). In contrast, marrow attenuation decreased 27% on average over 72 hours in four of the specimens ($p < 0.01$). Thus, the current protocol is sufficient for quantifying bone parameters over several days, but the prospect of increasing the duration must be evaluated with caution. Second, static loads differ from the dynamic loading conditions experienced *in vivo*.⁴⁶ Sustained loading exudates fluid from the IVD, causing a drop in NP pressure that shifts the load distribution to the periphery that could confound any potential relationships between failure patterns and the health of the adjacent disc.⁸³ However, the ultimate loads

recorded in this study agree with those obtained from continuous loading of lumbar vertebral segments⁸² and prior studies of trabecular bone have also shown good correlation between mechanical properties obtained with continuous vs. step-wise loading.⁹¹ Third, T7 and T9 were partially cored and filled with bone cement to ensure that failure occurred in T8. While at least 5mm of trabecular bone were left intact near the endplates adjacent to T8, the bone cement would likely have some effect on the load distribution transmitted to T8. Furthermore, failure occurred in these regions of intact trabecular bone at T7 or T9 in six specimens. Despite failure initiating in T7, loading continued and the initiation of a fracture was observed in T8 for all specimens. Fourth, The IVD-Generic and IVD-Specific boundary conditions were created from intradiscal pressure profiles measured on T9–T11 and T10–T12 spine segments at lower forces than what was experienced by the T7–T9 spine segment at failure. The pressure measurements were scaled for the FE models to match the higher loads experienced by the FE simulations under the experimentally matched and idealized boundary conditions. While it may not be appropriate to scale pressure measurements at low loads to model pressure distributions at failure, Pollintine et al. found a linear relationship between IVD compressive stress and applied load¹⁰² and Dolan et al. have made comparisons of scaled intradiscal pressure across spine levels for vertebrae loaded under varying forces.²⁴ Fifth, in an effort to examine clinically feasible FE models, relatively coarse meshes were used that precluded modeling the cortical shell and endplates separately from the trabecular bone. Incorporating the endplates and cortical shell as a thin outer layer with high bone

density would provide a more physiologically relevant model and may improve prediction of failure patterns in the vertebral body.

While some studies have found strong correlations between predicted and experimental strength,^{11,18,20,21,97} these studies did not address the accuracy of FE-predicted failure patterns. Poor agreement was observed for some specimens between measured and FE-computed displacements even with Experimentally Matched boundary conditions and regardless of the yield criterion used, suggesting that further improvements in material modeling of the bone—such as incorporating post-yield behavior that better matches experimental data—are needed to produce accurate predictions of vertebral failure by QCT-based FE models. QCT-based FE analyses incorporating realistic loading at the vertebral endplates produced more accurate predictions of vertebral failure than the analyses using idealized loading. However, inaccuracies in the FE predictions remain, suggesting that further improvements to the FE models are required before widespread application in predictions of vertebral fracture.

CHAPTER SIX

CONCLUSIONS

The overall goal of this work was to define the failure processes involved in vertebral fractures and evaluate the accuracy of patient-specific FE models in simulating these processes. Mechanical testing of human spine segments, in conjunction with micro-computed tomography (μ CT), enabled the assessment of vertebral endplate deflection as the vertebra was loaded to failure under both axial compression and anterior flexion. Image-guided failure analysis provided 3-D experimental measurement of the displacement field throughout the vertebral body and at the endplates to quantify deformation patterns in the vertebra. These measured deformation fields were then used to determine the accuracy of patient-specific FE models built from quantitative computed tomography (QCT) scans. The accuracy of FE-predicted displacements was examined for boundary conditions representing very simple idealized loading as well as those corresponding to physiologically relevant load distributions experienced by the endplate. Further, non-invasive assessments of disc health were used to develop a representative pressure distribution experienced by the adjacent IVD for healthy and degenerated case as well as a generic case not informed by the health of the IVD. QCT-based FE models and non-invasive assessments of disc health are both clinically feasible approaches for estimating vertebral strength and fracture risk.

Failure of the vertebra was associated with sudden and permanent deflection in the endplate. Although large endplate deflection was initially localized, a marked increase in endplate deflection indicated that the mechanical competence of the vertebra had been severely compromised. Endplate deflection initially propagated preferentially to

regions of thinner and/or more porous endplate and less robust trabecular microstructure, and these associations with bone microstructure then waned as loading progressed. These results connote a biomechanical basis for clinical use of large endplate deflection as a characteristic of vertebral deformities and fracture,^{31,58,59} and that the failure mechanisms relate to anatomical features of the endplate, neighboring bone, and IVD.

The role of endplate deflection in vertebral fractures for flexion loading was also examined, but only after surmounting an additional technical challenge. Spatial constraints in the μ CT equipment precluded the use of commercially available multi-axial load cells that would measure the loads and moments experienced by the spine segment under anterior flexion. To measure the non-uniform distribution of force along the inferior surface of the thoracic spine segment, a calibration layer was employed to operate as a multi-axial load cell. The polyurethane calibration layer deformed as load was applied through the spine segment and bone cement. The load distribution across the top surface of the calibration layer, and hence across the bottom surface of the spine segment, could be inferred from measurement of the deformation of the calibration layer and knowledge of the material properties of the polyurethane using a validated FE model.

The development of the calibration layer and the corresponding FE model facilitated the mechanical testing of thoracic spine segments under anterior flexion with μ CT. Under a moderate amount of anterior flexion, initial damage of the vertebral body tended to occur at or near the central endplate and, at least within the temporal resolution of this study, simultaneously at the anterior cortex near the central endplate. Damage then progressed anteriorly and inferiorly, while the posterior half of the vertebra remained

intact, leading to a pattern of wedge fracture. As damage progressed, endplate deflection propagated preferentially to regions with lower endplate volume fraction and to regions overlying less robust trabecular bone. Upon a marked increase in endplate deflection, the ability of the vertebral body to support anterior flexion had been compromised, even before the development of a clinical wedge fracture pattern. After the peak of loading, the anterior moment was markedly reduced while the axial load may or may not have declined. Damage to the anterior endplate and cortex may not markedly affect the ability of the vertebra to carry axial loads but may inhibit the vertebra's ability to support anterior bending moments.

Nonlinear FE models were developed from QCT images, and the displacement fields obtained from DVC were used to assess the accuracy of FE-predicted failure patterns. All FE models captured some of the general, qualitative features of the deformation; however, the models with idealized and intradiscal pressure-based boundary conditions did not predict the localized deformation occurring superiorly. FE simulations using idealized boundary conditions produced greater errors in predictions of vertebral deformation as compared to those that used experimentally matched boundary conditions. FE analyses incorporating boundary conditions based on pressure profiles from IVDs of comparable disc health did not improve predictions of deformation over boundary conditions derived from generic pressure profiles. Under anterior flexion, the use of boundary conditions informed by measurements of IVD pressure mitigated, but did not eliminate, this inaccuracy. The stress concentrations observed in the anterior annulus of the IVD under moderate amounts of flexion should be incorporated into models loaded

under anterior flexion. Under axial compression, the boundary conditions based on average intradiscal pressure profiles all featured—regardless of disc health—a relatively uniform pressure plateau and largely resembled the idealized boundary conditions. Thus, FE analyses using either idealized or intradiscal pressure-based boundary conditions produced greater errors in predictions of displacement fields than the experimentally matched boundary conditions.

The outcomes of this research demonstrate that endplate deflection is a defining feature of vertebral failure for both simple compression loads and a combination of compression and bending loads. While a sudden increase in endplate deflection indicated that the mechanical competence had been compromised for vertebrae under both loading modes, vertebrae under anterior bending loads experienced a reduced capability to support forward bending moments, shifting the load to the posterior elements and the posterior half of the vertebral body. Using the classifications for clinical fractures established by Genant et al. (Figure 1.6)³⁴, the minimum standard for a wedge fracture was more commonly observed in specimens loaded under anterior flexion than axial compression. The minimum standard for a biconcave fracture was commonly observed for specimens loaded under both anterior flexion and axial compression, suggesting that deflection in the central endplate is a defining feature of vertebral fracture regardless of the applied loading. Clinical observation of endplate deflection, even before traditional standards of fracture³⁴ have been met, can be used to indicate that the mechanical competence of the vertebra has been compromised, even though much of the vertebra may remain undeformed.

The localized deformations in the endplates suggest that the loading experienced by the vertebra is highly non-uniform, and FE analyses that incorporate these localized deformations into the boundary conditions, though clinically infeasible, are currently the gold standard for obtaining accurate predictions of deformation throughout the vertebral body. The stress concentrations observed in the anterior annulus of the IVD under moderate amounts of flexion²³ should be incorporated into models loaded under anterior flexion for a clinically feasible boundary condition; however incorporating intradiscal pressure measurements into the boundary conditions for axial compression did not improve the performance of the FE simulation over idealized boundary conditions. FE analyses with boundary conditions based on intradiscal pressure profiles applied a relatively uniform load distribution and, unsurprisingly, could not model the localized regions of damage observed experimentally. Further improvements in material modeling of the bone are needed to produce accurate predictions of vertebral failure by QCT-based FE models, possibly by developing of a material model that could better emulate the localized, buckling-type behavior and subsequent propagation of damage from the site of initial deformation that was observed experimentally.

FUTURE WORK

This work elucidated the relationship between endplate deflection and vertebral failure as well as the effect of physiologically relevant loading conditions on FE simulations of vertebral failure. During the course of this study, several new questions arose that may be answered by future investigations, including:

- How would FE simulations with boundary conditions based on intradiscal pressures perform when a different scoring system is used to identify healthy and degenerated IVDs? This study utilized the QCT images already available to develop the “apparent loss of disc integrity” (ALDI) scoring system; however, soft tissue features low levels of attenuation in QCT images and variations in soft tissue are difficult to identify. Another noninvasive assessment of IVD health has been established using magnetic resonance imaging¹⁰⁰ (MRI) to visualize subtle distinctions in the water and GAG content of the IVD. This technique would not be optimal in a clinical setting, however, because it would require both MRI and QCT images to develop FE models with noninvasive assessments of IVD health.
- What improvements could be made to the material model to accurately predict the failure patterns of the vertebral body? Despite incorporating physiological relevant boundary conditions to the FE simulations, FE-computed displacements with such boundary conditions were in relatively poor agreement with experimental displacements when compared to experimentally matched boundary conditions. Without the experimentally matched boundary conditions, no FE simulations could match the deformation pattern observed experimentally that featured a single, localized, region of deformation at the endplate. The current material models fail to account for the apparent buckling behavior occurring with the sub-endplate trabecular bone at the site of initial endplate deflection.
- How can a broader assessment of *in-vivo* conditions improve how vertebral loading is incorporated, both in biomechanical experiments and clinically feasible

FE simulations? In addition to geometry, morphology, and the interaction between the vertebra and adjacent IVDs, understanding the contribution of spinal curvature and zygapophysial joints on vertebral loading in each patient and how degeneration affects these interactions. Further, the presence of large osteophytes have an impact on vertebral loading, but this impact is largely avoided in mechanical tests and including the role of large osteophytes would provide a more clinically relevant understanding of vertebral loading.

- How can clinical assessments of sub-endplate trabecular bone quality, IVD degeneration, and vertebral fracture be combined to develop new indicators of fracture risk? Longitudinal and cross-sectional studies of QCT images from a population subset may provide new insights to assessing fracture risk by combining analyses of the heterogeneity of bone mineral density with assessments of IVD health and spatial patterns of intradiscal pressure.

BIBLIOGRAPHY

1. Adams, MA, Freeman, BJ, Morrison, HP, et al. 2000. Mechanical initiation of intervertebral disc degeneration. *Spine* 25: 1625–1636.
2. Adams, MA, McNally, DS, Dolan, P. 1996. 'Stress' distributions inside intervertebral discs. The effects of age and degeneration. *The Journal of Bone and Joint Surgery. British Volume* 78: 965–972.
3. Adams, MA, Pollintine, P, Tobias, JH, et al. 2006. Intervertebral disc degeneration can predispose to anterior vertebral fractures in the thoracolumbar spine. *Journal of Bone and Mineral Research* 21: 1409–1416.
4. Battie, MC, Videman, T, Parent, E. 2004. Lumbar disc degeneration: Epidemiology and genetic influences. *Spine* 29: 2679–2690.
5. Bay, BK, Smith, TS, Fyhrie, DP, Saad, M. 1999. Digital volume correlation: Three-dimensional strain mapping using x-ray tomography. *Experimental Mechanics* 39: 217–226.
6. Boos, N, Weissbach, S, Rohrbach, H, et al. 2002. Classification of age-related changes in lumbar intervertebral discs: 2002 volvo award in basic science. *Spine* 27: 2631–2644.
7. Braithwaite, I, White, J, Saifuddin, A, et al. 1998. Vertebral end-plate (modic) changes on lumbar spine mri: Correlation with pain reproduction at lumbar discography. *European Spine Journal* 7: 363–368.
8. Brinckmann, P, Frobin, W, Hierholzer, E, Horst, M. 1983. Deformation of the vertebral end-plate under axial loading of the spine. *Spine* 8: 851–856.

9. Buckley, JM, Cheng, L, Loo, K, et al. 2007. Quantitative computed tomography-based predictions of vertebral strength in anterior bending. *Spine* 32: 1019–1027.
10. Buckley, JM, Kuo, CC, Cheng, LC, et al. 2009. Relative strength of thoracic vertebrae in axial compression versus flexion. *The Spine Journal* 9: 478–485.
11. Buckley, JM, Loo, K, Motherway, J. 2007. Comparison of quantitative computed tomography-based measures in predicting vertebral compressive strength. *Bone* 40: 767–774.
12. Buckwalter, JA. 1995. Aging and degeneration of the human intervertebral disc. *Spine* 20: 1307–1314.
13. Burge, R, Dawson-Hughes, B, Solomon, DH, et al. 2007. Incidence and economic burden of osteoporosis-related fractures in the united states, 2005–2025. *Journal of Bone and Mineral Research* 22: 465–475.
14. Burger, H, Van Daele, PL, Grashuis, K, et al. 1997. Vertebral deformities and functional impairment in men and women. *Journal of Bone and Mineral Research* 12: 152–157.
15. Cauley, JA, Thompson, DE, Ensrud, KC, et al. 2000. Risk of mortality following clinical fractures. *Osteoporosis International* 11: 556–561.
16. Cheng, XG, Nicholson, PH, Boonen, S, et al. 1997. Prediction of vertebral strength in vitro by spinal bone densitometry and calcaneal ultrasound. *Journal of Bone and Mineral Research* 12: 1721–1728.

17. Chevalier, Y, Pahr, D, Zysset, PK. 2009. The role of cortical shell and trabecular fabric in finite element analysis of the human vertebral body. *Journal of Biomechanical Engineering* 131: 111003.
18. Crawford, RP, Cann, CE, Keaveny, TM. 2003. Finite element models predict in vitro vertebral body compressive strength better than quantitative computed tomography. *Bone* 33: 744–750.
19. Crawford, RP, Keaveny, TM. 2004. Relationship between axial and bending behaviors of the human thoracolumbar vertebra. *Spine* 29: 2248–2255.
20. Dall'Ara, E, Pahr, D, Varga, P, et al. 2012. Qct-based finite element models predict human vertebral strength in vitro significantly better than simulated dexa. *Osteoporosis International* 23: 563–572.
21. Dall'Ara, E, Schmidt, R, Pahr, D, et al. 2010. A nonlinear finite element model validation study based on a novel experimental technique for inducing anterior wedge-shape fractures in human vertebral bodies in vitro. *Journal of Biomechanics* 43: 2374–2380.
22. de Schepper, EI, Damen, J, van Meurs, JB, et al. 2010. The association between lumbar disc degeneration and low back pain: The influence of age, gender, and individual radiographic features. *Spine* 35: 531–536.
23. DelMonaco, AM, Jackman, TM, Fein, PM, et al., 2015. Quantifying the spatial distribution of intradiscal pressure and its assessment via non-invasive estimates of intervertebral disc degeneration. In, 61st Annual Meeting of the Orthopaedic Research Society.

24. Dolan, P, Luo, J, Pollintine, P, et al. 2013. Intervertebral disc decompression following endplate damage: Implications for disc degeneration depend on spinal level and age. *Spine* 38: 1473–1481.
25. Dunn, OJ. 1959. Estimation of the medians for dependent variables. *The Annals of Mathematical Statistics* 30: 192–197.
26. Eastell, R, Cedel, SL, Wahner, HW, et al. 1991. Classification of vertebral fractures. *Journal of Bone and Mineral Research* 6: 207–215.
27. Eisenberg, SR, Grodzinsky, AJ. 1985. Swelling of articular cartilage and other connective tissues: Electromechanochemical forces. *Journal of Orthopaedic Research* 3: 148–159.
28. Emch, TM, Modic, MT. 2011. Imaging of lumbar degenerative disk disease: History and current state. *Skeletal Radiology* 40: 1175–1189.
29. Eswaran, SK, Gupta, A, Adams, MF, Keaveny, TM. 2006. Cortical and trabecular load sharing in the human vertebral body. *Journal of Bone and Mineral Research* 21: 307–314.
30. Faulkner, KG, Gluer, CC, Majumdar, S, et al. 1991. Noninvasive measurements of bone mass, structure, and strength: Current methods and experimental techniques. *American Journal of Roentgenology* 157: 1229–1237.
31. Ferrar, L, Jiang, G, Schousboe, JT, et al. 2008. Algorithm-based qualitative and semiquantitative identification of prevalent vertebral fracture: Agreement between different readers, imaging modalities, and diagnostic approaches. *Journal of Bone and Mineral Research* 23: 417–424.

32. Fields, AJ, Lee, GL, Keaveny, TM. 2010. Mechanisms of initial endplate failure in the human vertebral body. *Journal of Biomechanics* 43: 3126–3131.
33. Fujiwara, S, Kasagi, F, Yamada, M, Kodama, K. 1997. Risk factors for hip fracture in a japanese cohort. *Journal of Bone and Mineral Research* 12: 998–1004.
34. Genant, HK, Wu, CY, van Kuijk, C, Nevitt, MC. 1993. Vertebral fracture assessment using a semiquantitative technique. *Journal of Bone and Mineral Research* 8: 1137–1148.
35. Ghosh, R, Gupta, S, Dickinson, A, Browne, M. 2012. Experimental validation of finite element models of intact and implanted composite hemipelvises using digital image correlation. *Journal of Biomechanical Engineering* 134: 081003.
36. Giambini, H, Khosla, S, Nassr, A, et al. 2013. Longitudinal changes in lumbar bone mineral density distribution may increase the risk of wedge fractures. *Clinical Biomechanics* 28: 10–14.
37. Granhed, H, Jonson, R, Hansson, T. 1989. Mineral content and strength of lumbar vertebrae. A cadaver study. *Acta Orthopaedica Scandinavica* 60: 105–109.
38. Greep, RO, Fischer, CJ, Morse, A. 1947. Histochemical demonstration of alkaline phosphatase in decalcified dental and osseous tissues. *Science* 105: 666.
39. Hardy, WG, Lissner, HR, Webster, JE, Gurdjian, ES. 1958. Repeated loading tests of the lumbar spine; a preliminary report. *Surgical Forum* 9: 690–695.
40. Hasserijs, R, Johnell, O, Nilsson, BE, et al. 2003. Hip fracture patients have more vertebral deformities than subjects in population-based studies. *Bone* 32: 180–184.

41. Hasserijs, R, Redlund-Johnell, I, Mellstrom, D, et al. 2001. Vertebral deformation in urban swedish men and women: Prevalence based on 797 subjects. *Acta Orthopaedica Scandinavica* 72: 273–278.
42. Holmes, AD, Hukins, DW, Freemont, AJ. 1993. End-plate displacement during compression of lumbar vertebra-disc-vertebra segments and the mechanism of failure. *Spine* 18: 128–135.
43. Homminga, J, Van-Rietbergen, B, Lochmuller, EM, et al. 2004. The osteoporotic vertebral structure is well adapted to the loads of daily life, but not to infrequent "error" loads. *Bone* 34: 510–516.
44. Homminga, J, Weinans, H, Gowin, W, et al. 2001. Osteoporosis changes the amount of vertebral trabecular bone at risk of fracture but not the vertebral load distribution. *Spine* 26: 1555–1561.
45. Hulme, PA, Boyd, SK, Ferguson, SJ. 2007. Regional variation in vertebral bone morphology and its contribution to vertebral fracture strength. *Bone* 41: 946–957.
46. Hulme, PA, Ferguson, SJ, Boyd, SK. 2008. Determination of vertebral endplate deformation under load using micro-computed tomography. *Journal of Biomechanics* 41: 78–85.
47. Hussein, AI, 2013. 3-d visualization and prediction of spine fractures under axial loading. Unpublished doctoral dissertation, Boston University.
48. Hussein, AI, Barbone, PE, Morgan, EF. 2012. Digital volume correlation for study of the mechanics of whole bones. *Procedia IUTAM* 4: 116–125.

49. Hussein, AI, Jackman, TM, Morgan, SR, et al. 2013. The intravertebral distribution of bone density: Correspondence to intervertebral disc health and implications for vertebral strength. *Osteoporosis International* 24: 3021–3030.
50. Hussein, AI, Morgan, EF. 2013. The effect of intravertebral heterogeneity in microstructure on vertebral strength and failure patterns. *Osteoporosis International* 24: 979–989.
51. Hussein, AI, Unnikrishnan, GU, Barest, GD, Morgan, EF, 2013. Accuracy of qct-based finite element models of the vertebra. In Annual Meeting of the American Society for Bone and Mineral Research.
52. Imai, K, Ohnishi, I, Bessho, M, Nakamura, K. 2006. Nonlinear finite element model predicts vertebral bone strength and fracture site. *Spine* 31: 1789–1794.
53. Inoue, H. 1981. Three-dimensional architecture of lumbar intervertebral discs. *Spine* 6: 139–146.
54. Jackman, TM, Hussein, AI, Adams, AM, et al. 2014. Endplate deflection is a defining feature of vertebral fracture and is associated with properties of the underlying trabecular bone. *Journal of Orthopaedic Research* 32: 880–886.
55. Jackson, AR, Yuan, TY, Huang, CY, Gu, WY. 2009. A conductivity approach to measuring fixed charge density in intervertebral disc tissue. *Annals of Biomedical Engineering* 37: 2566–2573.
56. Jacobs, NT, Cortes, DH, Peloquin, JM, et al. 2014. Validation and application of an intervertebral disc finite element model utilizing independently constructed tissue-

- level constitutive formulations that are nonlinear, anisotropic, and time-dependent. *Journal of Biomechanics* 47: 2540–2546.
57. Jelsma, RK, Kirsch, PT, Rice, JF, Jelsma, LF. 1982. The radiographic description of thoracolumbar fractures. *Surgical Neurology* 18: 230–236.
58. Jiang, G, Eastell, R, Barrington, NA, Ferrar, L. 2004. Comparison of methods for the visual identification of prevalent vertebral fracture in osteoporosis. *Osteoporosis International* 15: 887–896.
59. Jiang, G, Luo, J, Pollintine, P, et al. 2010. Vertebral fractures in the elderly may not always be "osteoporotic". *Bone* 47: 111–116.
60. Johannessen, W, Elliott, DM. 2005. Effects of degeneration on the biphasic material properties of human nucleus pulposus in confined compression. *Spine* 30: E724–729.
61. Jones, AC, Wilcox, RK. 2008. Finite element analysis of the spine: Towards a framework of verification, validation and sensitivity analysis. *Medical Engineering & Physics* 30: 1287–1304.
62. Jones, G, Nguyen, T, Sambrook, PN, et al. 1994. Symptomatic fracture incidence in elderly men and women: The dubbo osteoporosis epidemiology study (does). *Osteoporosis International* 4: 277–282.
63. Kado, DM, Duong, T, Stone, KL, et al. 2003. Incident vertebral fractures and mortality in older women: A prospective study. *Osteoporosis International* 14: 589–594.

64. Kanis, JA, Johnell, O, Oden, A, et al. 2002. Ten-year risk of osteoporotic fracture and the effect of risk factors on screening strategies. *Bone* 30: 251–258.
65. Keaveny, TM. 2010. Biomechanical computed tomography-noninvasive bone strength analysis using clinical computed tomography scans. *Annals of the New York Academy of Sciences* 1192: 57–65.
66. Keller, TS, Hansson, TH, Abram, AC, et al. 1989. Regional variations in the compressive properties of lumbar vertebral trabeculae: Effects of disc degeneration. *Spine* 14: 1012–1019.
67. Keller, TS, Ziv, I, Moeljanto, E, Spengler, DM. 1993. Interdependence of lumbar disc and subdiscal bone properties: A report of the normal and degenerated spine. *Journal of Spinal Disorders* 6: 106–113.
68. Kinzl, M, Wolfram, U, Pahr, DH. 2013. Identification of a crushable foam material model and application to strength and damage prediction of human femur and vertebral body. *Journal of the Mechanical Behavior of Biomedical Materials* 26: 136–147.
69. Kobayashi, S, Baba, H, Takeno, K, et al. 2008. Fine structure of cartilage canal and vascular buds in the rabbit vertebral endplate. *Journal of Neurosurgery: Spine* 9: 96–103.
70. Kopperdahl, DL, Aspelund, T, Hoffmann, PF, et al. 2014. Assessment of incident spine and hip fractures in women and men using finite element analysis of ct scans. *Journal of Bone and Mineral Research* 29: 570–580.

71. Kopperdahl, DL, Morgan, EF, Keaveny, TM. 2002. Quantitative computed tomography estimates of the mechanical properties of human vertebral trabecular bone. *Journal of Orthopaedic Research* 20: 801–805.
72. Kurowski, P, Kubo, A. 1986. The relationship of degeneration of the intervertebral disc to mechanical loading conditions on lumbar vertebrae. *Spine* 11: 726–731.
73. Lane, NE, Nevitt, MC, Genant, HK, Hochberg, MC. 1993. Reliability of new indices of radiographic osteoarthritis of the hand and hip and lumbar disc degeneration. *The Journal of Rheumatology* 20: 1911–1918.
74. Leclerc, H, Périé, JN, Roux, S, Hild, F. 2011. Voxel-scale digital volume correlation. *Experimental Mechanics* 51: 479–490.
75. Leung, VY, Chan, WC, Hung, SC, et al. 2009. Matrix remodeling during intervertebral disc growth and degeneration detected by multichromatic fast staining. *The Journal of Histochemistry and Cytochemistry* 57: 249–256.
76. Liebschner, MA, Kopperdahl, DL, Rosenberg, WS, Keaveny, TM. 2003. Finite element modeling of the human thoracolumbar spine. *Spine* 28: 559–565.
77. Lindsay, R, Silverman, SL, Cooper, C, et al. 2001. Risk of new vertebral fracture in the year following a fracture. *the Journal of the American Medical Association* 285: 320–323.
78. Liu, L, Morgan, EF. 2007. Accuracy and precision of digital volume correlation in quantifying displacements and strains in trabecular bone. *Journal of Biomechanics* 40: 3516–3520.

79. Lyons, G, Eisenstein, SM, Sweet, MB. 1981. Biochemical changes in intervertebral disc degeneration. *Biochimica et Biophysica Acta* 673: 443–453.
80. Mathis, JM, Deramond, H, Belkoff, SM, 2006. Spine anatomy. In, *Percutaneous vertebroplasty and kyphoplasty*. Springer, New York, pp. 8–32.
81. Matsumoto, T, Ohnishi, I, Bessho, M, et al. 2009. Prediction of vertebral strength under loading conditions occurring in activities of daily living using a computed tomography-based nonlinear finite element method. *Spine* 34: 1464–1469.
82. McCubbrey, DA, Cody, DD, Peterson, EL, et al. 1995. Static and fatigue failure properties of thoracic and lumbar vertebral bodies and their relation to regional density. *Journal of Biomechanics* 28: 891–899.
83. McMillan, DW, Garbutt, G, Adams, MA. 1996. Effect of sustained loading on the water content of intervertebral discs: Implications for disc metabolism. *Annals of the Rheumatic Diseases* 55: 880–887.
84. McNally, DS, Adams, MA. 1992. Internal intervertebral disc mechanics as revealed by stress profilometry. *Spine* 17: 66–73.
85. Melton, LJ, 3rd, Kan, SH, Frye, MA, et al. 1989. Epidemiology of vertebral fractures in women. *American Journal of Epidemiology* 129: 1000–1011.
86. Melton, LJ, 3rd, Lane, AW, Cooper, C, et al. 1993. Prevalence and incidence of vertebral deformities. *Osteoporosis International* 3: 113–119.
87. Miller, JA, Schmatz, C, Schultz, AB. 1988. Lumbar disc degeneration: Correlation with age, sex, and spine level in 600 autopsy specimens. *Spine* 13: 173–178.

88. Mirzaei, M, Zeinali, A, Razmjoo, A, Nazemi, M. 2009. On prediction of the strength levels and failure patterns of human vertebrae using quantitative computed tomography (qct)-based finite element method. *Journal of Biomechanics* 42: 1584–1591.
89. Moon, SM, Yoder, JH, Wright, AC, et al. 2013. Evaluation of intervertebral disc cartilaginous endplate structure using magnetic resonance imaging. *European Spine Journal* 22: 1820–1828.
90. Mosekilde, L, Mosekilde, L, Danielsen, CC. 1987. Biomechanical competence of vertebral trabecular bone in relation to ash density and age in normal individuals. *Bone* 8: 79–85.
91. Nazarian, A, Muller, R. 2004. Time-lapsed microstructural imaging of bone failure behavior. *Journal of Biomechanics* 37: 55–65.
92. Nazarian, A, Stauber, M, Zurakowski, D, et al. 2006. The interaction of microstructure and volume fraction in predicting failure in cancellous bone. *Bone* 39: 1196–1202.
93. O'Connell, GD, Johannessen, W, Vresilovic, EJ, Elliott, DM. 2007. Human internal disc strains in axial compression measured noninvasively using magnetic resonance imaging. *Spine* 32: 2860–2868.
94. O'Connell, GD, Vresilovic, EJ, Elliott, DM. 2011. Human intervertebral disc internal strain in compression: The effect of disc region, loading position, and degeneration. *Journal of Orthopaedic Research* 29: 547–555.

95. O'Neill, TW, Felsenberg, D, Varlow, J, et al. 1996. The prevalence of vertebral deformity in european men and women: The european vertebral osteoporosis study. *Journal of Bone and Mineral Research* 11: 1010–1018.
96. Ortiz, AO, Bordia, R. 2011. Injury to the vertebral endplate-disk complex associated with osteoporotic vertebral compression fractures. *American Journal of Neuroradiology* 32: 115–120.
97. Pahr, DH, Schwiedrzik, J, Dall'Ara, E, Zysset, PK. 2014. Clinical versus pre-clinical fe models for vertebral body strength predictions. *Journal of the Mechanical Behavior of Biomedical Materials* 33: 76–83.
98. Pearce, RH, Thompson, JP, Bebault, GM, Flak, B. 1991. Magnetic resonance imaging reflects the chemical changes of aging degeneration in the human intervertebral disk. *The Journal of Rheumatology* 27: 42–43.
99. Perey, O. 1957. Fracture of the vertebral end-plate in the lumbar spine; an experimental biochemical investigation. *Acta Orthopaedica Scandinavica* 25: 1–101.
100. Pfirrmann, CW, Metzdorf, A, Zanetti, M, et al. 2001. Magnetic resonance classification of lumbar intervertebral disc degeneration. *Spine* 26: 1873–1878.
101. Pollintine, P, Dolan, P, Tobias, JH, Adams, MA. 2004. Intervertebral disc degeneration can lead to "stress-shielding" of the anterior vertebral body: A cause of osteoporotic vertebral fracture? *Spine* 29: 774–782.
102. Pollintine, P, Przybyla, AS, Dolan, P, Adams, MA. 2004. Neural arch load-bearing in old and degenerated spines. *Journal of Biomechanics* 37: 197–204.

103. Race, A, Broom, ND, Robertson, P. 2000. Effect of loading rate and hydration on the mechanical properties of the disc. *Spine* 25: 662–669.
104. Richards, MS, 2007. Quantitative three dimensional elasticity imaging. Unpublished doctoral dissertation, Boston University.
105. Riggs, BL, Melton, LJ, 3rd. 1986. Involutional osteoporosis. *The New England Journal of Medicine* 314: 1676–1686.
106. Roberts, S, Menage, J, Eisenstein, SM. 1993. The cartilage end-plate and intervertebral disc in scoliosis: Calcification and other sequelae. *Journal of Orthopaedic Research* 11: 747–757.
107. Roberts, S, Menage, J, Urban, JP. 1989. Biochemical and structural properties of the cartilage end-plate and its relation to the intervertebral disc. *Spine* 14: 166–174.
108. Rodriguez, AG, Rodriguez-Soto, AE, Burghardt, AJ, et al. 2012. Morphology of the human vertebral endplate. *Journal of Orthopaedic Research* 30: 280–287.
109. Rolander, SD, Blair, WE. 1975. Deformation and fracture of the lumbar vertebral end plate. *Orthopedic Clinics of North America* 6: 75–81.
110. Ross, PD, Davis, JW, Epstein, RS, Wasnich, RD. 1991. Pre-existing fractures and bone mass predict vertebral fracture incidence in women. *Annals of Internal Medicine* 114: 919–923.
111. Roughley, PJ. 2004. Biology of intervertebral disc aging and degeneration: Involvement of the extracellular matrix. *Spine* 29: 2691–2699.

112. Roughley, PJ, Alini, M, Antoniou, J. 2002. The role of proteoglycans in aging, degeneration and repair of the intervertebral disc. *Biochemical Society Transactions* 30: 869–874.
113. Setton, LA, Zhu, W, Weidenbaum, M, et al. 1993. Compressive properties of the cartilaginous end-plate of the baboon lumbar spine. *Journal of Orthopaedic Research* 11: 228–239.
114. Silva, MJ, Keaveny, TM, Hayes, WC. 1998. Computed tomography-based finite element analysis predicts failure loads and fracture patterns for vertebral sections. *Journal of Orthopaedic Research* 16: 300–308.
115. Simpson, EK, Parkinson, IH, Manthey, B, Fazzalari, NL. 2001. Intervertebral disc disorganization is related to trabecular bone architecture in the lumbar spine. *Journal of Bone and Mineral Research* 16: 681–687.
116. Stokes, I, Greenapple, DM. 1985. Measurement of surface deformation of soft tissue. *Journal of Biomechanics* 18: 1–7.
117. Stokes, IA. 1987. Surface strain on human intervertebral discs. *Journal of Orthopaedic Research* 5: 348–355.
118. Tawara, D, Sakamoto, J, Murakami, H, et al. 2010. Mechanical evaluation by patient-specific finite element analyses demonstrates therapeutic effects for osteoporotic vertebrae. *Journal of the Mechanical Behavior of Biomedical Materials* 3: 31–40.

119. Thompson, JP, Pearce, RH, Schechter, MT, et al. 1990. Preliminary evaluation of a scheme for grading the gross morphology of the human intervertebral disc. *Spine* 15: 411–415.
120. Thomsen, JS, Ebbesen, EN, Mosekilde, LI. 2002. Age-related differences between thinning of horizontal and vertical trabeculae in human lumbar bone as assessed by a new computerized method. *Bone* 31: 136–142.
121. Tosun, O, Fidan, F, Erdil, F, et al. 2012. Assessment of lumbar vertebrae morphology by magnetic resonance imaging in osteoporosis. *Skeletal Radiology* 41: 1583–1590.
122. Trout, AT, Kallmes, DF, Layton, KF, et al. 2006. Vertebral endplate fractures: An indicator of the abnormal forces generated in the spine after vertebroplasty. *Journal of Bone and Mineral Research* 21: 1797–1802.
123. Ulrich, D, van Rietbergen, B, Laib, A, Ruegsegger, P. 1999. The ability of three-dimensional structural indices to reflect mechanical aspects of trabecular bone. *Bone* 25: 55–60.
124. Unnikrishnan, GU, Barest, GD, Berry, DB, et al. 2013. Effect of specimen-specific anisotropic material models the qct-based finite element analysis of vertebra. *Journal of Biomechanical Engineering* 135: 101007.
125. Unnikrishnan, GU, Morgan, EF. 2011. A new material mapping procedure for quantitative computed tomography-based, continuum finite element analyses of the vertebra. *Journal of Biomechanical Engineering* 133: 071001.

126. Urban, JP, McMullin, JF. 1988. Swelling pressure of the lumbar intervertebral discs: Influence of age, spinal level, composition, and degeneration. *Spine* 13: 179–187.
127. Urban, JP, Roberts, S. 2003. Degeneration of the intervertebral disc. *Arthritis Research & Therapy* 5: 120–130.
128. Vernon-Roberts, B, Pirie, CJ. 1977. Degenerative changes in the intervertebral discs of the lumbar spine and their sequelae. *Rheumatology and Rehabilitation* 16: 13–21.
129. Wade, KR, Robertson, PA, Broom, ND. 2011. A fresh look at the nucleus-endplate region: New evidence for significant structural integration. *European Spine Journal* 20: 1225–1232.
130. Wade, KR, Robertson, PA, Broom, ND. 2012. On the extent and nature of nucleus-annulus integration. *Spine* 37: 1826–1833.
131. Wang, X, Sanyal, A, Cawthon, PM, et al. 2012. Prediction of new clinical vertebral fractures in elderly men using finite element analysis of ct scans. *Journal of Bone and Mineral Research* 27: 808–816.
132. Wang, Y, Owoc, JS, Boyd, SK, et al. 2013. Regional variations in trabecular architecture of the lumbar vertebra: Associations with age, disc degeneration and disc space narrowing. *Bone* 56: 249–254.
133. Wegrzyn, J, Roux, JP, Arlot, ME, et al. 2011. Determinants of the mechanical behavior of human lumbar vertebrae after simulated mild fracture. *Journal of Bone and Mineral Research* 26: 739–746.

134. Whealan, KM, Kwak, SD, Tedrow, JR, et al. 2000. Noninvasive imaging predicts failure load of the spine with simulated osteolytic defects. *The Journal of Bone and Joint Surgery. American Volume* 82: 1240–1251.
135. Windhagen, H, Hipp, JA, Hayes, WC. 2000. Postfracture instability of vertebrae with simulated defects can be predicted from computed tomography data. *Spine* 25: 1775–1781.
136. Yang, H, Nawathe, S, Fields, AJ, Keaveny, TM. 2012. Micromechanics of the human vertebral body for forward flexion. *Journal of Biomechanics* 45: 2142–2148.
137. Yoganandan, N, Maiman, DJ, Pintar, F, et al. 1988. Microtrauma in the lumbar spine: A cause of low back pain. *Neurosurgery* 23: 162–168.
138. Zhao, FD, Pollintine, P, Hole, BD, et al. 2009. Vertebral fractures usually affect the cranial endplate because it is thinner and supported by less-dense trabecular bone. *Bone* 44: 372–379.
139. Zysset, PK, Dall'ara, E, Varga, P, Pahr, DH. 2013. Finite element analysis for prediction of bone strength. *BoneKEy Reports* 2: 386.

CURRICULUM VITAE

Timothy Maxfield Jackman

44 Cummington Mall

Boston, MA 02215

jackmant@bu.edu

EDUCATION

2010 – 2015 Ph.D. in Biomedical Engineering, Boston University

2010 – 2014 M.S. in Biomedical Engineering, Boston University

2007 – 2010 B.S. in Mechanical Engineering, Brigham Young University

POSITIONS

2010 – 2015 Graduate Research Assistant, Department of Biomedical Engineering,
Boston University

2013 Graduate Teaching Fellow, Department of Mechanical Engineering,
Boston University. Course: Engineering Mechanics

2012 Graduate Teaching Fellow, Department of Biomedical Engineering,
Boston University. Course: Respiratory and Cardiovascular Systems

2008 – 2009 Teaching Assistant, Department of Mechanical Engineering, Brigham
Young University. Course: Engineering Dynamics

PUBLICATIONS

Book Chapters

Morgan EF, Jackman TM, McDonald G. Micro-CT imaging of bone tissue. In: Simpson
H, Augut P, editors. *Experimental Research Methods in Orthopedics and Trauma*.
Thieme; In press

Journal Publications

Jackman TM, Hussein AI, Adams AM, Makhnejia KK, Morgan EF. Endplate deflection is a defining feature of vertebral fracture and is associated with properties of the underlying trabecular bone. *Journal of Orthopaedic Research*, 2014 32(7):880–6

Hussein AI, Jackman TM, Morgan S, Barest G, Morgan EF. The intervertebral distribution of bone density: Correspondence to intervertebral disc health and implications for vertebral strength. *Osteoporosis International*, 2013 24(12):3021– 30

Conference Presentations

Jackman TM, DelMonaco AM, Morgan EF. Accuracy of QCT-Based Finite Element Predictions of Vertebral Fracture When Boundary Conditions are Based on Intradiscal Pressure Profiles. Summer Biomechanics, Bioengineering and Biotransport Conference, 2015

Jackman TM, Morgan EF. QCT-Based Finite Element Models Do Not Accurately Predict Vertebral Failure Under Anterior Flexion. 61st Annual Meeting of the Orthopaedic Research Society, 2015.

DelMonaco AM, Jackman TM, Fein PM, Adams AM, Makhnejia KK, Morgan EF. Quantifying the Spatial Distribution of Intradiscal Pressure and its Assessment via Non-Invasive Estimates of Intervertebral Disc Degeneration. 61st Annual Meeting of the Orthopaedic Research Society, 2015.

Fein PM, Adams AM, Hussein AI, Jackman TM, Morgan EF. Improving Measurement of Intra-Vertebral Heterogeneity in Bone Density for Use in Prediction of Spine Fractures. GE Student Research Summit, 2014

Jackman TM, Hussein AI, Morgan EF. Experimental measurement of the progression of vertebral fracture under anterior flexion. 7th World Congress of Biomechanics, 2014. MS Student Paper Competition 233

Morgan EF, Hussein AI, Unnikrishnan GU, Jackman TM. Quantitative visualization of vertebral failure for advancing study of the pathogenesis of spine fractures. 7th World Congress of Biomechanics, 2014. Podium presentation 3202

Jackman TM, Hussein AI, Adams AM, Makhnejia KK, Morgan EF. Endplate deflection is a defining feature of vertebral fracture and is associated with properties of the underlying trabecular bone. *59th Annual Meeting of the Orthopaedic Research Society*, 2013. Podium presentation 0289

Hussein AI, Jackman TM, Morgan EF. Associations between spatial distributions of bone density within the vertebral centrum and both vertebral strength and disc quality. *59th Annual Meeting of the Orthopaedic Research Society*, 2013. Poster session 1500